Numerical Optimization of a Finned Cavity Latent Thermal Energy Storage Enclosure for Solar Power Production

by

Johann Möller

Submitted in partial fulfilment of the requirements for the degree of

Masters of Engineering

In the Department of Mechanical and Aeronautical Engineering in the Faculty of Engineering, Built Environment and Information Technology

UNIVERSITY OF PRETORIA

22 February 2022

Abstract

Author: Johann Möller

Student number: 11057727

Supervisors: Prof J Dirker and Prof JP Meyer

Department: Mechanical and Aeronautical Engineering

Degree: Masters of Engineering (Mechanical Engineering)

The utilization of thermal solar energy has significantly increased in recent times. However, due to the daily temporal nature of solar irradiation, which is affected by, for instance, cloud coverage, efficient thermal energy storage (TES) techniques are needed. Latent heat energy storage using phase change materials (PCMs) is a promising technology for concentrated solar power (CSP), but due to the low thermal conductivity of many PCMs, careful geometric design is required to sustain acceptable energy charging and discharging rates. In this numerical investigation the heat transfer rate in a latent heat thermal energy storage enclosure containing sodium nitrate PCM and horizontal high-conductive aluminium plate fins was considered. An enthalpy-porosity technique was used to model the phase change process in a two-dimensional domain while also considering buoyancy driven flow. The influence of the fin pitch on the heat rate during energy discharge, when the PCM solidifies, was studied. The width of the enclosure and the thickness of the fins relative to the enclosure volume was kept constant. Two thermal boundary condition cases were investigated, being, when the outer wall was 10 K and 5 K colder than the phase change temperature. The results revealed a definite optimum fin pitch exist when the wall temperature is 10 K colder than the phase change temperature.

Acknowledgements

I would like to thank the following people who helped me undertake and complete this research project:

The Clean Energy Research Group and Professor Josua Meyer for providing me with the opportunity and resources to undertake this study.

My supervisor Professor Jaco Dirker for providing me with excellent guidance and support throughout the course of this dissertation and without whose insight and knowledge I would not have been able to make it to the end.

The National Research Foundation (NRF) for providing the funding required to undertake this study.

The South African Centre for High Performance Computing (CHPC) for allowing the use of their facilities throughout the duration of this investigation.

My family for their continuous support which helped keep me motivated; especially Ilana who kept pushing me when I needed it most.

Reinette for being there for me and right beside me, helping me through the important last stretch.

Last but not least, I would like to thank my Heavenly Father for granting me the opportunities, knowledge and perseverance so that I could finish this dissertation.

Table of Contents

1. Introduction 1
   1.1 Background 1
   1.2 Problem statement 5
   1.3 Aim of study 5
   1.4 Overview of document structure 5
2. Literature Review 7
   2.1 Solar thermal power generation 7
   2.2 Thermodynamic cycles 7
   2.3 Thermal energy storage 9
   2.4 Latent heat thermal energy storage through use of phase change materials 12
      2.4.1 Thermophysical material properties 13
      2.4.2 Containment methods 15
      2.4.3 Heat transfer enhancement 16
   2.5 TES applications using PCM 17
   2.6 Heat transfer in PCMs 21
      2.6.1 Heat transfer mechanisms during phase change 22
      2.6.2 The moving boundary problem 22
      2.6.3 Solutions to the moving boundary problem 23
   2.7 Chapter summary 25
3. Thermal Energy Storage Application 26
   3.1 Enclosure 26
   3.2 Materials selection 28
      3.2.1 Thermophysical properties 29
   3.3 Chapter summary 30
4. Numerical Method 31
   4.1 Simulation platform 31
   4.2 Domain 31
   4.3 Boundary and initial conditions 32
   4.4 Governing equations 32
      4.4.1 Navier-Stokes equations 32
      4.4.2 Solidification and melting 33
   4.5 Mesh 36
      4.5.1 Mesh theory 36
      4.5.2 Meshing type 36

4.6 Determining the mesh and time step size 39
4.6.1 Mesh independence 40
4.6.2 Time step independence 45
4.6.3 Final mesh and time step size 48
4.7 Chapter summary 48
5. Numerical Method Validation 50
5.1 Experimental setup (Johnson et al.) 50
5.2 Numerical setup adjustment 52
5.3 Result Comparisons 53
5.4 Chapter summary 58
6. Sample Case Results 59
6.1 Dimensions and boundary conditions 59
6.2 Sample Results 59
6.3 Chapter summary 61
7. Parametric Study 62
7.1 Design variables 62
7.2 Results 63
7.2.1 $\Delta T = 10\ \mathrm{K}$ 64
7.2.2 $\Delta T = 5\ \mathrm{K}$ 69
7.3 Analyses 74
7.3.1 $\Delta T = 10\ \mathrm{K}$ 74
7.3.2 $\Delta T = 5\ \mathrm{K}$ 76
7.4 Chapter summary 79
8. Summary, Conclusions and Recommendations 80
8.1 Summary 80
8.2 Conclusions 81
8.3 Recommendations 81
Bibliography 82

List of Figures

Figure 1 Renewables breakdown 2019 (REN21, 2020).... 1
Figure 2 Different fin configurations. (a) longitudinal fins (b) annular fins (c) circular fins (d) plate fins (e) pin fins and (f) tree shaped fins (Abdulateef et al., 2018).... 4
Figure 3 Latent heat storage system with PCM, fins and HTF layout.... 5
Figure 4 Thermal energy storage techniques.... 10
Figure 5 Maturity status of storage technology(Tamme et al., 2005).... 11
Figure 6 Classification of solid-liquid PCMs (Xu et al., 2015).... 13
Figure 7 Heat transfer enhancement techniques (Agyenim et al., 2010).... 16
Figure 8 Solar water heating system with PCM TES (Mahfuz et al., 2014a).... 19
Figure 9 Schematic of a solar thermal power plant with PCM TES (Mahfuz et al., 2014b)... 20
Figure 10 Different TES device orientations (a) flat plate (b) shell and tube - internal flow (c) shell and tube - parallel flow (d) shell and tube - cross flow and (e) packed bed (Li et al., 2019).... 21
Figure 11 Moving boundary progression with time.... 23
Figure 12 PCM TES application with plate fins.... 26
Figure 13 PCM TES tube layout and characteristic region for (a) inline and (b) staggered arrangements.... 27
Figure 14 Simplified single shell and tube PCM TES with (a) a three-dimensional representation and (b) a two-dimensional cross section in the vertical plane.... 27
Figure 15 TES enclosure with PCM and its dimensions.... 28
Figure 16 Numerical domain with dimensions and boundary conditions.... 31
Figure 17 Basic mesh type used in this study.... 37
Figure 18 Dynamic mesh refinement.... 38
Figure 19 Independence study domain dimensions.... 39
Figure 20 Mesh independence heat transfer wall heat flux vs time.... 41
Figure 21 Mesh independence solid fraction vs time.... 41
Figure 22 Error for ψ of all mesh cases vs time.... 42
Figure 23 GCI independence vs full simulation time.... 44
Figure 24 GCI independence vs t > 50s.... 44
Figure 25 Time step independence heat transfer wall heat flux vs time.... 46
Figure 26 Time step independence solid fraction vs time.... 46
Figure 27 Error for ψ of all time step cases vs time.... 47
Figure 28 (a) Experimental setup of flat plate PCM storage unit and (b) a sketch of the storage tank with a two-dimensional plat cut for the simulation (Johnson et al., 2014).... 50
Figure 29 Numerical domain used by Pointner et al. (2016).... 52
Figure 30 Numerical domain used for this validation study.... 53
Figure 31 Validation results vs experimental for thermocouples a) TC12 b) TC40 c) TC17 and d) TC18.... 54
Figure 32 TC12 validation result comparison and associated errors.... 55
Figure 33 TC40 validation result comparison and associated errors.... 55
Figure 34 TC17 validation results error comparison and associated errors.... 56
Figure 35 TC18 validation results error comparison and associated errors.... 56
Figure 36 Numerical domain for $L = 50\ mm$, $P = 8\ mm$, $tf = 0.8\ mm$, $Tw = 296\ °C$ $Ti, Domain = 306{,}85\ °C$.... 59
Figure 37 Heat flux vs time.... 60
Figure 38 Solid fraction vs time.... 60

Figure 39 Phase boundary progression at a) 100 s b) 1000 s and c) 2000 s. 61
Figure 40 Numerical domain. 62
Figure 41 Heat flux results $\Delta T = 10\ K$. 64
Figure 42 Solid fraction results for $\Delta T = 10\ K$ 64
Figure 43 Difference between minimum and maximum ψ values for $\Delta T = 10\ K$. 65
Figure 44 Solidification time progress for $\Delta T = 10\ K$. 66
Figure 45 Phase boundary for $\Delta T = 10\ K$ at a) 100 s b) 500 s c) 1000 s d) 1500 s e) 2000 s and f) 2400 s for different pitch distances. 68
Figure 46 Heat flux results $\Delta T = 5\ K$. 69
Figure 47 Solid fraction results $\Delta T = 5\ K$. 69
Figure 48 Difference between minimum and maximum ψ values for $\Delta T = 5\ K$. 70
Figure 49 Solidification time progress for $\Delta T = 5\ K$. 71
Figure 50 Phase boundary for $\Delta T = 5\ K$ at a) 100 s b) 1000 s c) 2000 s d) 3000 s e) 4000 s and f) 4700 s for different pitch distances. 72
Figure 51 Comparison at $\psi \approx 0.85$ for $P = 4\ mm$ of (a) $\Delta T = 10\ K$ and (b) $\Delta T = 5\ K$ showing the (i) phase boundary and (ii) velocity fields. 73
Figure 52 Comparison at $\psi \approx 0.85$ for $P = 2\ mm$ of (a) $\Delta T = 10\ K$ and (b) $\Delta T = 5\ K$ showing the (i) phase boundary and (ii) velocity fields. 74
Figure 53 Solid fractions in terms of pitch distance at a) 100 s b) 500 s c) 1000 s d) 1500 s e) 2000 s and f) 2400 s ($\Delta T = 10\ K$). 75
Figure 54 Position of maximum solid-fraction pitch $\Delta T = 10\ K$. 76
Figure 55 Solid fractions in terms of pitch distance at a) 100 s b) 1000 s c) 2000 s d) 3000 s e) 4000 s and f) 4700 s ($\Delta T = 5\ K$). 77
Figure 56 Position of maximum solid fraction pitch $\Delta T = 5\ K$. 78
Figure 57 Position of shortest time to ψ for $\Delta T = 10\ K$ and $\Delta T = 5\ K$. 78

List of Tables

Table 1 Comparison of organic and inorganic materials for heat storage. 14
Table 2 Salt hydrates with potential use as PCM. 14
Table 3 Metallics with potential use as PCM (Khare et al., 2012). 15
Table 4 Inorganic eutectics with potential use as PCM. 15
Table 5 Thermophysical properties of PCM and fin material. 30
Table 6 Mesh independence cases. 40
Table 7 Mesh independence errors. 42
Table 8 GCI independence average and standard deviation across time. 45
Table 9 Time step independence cases. 45
Table 10 Time step independence errors. 47
Table 11 Thermophysical properties of validation model PCM and fin material used by Johnson et al. 51
Table 12 Validation thermocouple accuracies. 57
Table 13 Numerical study parameter set. 63
Table 14 Solidification time progress for $\Delta T = 10\ K$. 66
Table 15 Solidification time progress for $\Delta T = 5\ K$. 70

Nomenclature

English letters and symbols

Symbol	Description	Units
A	Porosity function	
A_{mush}	Mushy zone parameter used by ANSYS Fluent's solidification and melting solver	-
a^*	Aspect ratio of PCM container	-
c	Empirical constant	-
C_{p}	Specific heat	J/kg.K
$C_{\mathrm{p,ave}}$	Average specific heat between the initial and final temperature	J/kg.K
$C_{\mathrm{p,f}}$	Specific heat for final phase	J/kg.K
$C_{\mathrm{p,i}}$	Specific heat for the initial phase	J/kg.K
$C_{\mathrm{p,k}}$	Specific heat for PCM in phase K	J/kg.K
$C_{\mathrm{p,l}}$	Specific heat for liquid	J/kg.K
$C_{\mathrm{p,s}}$	Specific heat for solid	J/kg.K
D	Averaged deviation between numerical and experimental results	-
dT	Change in temperature	K
dV	Change in volume	m^3
dx	Mesh cell horizontal size	mm
dy_{f}	Mesh cell size for fin region	mm
dy_{PCM}	Mesh cell size for PCM region of container	mm
E	Energy	J
f_1	Solution value for GCI case 1	
f_2	Solution value for GCI case 2	
f_3	Solution value for GCI case 2	
F_{s}	Safety factor used in GCI study	-
$\vec{F}$	External body forces	N
g	Gravitational acceleration	m/s^2
h	Sensible volumetric enthalpy	J/m^3
h_{c}	Convective heat transfer coefficient	$W/m^2.K$
h_{f}	Sensible volumetric enthalpy for container material	J/m^3
H	Total volumetric enthalpy	J/m^3
H_{f}	Latent heat of fusion	J/kg
Δh_{r}	Endothermic heat of reaction	J/kg
ΔH	Latent heat	J/kg
k_{eff}	Effective thermal conductivity	W/m.K
k_{k}	Thermal conductivity of PCM in phase k	W/m.K

k_{l}	Thermal conductivity of liquid PCM	W/m.K
L	Melt layer thickness/width of PCM enclosure	m
m	Mass	kg
n	Empirical constant	-
p	Pressure/observed order of truncation error decay	Pa; -
P	Pitch of fins in PCM container	mm
q	Heat flux	W/m^2
Q	Heat energy	J
r	Ratio between mesh sizes	-
Ra	Rayleigh number	-
R^2	Coefficient of determination - the proportion of the variance in the dependent variable that is predictable from the independent variable	-
S	Latent heat source term	
S_{b}	Boussinesq source term	
S_{h}	Source term for volumetric heat sources	
S_{m}	Source term for mass	
S_x	x momentum source term	
S_y	y momentum source term	
t	Time	s
t_0	initial time	s
t_{s}	Time step	s
t_{f}	Thickness of PCM container fin	mm
T	Temperature	°C
T_{c}	Heat rejection temperature	°C
T_{expr}	Temperature obtained from experimental results	°C
T_{f}	Final temperature	°C
T_{h}	Heat supply temperature	°C
T_{i}	Initial temperature	°C
$T_{\mathrm{i,Domain}}$	Initial temperature of the domain	°C
$T_{\mathrm{i,Fin}}$	Initial temperature of the fin	°C
$T_{\mathrm{i,PCM}}$	Initial temperature of the PCM	°C
T_{l}	Liquidus temperature	°C
T_{m}	Melting temperature of PCM	°C
T_{ref}	Reference temperature	°C
T_{s}	Solidus temperature	°C
T_{sim}	Temperature obtained from the validation (simulation) model	°C
T_{w}	Wall temperature	°C
ΔT	Difference between wall temperature and PCM melting temperature	K

v	Velocity	m/s
v_x	Velocity in x direction	m/s
v_y	Velocity in y direction	m/s
$\vec{v}$	Velocity vector	m/s
$\overrightarrow{v_{\mathrm{l}}}$	Actual liquid velocity vector	m/s
V	Volume	m^3
x	Horizontal position/space coordinate	m
X	Surface position of moving boundary (phase change front)	m
y	Vertical position/space coordinate	m

Greek symbols

α	Thermal diffusivity	m^2/s
α_{f}	Thermal diffusivity of container material	m^2/s
β	Volumetric/thermal expansion coefficient	K^{-1}
δ	Change in property	
Δ	Change in property	
ε	Half temperature range of the mushy zone	K
$\varepsilon_{t_{\mathrm{s}},\psi}$	Error of solid fraction between consecutive time step sizes	-
$\varepsilon_{\mathrm{mesh},\psi}$	Error of solid fraction between consecutive mesh sizes	-
η_{c}	Carnot efficiency	-
η_{th}	Thermal efficiency of TES system	-
ξ	Percentage of numerical results that fall within experimental uncertainty range	%
λ	Porosity	-
μ	Dynamic viscosity	kg/m.s
ρ	Density	kg/m^3
ρ_{k}	Density of PCM in phase k	kg/m^3
ρ_{l}	Density of liquid PCM	kg/m^3
σ	Standard deviation	-
$\bar{\bar{\tau}}$	Stress tensor	N
ϕ	Melt fraction of PCM	-
ϕ_{r}	Fraction of material that has reacted chemically	-
ψ	Solid fraction	-
$\Delta\psi_{t,\mathrm{ij}}$	Difference in solid fraction between two cases (i and j) at a certain time (t)	-
$\Delta t_{\psi,\mathrm{ij}}$	Difference in time taken to reach a certain solid fraction (ψ) between two cases (i and j) at	s

Acronyms and miscellaneous

AMR	Adaptive mesh refinement
ANSYS	Commercial software
CFD	Computational fluid dynamics
CSP	Concentrated solar power
DSG	Direct steam generation
FDM	Finite difference method
FEM	Finite element method
GCI	Grid convergence indicator
HTF	Heat transfer fluid
LHS	Latent heat storage
PCM	Phase change material
PV	Photo voltaic
TC	Thermocouple
TES	Thermal energy storage

1. Introduction

1.1 Background

The greenhouse gas concentration in the atmosphere caused by fossil fuel combustion is rising by 2-3 ppm per year and it is predicted that this will cause a rise in mean global surface temperatures of between 1.8 °C and 6.4 °C by the end of the 21st century. This correlates to a predicted rise in mean global sea levels of up to 0.59 m due to thermal expansion alone (Redpath et al., 2010). Many countries are thus starting the move to renewable energy sources over traditional fossil fuel power to combat this global warming. In 2018 renewable energy sources produced an estimated 11% of the total energy consumed worldwide, a number that rose by almost 13% from the 9.6% contribution in 2013. The sector that saw the highest share of renewables in 2018 at 26.4%, was the power generation sector (REN21, 2020).

Renewable energy power generation can take place in a number of different ways. In 2019 the most-prevalent approaches were: hydropower, wind power, solar power (photovoltaics and concentrated solar power), bio power, geothermal, and ocean power. The contribution of each of these technologies are shown in Figure 1.

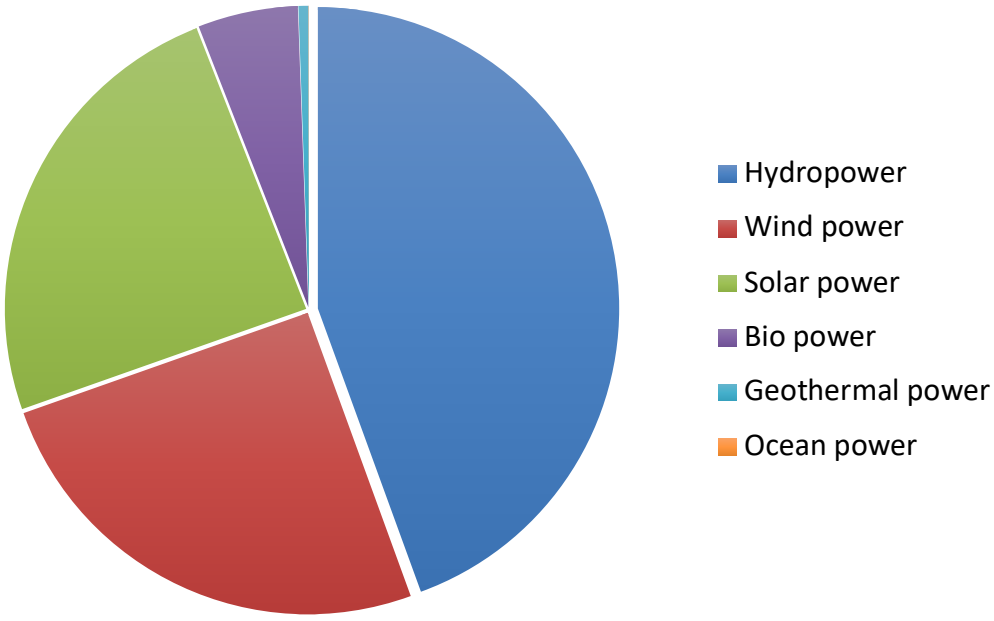

Figure 1 Renewables breakdown 2019 (REN21, 2020).

Hydropower is still responsible for the majority of the renewable energy generation worldwide and even though it had an estimated increase of 15.6 GW to its capacity in 2019, this was its smallest increase in the last seven years. Wind power had a much larger annual increase of 60 GW from 2018 to 2019 (its second highest annual increase) and its cost fell world-wide due to technological innovations, a lower perceived risk and fierce competition in the industry. The largest annual increase in capacity, however, came from solar power – 115.6 GW of additional generating capacity from 2018 to 2019. The majority of the existing solar power is from solar photovoltaics (PV), but price reductions driven by competition and

ongoing research and development in the concentrated solar power (CSP) sector has meant it has emerged as a viable competitor to fossil fuel thermal power plants.

Solar power can be harnessed via a range of different CSP systems, including flat-plate collectors, parabolic trough collectors and central tower receivers (also called solar power towers). These systems operate at different temperature ranges: low temperatures (colder than 100 °C), medium temperatures (colder than 400 °C) and high temperatures (warmer than 400°C) (P Sukhatme, 1997). Large scale solar power generation largely employ the use of technologies in the medium to high temperature ranges (parabolic trough collectors and solar power towers).

The rise in the deployment of CSP has presented new opportunities and challenges. Because direct solar energy is not necessarily adequately available during periods of peak electricity demand, effective energy storage solutions are needed. During times of abundant solar radiation, excess energy is to be collected and stored until there is a need to supplement the solar resource (periods with significant cloud coverage or at dusk), or to replace the solar resource (at night).

Energy storage is required for different time spans based on the need. In the case of normal operation for solar, energy storage with a capacity less than 8 hours is necessary which can be recharged during the next day. In worse cases, during times of long-lasting inclement weather or a storm, energy capacity of several days or weeks might be needed. These different energy storage durations can be classified as short, medium and long term. There is not an official definition for these, with literature varying from a few seconds to minutes for short term and minutes or hours for long term (Faias et al., 2008); less than 2 hours for short term, 2-8 hours for medium term (long term) and a day to weeks for long term (very long term) (Schoenung, 2001); and less than 4 hours for short term, 4-200 hours for medium and longer than 200 hours for long term (Garvey, 2020).

The energy produced from solar can be stored in different ways depending on the type of power generation. Energy harnessed using PV systems are usually stored using lithium-ion (or similar) batteries, while thermal solar energy harnessed with CSP systems can be stored by making use of chemical storage (thermal chemical pipe lines), sensible heat (packed-bed storage) or latent heat (phase change material, or PCM, systems). Thermal energy storage (TES) offers a low-cost advantage compared to, for instance electrical energy storage. Because a thermodynamic cycle is needed to convert the stored thermal energy into electricity, it is very suited for use with CSP plants.

Sensible heat storage systems (using single phase solids or liquids) are the most widely used and simplest TES solution. It does, however, have relatively low energy storage densities and suffers from temperature glide during charging and discharging, which can be problematic for the operation of some thermodynamic power cycles. On the other hand, latent heat (thermal energy) storage systems (LHS) have higher energy densities and can discharge energy at relatively constant temperatures. LHS have significant potential to offer high capacity on a commercial scale in the near future for use with thermodynamic cycles.

LHS systems store the latent energy in phase change materials (PCMs). PCMs change their physical characteristics when absorbing or releasing heat – usually by changing between either solid and liquid or liquid and gas phases. The heat absorbed (or released) during this

change is known as the latent heat (or enthalpy) of fusion for solid-liquid and the latent heat of evaporation for liquid-gas PCMs. Solid-liquid PCMs have much smaller volumetric changes than liquid/gas, which make them more feasible for use in TES.

A solid-liquid LHS system is charged during the melting phase of the PCM and discharged during the solidification of the PCM. The LHS system in a CSP plant would be charged by heating a HTF with thermal solar energy and having it flow past the PCM, causing it to melt. When the solar resource needs to be supplemented or replaced, the LHS system would be discharged by directing HTF in close proximity of the energy storage system, extracting heat energy and causing the PCM to solidify.

These solid-liquid PCMs are split into three main categories: organic, inorganic and eutectic. Organic PCMs have lower melting temperatures (15 – 45 °C) and lower latent heat capacities (around 120 kJ/kg to 250 kJ/kg) (Souayfane et al., 2016), whilst inorganic PCMs tend to have much higher melting temperatures (up to 900 °C) and latent heat capacities (up to 400+ kJ/kg). Eutectic PCMs are homogeneous mixtures of two or more materials (organic-inorganic, organic-organic or inorganic-inorganic) that does not result in a new chemical compound and melts or solidifies at a single temperature that is less than or equal to the lowest melting temperature of any of its components. The melting temperature and latent heat capacity of eutectic PCMs thus vary from mixture to mixture.

Inorganic PCMs consist of salts, salt hydrates and metallics, each with its own advantages and disadvantages. Salts and salt hydrates are freely available, affordable and chemically stable but they also have very low thermal conductivities (0.5 – 5 W/m.K) which greatly inhibits conduction heat transfer. Metallic PCMs have higher thermal conductivities but have other disadvantages, including availability and affordability, which will be discussed in detail in a later chapter. The thermal conductivities of organic PCMs are even lower than those of inorganic.

The low thermal conductivities of most PCMs have a significantly negative impact on the charging and discharging rates when used for TES and additional design is required to make them a viable option. Literature has revealed that the thermal resistance posed by the PCM is greater during solidification than during charging (Robak et al., 2011). Numerous options have been investigated in literature to increase the overall heat transfer rate of the system. These include extended fin surfaces, dispersion of highly conductive particles/materials in the PCM, expanded metal foams impregnated with PCMs, and the use of heat pipes.

The use of fins to increase the overall heat transfer rate in LHS systems is an attractive solution due to its simplicity and efficiency during both charging and discharging cycles. It does, however, require careful design and optimisation, especially in terms of the fin's geometry, to produce optimal results. Fins have numerous parameters that could influence their effect on the performance of the LHS system, including the choice between full fins (which extend the full length of the enclosure which they are in in the direction of the fin length - also known as plate fins) or partial fins, which material to use for the fins, the width of the PCM enclosure, the thickness of the fins in relation to the PCM and the pitch of the fins. A few fin configurations are shown in Figure 2.

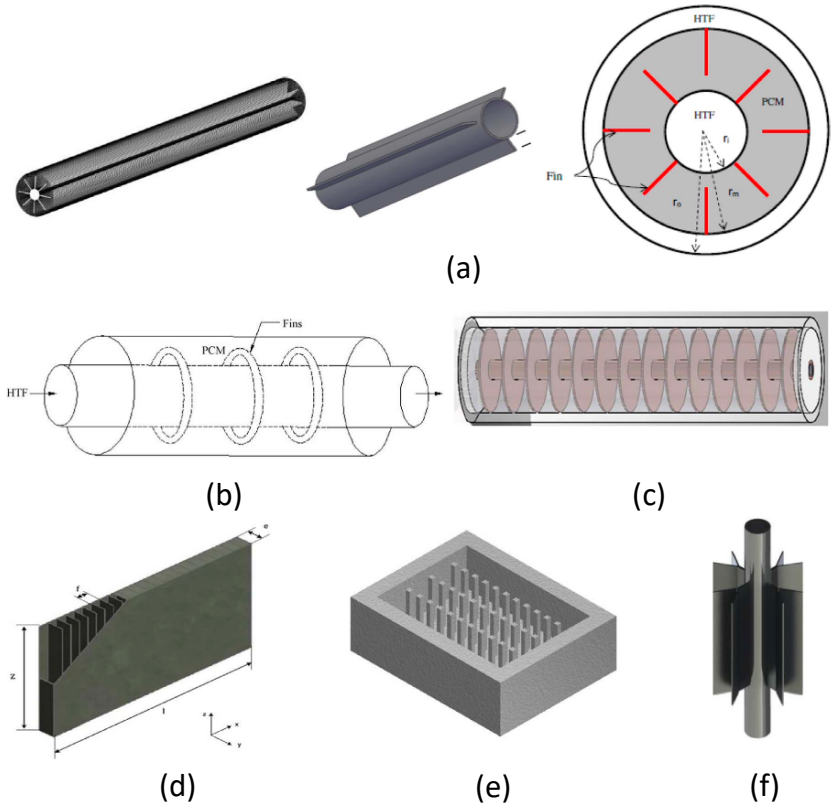

Figure 2 Different fin configurations. (a) longitudinal fins (b) annular fins (c) circular fins (d) plate fins (e) pin fins and (f) tree shaped fins (Abdulateef et al., 2018).

A number of studies have already been done on the viability of fins as heat transfer enhancement for latent heat thermal storage systems. Velraj et al. (1999) conducted an experimental study to investigate longitudinal fins inside a paraffin filled vertical cylindrical tube and found that the addition of fins decreased the time required for completed solidification by approximately 75% while only occupying 7% of the tube volume. Studies by Sharifi et al. (2011) and Kamkari and Shokouhmand (2014) investigated the effect of internal partial fins on the melting rate of a PCM in a rectangular enclosure and found that even though increasing the fin length and the number of fins in an enclosure hinders natural convection currents, it still increased the overall heat transfer rate of the system.

Literature reveals the importance of heat transfer enhancements in overcoming the inherent low thermal conductivity of most PCMs that hinder LHS from becoming a viable alternative for CSP plants. Highly conductive plate fins – which maximises the fin length – have been identified as a good option in enhancing the heat transfer during both melting and solidification but not enough is known about the effect of the fin pitch on especially the discharge of energy from LHS systems. Obtaining a fin pitch at which the heat transfer rate is at a maximum could not only improve the efficiency of LHS systems, but possibly also decrease manufacturing complexity and costs.

Not a lot of studies are available on the influence of buoyancy driven natural convection on the heat transfer rate in LHS using horizontal plate fins as heat transfer enhancement. The effect of the pitch spacing of the fins on the relative strength of buoyancy has not been reported on sufficiently yet.

1.2 Problem statement

It is evident that the fin pitch plays a big role in heat transfer advancement, but there is not enough literature attempting to find an optimum fin pitch for LHS systems, especially during the discharging (or solidification) of the PCM. The fin pitch of horizontal fins is of particular interest since larger fin pitch spacings could in theory promote buoyancy driven natural convection heat transfer.

1.3 Aim of study

This study focuses on the release of energy from a short term LHS system, applied in CSP systems, using plate fins as heat transfer enhancement. Under consideration is a PCM that is housed in a finned rectangular enclosure coupled to a HTF flow path as is shown schematically as a two-dimensional representation in Figure 3.

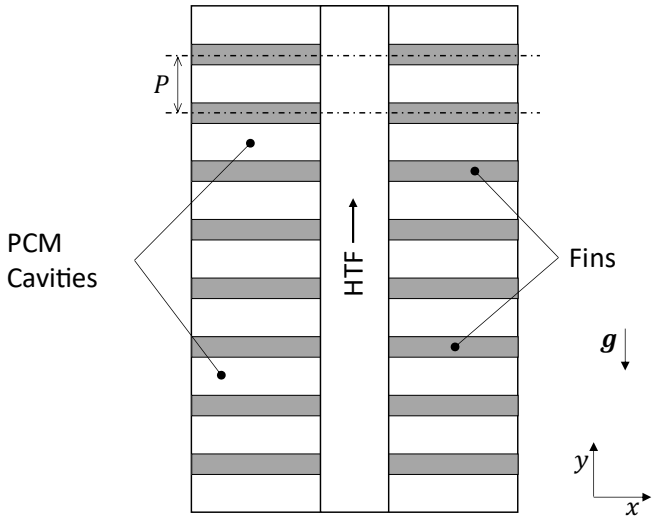

Figure 3 Latent heat storage system with PCM, fins and HTF layout.

The study aims to achieve the following:

- Develop a transient-based numeric model with which to simulate the thermal and phase change response during an energy discharging (solidification) process.
- Build confidence in the numerical model by validating it against experimental results from independent literature.
- Determine whether an optimum fin pitch (P) exists which maximises the discharge rate (PCM solidification) of an LHS system.
- Discuss the real-world implications of the outcome of the optimisation study and how it could improve the viability of using LHS systems for solar energy storage.

1.4 Overview of document structure

In Chapter 2 a brief literature review is presented on the theory behind solar thermal power generation, thermal energy storage, phase change materials, numerical methods on solving the phase change problem and previous studies done on solving solidification and melting.

In Chapter 3 the specific latent heat thermal energy storage application and geometric layout is presented, and simplified to a two-dimensional representative domain. The materials used for the fin and PCM are defined along with their thermophysical properties.

In Chapter 4 the numerical method is defined in terms of the simulation platform on which the model is solved, the domain based on the geometry of the enclosure, the boundary conditions applied to the domain, the equations governing the solution of the solidification and melting process in the simulation platform and the numerical mesh applied to the domain. After this the results from the mesh and time step independence studies conducted are presented and the mesh and time step sizes at which the model reached a sufficiently independent solution are determined.

In Chapter 5 a validation study is performed against independently produced experimental data from literature to determine whether the numerical method described in Chapter 4 is able to correctly simulate the thermal-fluid interactions in the liquid and solid phases.

In Chapter 6 a sample case is defined with values for the domain parameters described in Chapter 4 and 5. The solidification results of this case are presented to highlight any points of interest which will be of value for the parametric study in the following chapter.

In Chapter 7 design parameters for the parametric study are defined, the results from the simulations are presented and the parametric study is performed to find the fin pitch which maximises the discharge heat transfer rate. The results are then analysed and the implications thereof discussed.

In Chapter 8 the conclusions that were reached during this study are stated and any recommendations for studies following from this one, are presented.

2. Literature Review

This chapter provides a brief literature review into the fields associated with LHS systems, including solar thermal power generation, the thermodynamic cycles used in solar thermal power generation, thermal energy storage, phase change materials, the different heat transfer advancement techniques applied in PCMs, the numerical methods used to solve the phase change problem and previous studies done on solving solidification and melting.

2.1 Solar thermal power generation

Solar energy can be harnessed for power generation in various ways; the most dominant being PV systems and CSP plants. PV systems directly convert solar radiation into electric current using the photovoltaic effect, while CSP plants use a combination of lenses or mirrors to concentrate thermal solar radiation which can be thermodynamically converted to mechanical work and electricity (Lovegrove and Stein, 2012). Whilst PV and CSP systems can be combined (by concentrating solar energy onto photovoltaic cells) it is not the focus of this study – focus will, instead, be placed on thermal CSP systems which are of more interest in this investigation.

CSP systems are reliant on solar collectors to receive thermal energy. This can be done by employing a range of different collector designs, configurations, and methods:

- Flat-plate collectors.
- Solar ponds.
- Parabolic trough reflectors/collectors.
- Central tower receiver with a field of heliostat reflectors.
- Linear Fresnel reflectors/collectors.
- Paraboloidal dish reflectors/collectors.

The thermodynamic cycles used for solar thermal power generation can be broadly classified into three ranges, based on the temperature of the inbound heat transfer process, which typically makes use of a different collector schemes (P Sukhatme, 1997):

- Low temperature, below 100 °C, via flat-plate collectors and solar ponds;
- Medium temperature, below 400 ° C, via parabolic trough and linear Fresnel reflectors/collectors;
- High temperature, above 400 °C, via central tower receivers and paraboloidal dish collectors.

For large scale solar power generation, the main technologies currently in operation are parabolic trough collectors and central tower receivers (Islam et al., 2018).

2.2 Thermodynamic cycles

Thermal-to-electric conversion is usually done via a thermodynamic power cycle coupled to an electric generator. In such systems, the cycle efficiency is of paramount importance and generally increases as the supply heat temperature increases and/or when the heat rejection temperature decreases (Karni, 2012).

For an ideal reversible cycle, the theoretical maximum efficiency is that of the Carnot efficiency:

$$\eta_{\mathrm{c}} = 1 - \frac{T_{\mathrm{c}}}{T_{\mathrm{h}}} \tag{1}$$

where T_{c} is the heat rejection temperature and T_{h} is the heat supply temperature, both measured in Kelvin.

Thermodynamic cycles that operate at higher supply temperatures are thus of specific interest because of their increased plausible thermodynamic efficiencies. Several thermodynamic cycles exist which are suitable to high supply temperatures. The most commonly used high-temperature cycles are the Brayton cycle, Rankine cycle, Kalina cycle or a combination of these cycles into a single system (Yu et al., 2015).

The simplicity of single cycles, like the Brayton and Rankine cycles, and their representation of the simplest thermal power plant configurations mean they can be used as baselines in identifying high-efficiency systems (Dunham and Iverson, 2014).

Brayton cycle

The simple Brayton cycle uses gas as a working fluid and consists of four stages which the working fluid must go through: compression, heating driven by the heat source, expansion through a turbine (this is where the mechanical work is produced) and heat rejection (cooling) to the initial state. These cycles are able to operate at temperatures much higher than other cycles and thus increase the potential for a higher thermal efficiency. A caveat is, however, the compression stage that occurs in the vapour phase region of the working fluid which uses a significant portion of the produced work.

CO_2 recompression Brayton cycles have been shown to have thermal efficiency potentially exceeding 60% at high pressures (above 30 MPa) and temperatures exceeding 1000 °C, when wet cooling is applied (Dunham and Iverson, 2014).

Despite the low heat capacity of a gas and the high energy cost of compression, it is this potential combined with its simplicity and the fact that a freely available working fluid, such as air, can be used that makes the Brayton cycle such an attractive option for solar thermal power generation.

Rankine cycle

The Rankine cycle is widely used for power generation due to its simplicity. It functions similarly to the Brayton cycle, except that the Rankine cycle's working fluid undergoes phase change: vaporising during the heating stage and condensing back to its initial phase during heat rejection stage. While operating in solar power applications, the majority of Rankine cycles use an intermediate HTF (like molten salt or thermal oils) to transfer the heat from the solar collector field to the thermodynamic loop which is normally operated with water as working fluid. Alternatively, the working fluid from the thermodynamic power block can be led directly to the solar collector to be heated, thus eliminating the intermediate HTF, which is referred to as direction steam generation (DSG).

DSG systems demonstrate high solar use efficiency. Furthermore, line-focused DSG technologies can successfully achieve temperatures up to 773.15 K and improve the performance of solar thermal power plants due to its low irreversibility at the heat recovery steam generator and high thermal efficiency in the solar field.

The steam Rankine cycle is shown to offer high thermal efficiencies (up to 47.5%) at temperatures ranging to 600 °C but different materials for its components might have to be considered above this due to the material limitations of standard ferritic steels (which is commonly used).

Kalina cycle.
The Kalina cycle uses a solution of two fluids with different boiling points as working fluid, such as ammonia and water. The effective boiling point keeps on changing as the mixture is vaporized which leads to a better match in temperature profiles with the heat source and permits more energy to be transferred to the working fluid with a lower exergy destruction rate.

For solar thermal power system, the simple Rankine cycle exhibits better performance than the Kalina when the heat input is only from one heat source at a fixed and relatively uniform temperature. However, when using a two-tank molten-salt storage system as the primary source of heat input, the Kalina cycle could show an advantage over the simple Rankine cycle due to about a 33% reduction in the storage requirement.

At present, implementation with geothermal energy is the only viable renewable energy application of the Kalina cycle. Little success has been achieved at temperatures above 700 K.

Combined cycle
Various thermodynamic cycles can be combined to increase the efficiency of the resultant system.

A Rankine compression gas turbine has been investigated that would offer thermal efficiencies of over 40% according to thermodynamic calculations (Ouwerkerk and de Lange, 2006).

A triple combined cycle, utilizing gas, water and ammonia in a Brayton/Rankine/Rankine configuration was investigated that could achieve a thermal efficiency of 60% when working at a fixed inlet temperature of 1400 K for the Brayton cycle (Marrero et al., 2002).

Combining different thermodynamic cycles could thus result in the highest thermal efficiencies, although this comes with the extra complexity of designing a system with multiple cycles. Due to its simplicity, the Brayton or Rankine cycles seem to be the best option for experimental high temperature solar power generation systems.

2.3 Thermal energy storage

Thermal energy storage (TES) systems can be used to increase and optimize a plant's annual performance (Coco-Enríquez et al., 2015). There are several advantages to TES when compared to mechanical, electrical or chemical storage technologies. TES generally have lower capital costs and relatively high or comparative operating efficiencies when compared to other storage technologies (Kuravi et al., 2013).

A TES system mainly consists of three parts: the storage medium, the heat transfer mechanism and the container. Depending on the type of storage, there are several requirements that need to be met to ensure optimal storage and the longevity of the system. These requirements include (Herrmann and Kearney, 2002)**:**

1. High energy density in the storage material.
2. Good heat transfer between the heat transfer fluid (HTF) and the storage medium.
3. Mechanical and chemical stability of the storage material.
4. Chemical compatibility between HTF, heat exchanger and storage medium.
5. Complete reversibility for a large number of charging/discharging cycles.
6. Low thermal losses.
7. Low cost.
8. Low environmental impact.

In addition to considering these requirements when choosing a TES system, the nominal temperature drop and specific enthalpy drop in the load, the maximum load, the operational strategy and the integration of the TES into the plant, are further plant-specific requirements that need to be considered in deciding on a storage system.

Different methods of TES exist, including sensible heat, latent heat and chemical storage – shown in Figure 4. An overview of these TES techniques and energy densities are given in Figure 5. Sensible heat storage has lower operational costs but also much lower energy densities. Liquid or solid materials can be used for sensible heat storage – examples include water, molten salts or liquid metals for the former and ceramics and metals for the latter. Latent heat storage media are more expensive but offers higher energy densities. The main types of latent heat storage are between liquid and gas phases, liquid and solid, just solid and solid and solid and gas. Thermochemical storage has the highest energy density but research on it is relatively scarce (Ataer, 2006)**.**

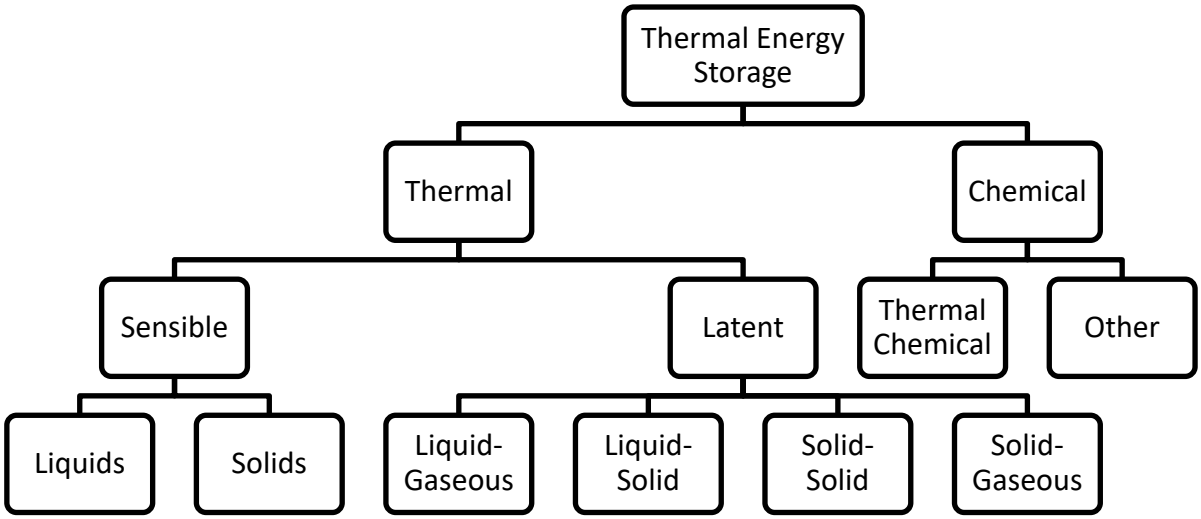

Figure 4 Thermal energy storage techniques.

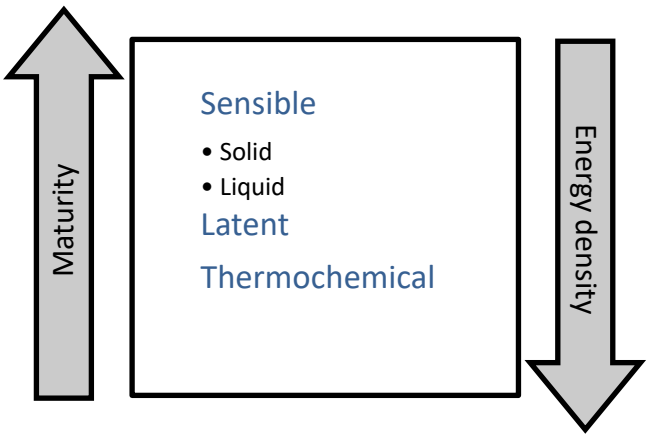

Figure 5 Maturity status of storage technology(Tamme et al., 2005).

Sensible storage is the most mature method of TES but it is not the most energy dense. Thermochemical storage, alternatively, has not yet been developed sufficiently to be a viable option when considering a TES system. It is thus important to perform a trade-off on the availability of the technique versus the resources available when selecting storage system.

Once a system has been chosen, it is important that it performs optimally. For that purpose, the thermal efficiency of a TES system can be defined as:

$$\eta_{th} = \frac{\text{Energy recovered}}{\text{Energy input}} \tag{2}$$

An alternative definition splits the numerator into energy recovered and energy remaining in the TES and the denominator into energy input and energy originally in the TES (Kuravi et al., 2013). Both definitions are valid but can yield different results in different circumstances and care should thus be taken when deciding on which definition to use.

The thermal energy stored by sensible, latent and thermochemical storage can be calculated as summarised below(Sharma et al., 2009):

Sensible:

$$Q = \int_{T_\mathrm{i}}^{T_\mathrm{f}} mC_\mathrm{p}\,dT \tag{3}$$

$$Q = mC_{\mathrm{p,ave}}(T_\mathrm{f} - T_\mathrm{i}) \tag{4}$$

Where Q is the energy quantity (measured in joules), m is the mass of the storage medium, $C_{\mathrm{p,ave}}$ the average specific heat between the initial temperature, T_i, and the final temperature, T_f.

Latent:

For general PCMs:

$$Q = \int_{T_\mathrm{i}}^{T_\mathrm{m}} mC_{\mathrm{p,i}}dT + m\phi H_\mathrm{f} + \int_{T_\mathrm{m}}^{T_\mathrm{f}} mC_{\mathrm{p,f}}dT \tag{5}$$

$$Q = m[C_{\mathrm{p,i}}(T_\mathrm{m} - T_\mathrm{i}) + \phi H_\mathrm{f} + C_{\mathrm{p,f}}(T_\mathrm{f} - T_\mathrm{m})] \tag{6}$$

Here T_m is the phase change temperature of the PCM, ϕ the mass fraction of PCM that has changed phase, H_f the latent heat of phase change of the PCM and $C_{\mathrm{p,i}}$ and $C_{\mathrm{p,f}}$ the specific heat for the initial and final phases respectively.

For thermochemical:

$$Q = \phi_\mathrm{r} m \Delta h_\mathrm{r} \tag{7}$$

Here ϕ_r and Δh_r are the mass fraction of the material that has reacted, and the endothermic heat of reaction respectively.

Amongst all the TES techniques considered, latent heat thermal energy storage is a particularly attractive solution. It presents high energy density and the technology has already been developed enough for commercial implementation. Another advantage is its ability to store heat at a constant temperature corresponding to the phase change temperature of the PCM in use, which is an important consideration for efficient power production, particularly if a relatively constant thermal efficiency is required, or when the heat input mechanism itself into the thermodynamic cycle uses phases change, such as boiling in the Rankine cycles.

2.4 Latent heat thermal energy storage through use of phase change materials

As mentioned, latent heat storage is one of the most efficient ways of storing thermal energy because it provides much higher storage density than sensible heat storage, with a smaller temperature difference between storing and releasing heat (Farid et al., 2004). This is true because it makes use of the latent heat during phase transitions to absorb or release energy within a narrow temperature band. Therefore, PCMs have been widely used in latent heat TES due to their high energy densities owing to their high latent heat of fusion compared to other storage solutions (Pelay et al., 2017).

PCMs can be operated in solid-solid, solid-liquid, solid-gas, and liquid-gas transitions. During solid-solid transition the intension is for the material to undergo a crystalline change. This results in a relatively small changes in volume and a relatively small latent heat. The stable volume makes it easier to contain the PCM, but its low associated energy density makes it less attractive as a TES option. Solid-gas and liquid-gas transitions are characterised by relatively high latent heat, but are also associated with large changes in the specific volume. This makes it difficult to contain the PCM and poses other practical problems. Solid-liquid transition, however, involves comparatively small volumetric changes, but at acceptable latent heat values, which makes it economically attractive. Therefore, solid-liquid PCMs are the focus of this investigation.

An effective latent heat energy storage system is characterised as follows:

- A suitable PCM with its phase change temperature within the desired range.
- A suitable container compatible with the PCM.
- A suitable heat exchange surface.

These aspects are discussed in more detail in the following sub sections.

2.4.1 Thermophysical material properties

A PCM should be chosen according to its thermodynamic, physical, kinetic and chemical properties, and are to satisfy certain criteria.

Thermally the material should have a phase-change temperature that is suitable for the application, a high latent heat of phase change, and possess good heat transfer properties. Desirable physical properties include having phase stability during solidifying, high density (which decreases the container size), small volume change during phase change, and low vapour pressure (which will make containment significantly easier).

The most important kinetic property is an aversion to supercooling, which is the lowering the temperature of the material below its freezing point without it solidifying. In such a scenario, it means only sensible heat is stored which negates the advantages of latent heat storage. Long-term chemical stability of a PCM should also be considered, along with its compatibility with any materials it comes in contact with (including containers), its toxicity and flammability.

Lastly, and most importantly for commercial applications, the economic viability of a PCM should be considered: availability, abundance and cost effectiveness are some of the factors to be weighed.

As mentioned in the previous chapter, PCMs can be classified into sub-categories in terms of its material type. These are: organic, inorganic or eutectic. The different material types of PCMs and their sub-classes are illustrated in Figure 6. Organic compound PCMs can be divide into paraffin and non-paraffin (esters, acids and alcohols) compounds. Inorganic compound PCMs include salt hydrates and metals. Eutectic compounds PCMs are a homogeneous mixture of organic and inorganic compounds with single phase change temperature, which is usually lower than the phase change temperature of any of the constituents.

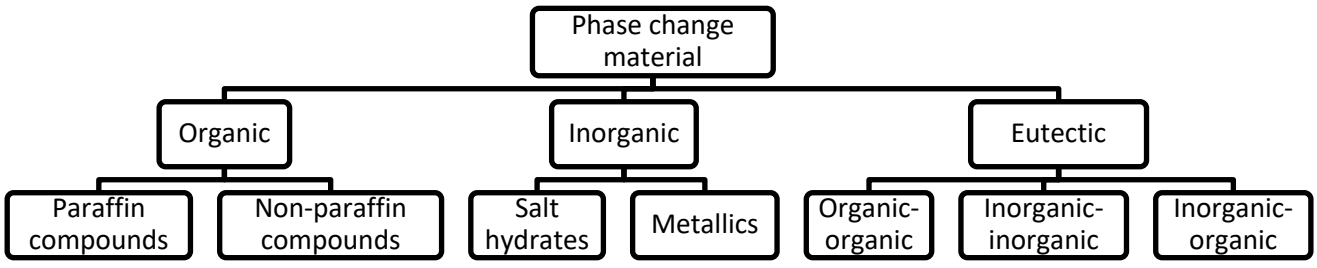

Figure 6 Classification of solid-liquid PCMs (Xu et al., 2015).

In general, inorganic compounds have almost double the volumetric latent heat storage capacity (250 - 400 kg/dm^3) compared to organic compounds (128 - 200 kg/dm^3) while eutectic PCMs can be made to suit the specific needs of the application.

There are a large number of PCMs with a wide range of melting/solidifying temperatures available. Organic substances tend to have lower melting temperatures and are mostly applied for thermal comfort heating or cooling, protection of electrical devices or bio-climatic building/architecture. Inorganic substances have higher melting temperatures and have multiple applications in the field of solar storage (Agyenim et al., 2010).

The advantages and disadvantages both of organic and inorganic PCMs are listed in Table 1. Eutectics are just a mixture of organics and/or inorganics and are thus not listed.

Table 1 Comparison of organic and inorganic materials for heat storage.

	Organic	Inorganic
Advantages	• Non-corrosive • Low or no supercooling • Chemical and thermal stability	• Greater phase change enthalpy
Disadvantages	• Lower phase change enthalpy • Low thermal conductivity • Flammability	• Supercooling • Corrosion • Phase separation • Phase segregation, lack of thermal stability

Various inorganic PCMs, eutectic and non-eutectic, are listed in Table 2 to Table 4 along with their thermodynamic properties, based on the information compiled using reviews done by Zalba et al. (2003), Khare et al. (2012) and Xu et al. (2015).

No organic substances are listed since most of these have phase change temperatures too low for use in medium to high temperature (approximately above 300 °C) solar power generation.

Table 2 Salt hydrates with potential use as PCM.

Compound	**Melting temp [°C]**	**Heat of fusion [kJ/kg]**	**Thermal conductivity [W/m.K]**	**Density [kg/m^3]**
$ZnCl_2$	280	75	0.5 (liquid)	2907 (solid)
$NaNO_3$	306	178	0.5 (liquid)	2260 (solid)
KNO_3	336	116	0.5 (liquid)	2110 (solid)
KOH	380	149.7	0.5 (liquid)	2044 (solid)
NaCl	800	492	5 (liquid)	2160 (solid)
Na_2CO_3	854	275.7	2 (liquid)	2533 (solid)
K_2CO_3	897	235.8	2 (liquid)	2290 (solid)

Table 3 Metallics with potential use as PCM (Khare et al., 2012).

Compound	Melting temp [°C]	Heat of fusion [kJ/kg]	Thermal conductivity [W/m.K]	Density [kg/m^3]
Aluminium, commercial purity	661	388	186 (liquid)	2700 (solid)
88Al:12Si	576	560	160 (liquid)	2700 (solid)

Table 4 Inorganic eutectics with potential use as PCM.

Compound (weight %)	Melting temp [°C]	Heat of fusion [kJ/kg]	Thermal conductivity [W/m.K]	Density [kg/m^3]
Na_2CO_3-Li_2CO_3 (56:44)	496	370	2.09 (liquid)	2320 (solid)
NaF-MgF_2 (75:25)	650	860	1.15 (liquid)	2820 (solid)
LiF-CaF_2 (80.5:19.5)	767	816	1.7 (liquid) 3.8 (solid)	2390 (solid)

Notable among inorganic substances are hydrated salts, which exhibit higher energy storage densities and thermal conductivities. Unfortunately, they experience supercooling and phase segregation at higher temperatures, and hence require the use of some nucleating and thickening agents in their application (Farid et al., 2004). The high thermal conductivity of metallics PCMs make them very attractive options for LHS, however, their high costs mean they are not easy to consider as practical choices for LHS systems.

2.4.2 Containment methods

Once a PCM has been selected, based primarily on the temperature range of application, the next important selection to make is the containment method of the PCM. The main factors that influence the suitability of a container are:

- The geometry of the container.
- The thermal interaction between the container and the PCM.

Both of these factors have a direct influence on the heat transfer characteristics and ultimately the phase transition time and performance of the PCM storage unit. There has to be effective heat exchange between the PCM and whichever energy transport mechanism (such as a HTF) is used to and from the PCM. Container geometries are typically chosen with the purpose that either the heat transfer area or the convective heat transfer coefficient between PCM and HTF is maximised (Xu et al., 2015). The most common shapes for PCM containers are rectangular cavities, spherical capsules and tubes (including long thin heat pipes) or cylinders (Dhaidan and Khodadadi, 2015).

The most important criteria that have limited widespread use of latent heat stores, are the useful life of PCMs-container systems and the number of cycles they can withstand without any degradation in their properties. Insufficient long-term stability of the storage materials is due to two factors: poor stability of the materials properties and/or corrosion between the PCM and the container (Farid et al., 2004).

2.4.3 Heat transfer enhancement

As indicated, a significant challenge associated with most high-density energy storage PCMs (organic, inorganic salt hydrates and non-metallic eutectics) is their low thermal conductivities (see Table 2 and Table 4). To counter this, heat transfer enhancement techniques are required (Velraj et al., 1999).

The overall thermal conductivity of a PCM TES system can be enhanced in a number of different ways, including:

- Extended surfaces (fins).
- Multi-tubes.
- Micro- and macro-encapsulation.
- Metal rings – especially effective for improved solidification.
- Bubble agitation – especially effective for improved melting.
- Dispersion of high conductivity particles (like graphite) in the PCM.
- Embedding a metal or graphite matrix structure in the PCM.

These techniques are illustrated in Figure 7 along with a few other methods.

The most widely implemented heat transfer enhancement techniques are based on either the application of extended surfaces via highly conductive fins, or the introduction of high conductivity matrices made from materials such as carbon fibre and brushes and multi-tubes. Fins are the most common technique due its simplicity, both in fabrication and application, and low cost (Agyenim et al., 2010).

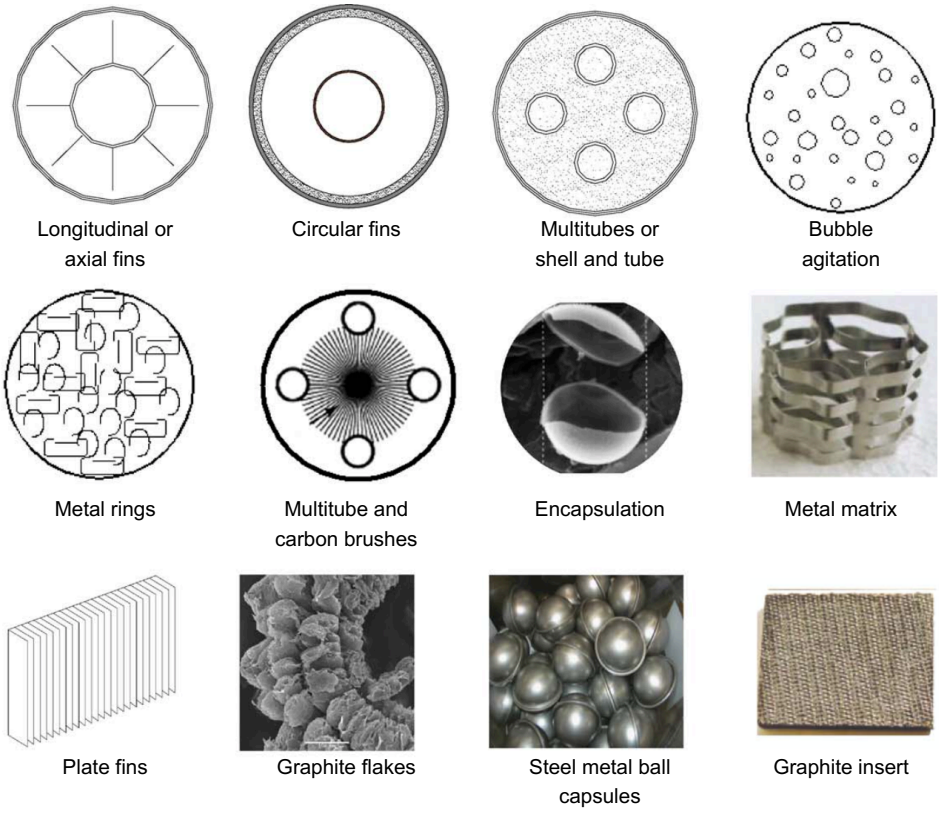

Figure 7 Heat transfer enhancement techniques (Agyenim et al., 2010).

The use of fins has the advantage of being effective during the melting and solidification processes of a latent heat storage cycle. Heat transfer during the melting process is dominated by convective heat transfer and conductive heat transfer decreases as the process progresses, whilst the inverse occurs during solidification. An effective fin configuration in the PCM container could accelerate both these processes by enhancing the conductive heat transfer throughout the PCM (Sivasamy et al., 2018). The fin configuration can be optimised by adjusting a number of parameters, including the orientation, material, thickness, length and spacing of the fins.

A number of studies have been done on the viability of fins as heat transfer enhancement technique for latent heat thermal energy storage systems.

Velraj et al. (1999) conducted an experimental study to investigate, amongst other techniques, longitudinal fins inside a paraffin filled vertical cylindrical tube and found that the addition of fins decreased the time required for completed solidification by approximately 75% while only occupying 7% of the tube volume. Pizzolato et al. (2017) attempted to accelerate the melting and solidification times inside a shell-and-tube LHS unit by performing topology optimisation of its longitudinal fins and found optimal layouts that differ significantly between solidification and melting. Their study also highlighted the importance of modelling natural convection in phase change design optimisation studies.

Debich et al. (2020) performed a numerical design optimisation of a PCM-based plate fin matrix heat sink. The number of enclosures in the matrix and the PCM volume fraction were optimised. They found that a 100% volume fraction of PCM (the cavities were completely filled) was able to store more energy during charging and dissipate it at a lower rate during discharging. Similarly, fewer enclosures (and thus fewer fins) resulted in slower energy absorption and dissipation, alternatively more enclosures resulted in a higher energy transfer rate during charging but especially during discharging.

Sharifi et al. (2011) and Kamkari and Shokouhmand (2014) both investigated the effect of internal partial fins on the melting rate of a PCM in a rectangular enclosure. The former conducted a numerical study and the latter experimental, but both concluded that even though increasing the fin length and the number of fins in an enclosure hinders natural convections currents, it still increased the overall heat transfer rate of the system. This was confirmed by De Césaro Oliveski et al. (2021) who investigated the effect of the fin aspect ratio on the melting process and found that longer, thinner fins resulted in higher melting rates. Additionally, Kamkari and Shokouhmand (2014) concluded that an optimum number of fins in an enclosure (and thus fin pitch) must exist, but further investigation is needed to determine what the optimum is.

Abdulateef et al. (2018) conducted a review of various literature studies done on the geometric and design parameters of fins used in LHS systems and concluded that the heat transfer rate is most dependent on the number of fins in an enclosure. They, however, also found that an increase in a number of fins did not significantly improve the heat transfer rate in some cases.

2.5 TES applications using PCM

There are numerous practical applications of TES making use of PCMs. Sharma et al. (2015) conducted a review of organic solid-liquid PCMs and their application in thermal energy

storage for domestic and industrial cases. Encapsulated PCMs can be incorporated in building walls (in wallboards), floors and ceilings (in ceiling boards) to absorb solar energy and maintain the internal temperature of a building for longer.

The effect of natural convection in PCM wallboards was investigated by Liu and Awbi (2009) who experimentally found that during charging the PCM provided improved heat-insulation and releases more heat during discharge than a normal wall. This increased energy exchange between the air inside the building and the wallboard resulted in a higher calculated convective heat transfer coefficient.

Butala and Stritih (2009) investigated how PCM impregnated floor and ceiling boards could improve the cooling of a building by absorbing additional heat and melting during the day and solidifying and releasing the absorbed heat energy during the cooler evening. They found this technique resulted in cooler temperatures in the building compared to a building without PCM floor and ceiling boards.

The high energy density of PCMs makes them an attractive alternative option in passive thermal management in electronic devices (where space is generally limited) over active convective air based thermal management systems, offering advantages such as simplified designs (due to fewer moving parts), compactness and high efficiency with cooling systems.

Baby and Balaji (2013) investigated the thermal performance of PCM based pin fin heat sinks versus heat sinks without pin fins and found that pin fins increased the performance and the life time of the device on which the heat sink is installed. They developed an Artificial Neural Network – Genetic Algorithm hybrid algorithm which helped determine that an optimum pin fin configuration exists for the heat sink studied.

The lower melting temperatures of organic PCMs also make them ideal for lower temperature energy storage in solar water and air heating and solar dryer applications. In solar water heating applications there are numerous different configurations to employ PCMs as TES, including placing microencapsulated PCM in the water storage tank. The PCM melts and absorbs heat during charging and releases heat during discharge resulted. Fazilati and Alemrajabi (2013) employed this method and found the spherical encapsulated PCM increased their tank's energy density by 16% and the solar water heater could supply hot water for 25% longer.

Alternatively, the PCM can be housed in a storage separate from the water storage tank. Hot water from the solar collector can be diverted past the PCM (melting it) on the way to the water storage tank during charging and from the water tank, cold water flows back to the solar collector to be reheated. During discharge the solar collector can be excluded from the loop and the cold water can be reheated by flowing past the melted PCM (extracting heat and solidifying the PCM) and back to the water tank.

Mahfuz et al. (2014a) investigated the performance of such a system using a shell and tube PCM filled TES system. Their system, shown in Figure 8, lead the water past the TES storage using a secondary loop. When the solar collector is in use valve 1 would be open and valve 2 closed. When energy needs to extracted from the TES valve 1 would be closed and valve 2 opened causing the cold water to flow past the TES to be heated. They found the addition of a TES using PCM improved the performance of the system.

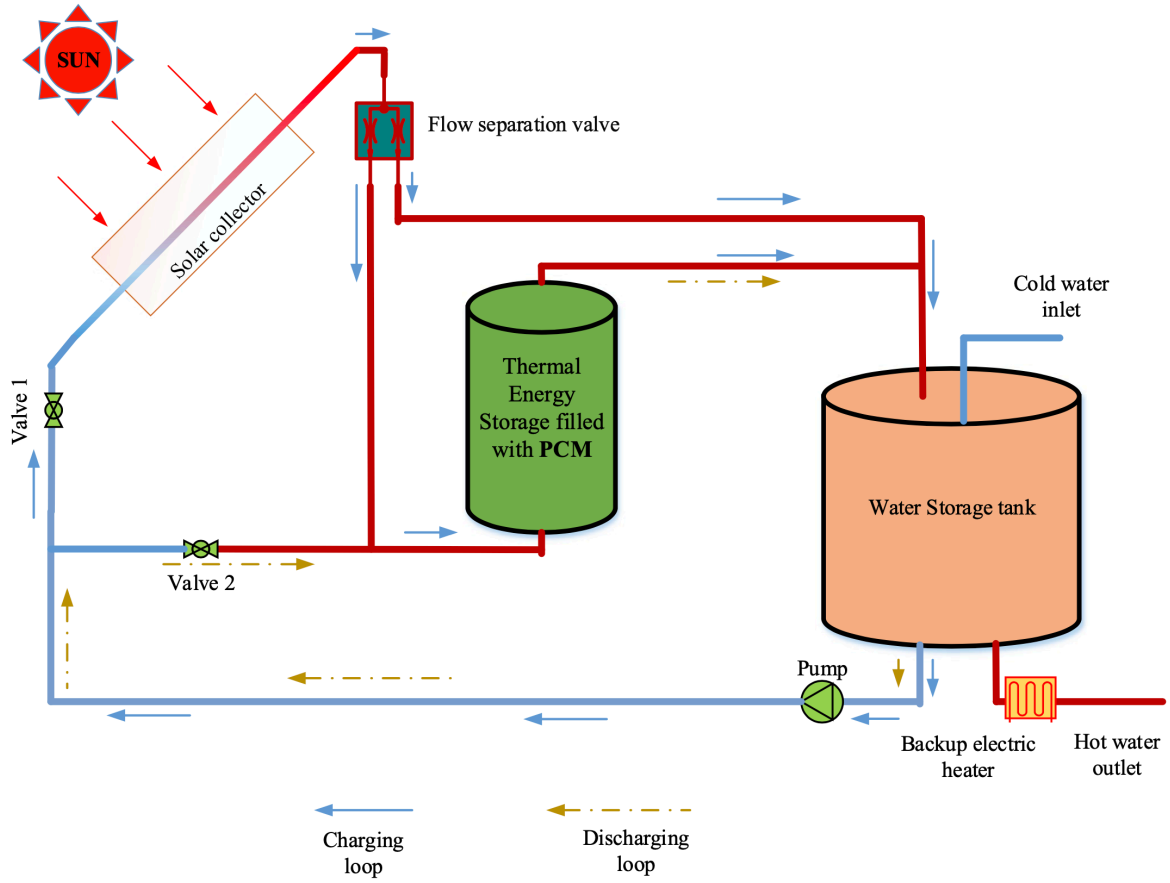

Figure 8 Solar water heating system with PCM TES (Mahfuz et al., 2014a).

Solar thermal power generation systems that make use of TES using PCM make use of very similar configurations as the one shown in Figure 8. The solar collector would just be replaced by a solar field, the water storage tank by a thermodynamic power cycle and, depending on the power cycle, another HTF used instead of water.

In a newer study Mahfuz et al. (2014b) compared the thermodynamic performance of a thermal power system with and without PCM storage. An operational solar power plant, near Shiraz in Iran, was used for the analysis. A schematic of the system in Figure 9, shows how a similar configuration as the one employed for the solar water heating system in Figure 8 is used for power generation applications. In the power plant, an oil is used as the HTF in the parabolic trough solar collector field and TES cycle, while water is used as the HTF in the thermodynamic (Rankine) cycle. It was found that the overall exergy efficiency increased from about 10% in the system without PCM to 30% in the system with.

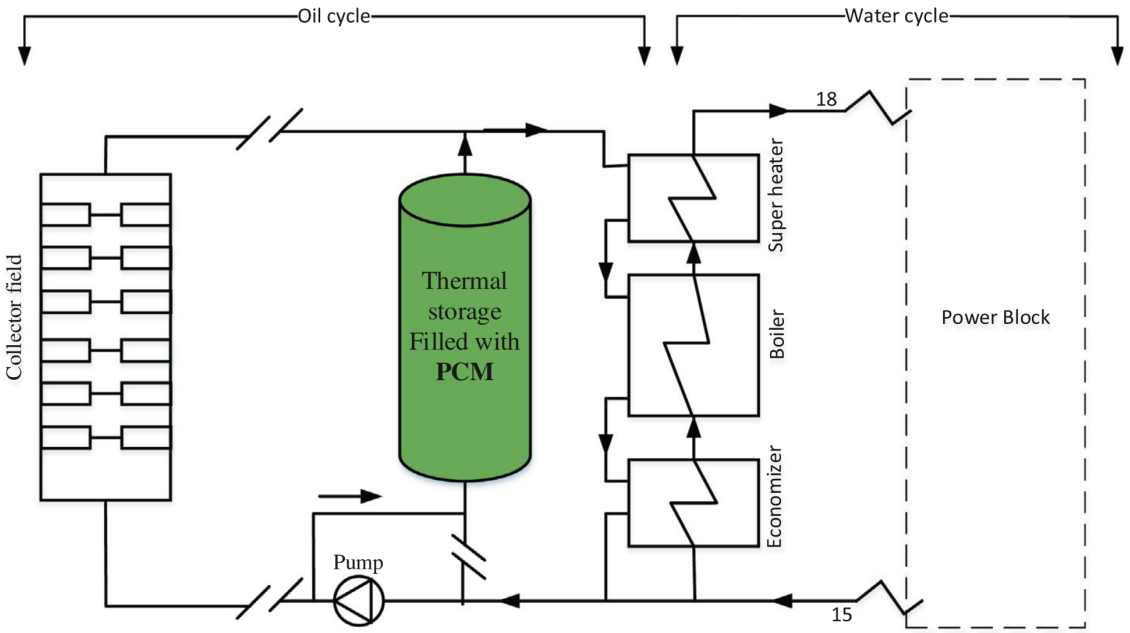

Figure 9 Schematic of a solar thermal power plant with PCM TES (Mahfuz et al., 2014b)

Robak et al. (2011) performed an economic evaluation of TES in large scale CSP applications. A new latent heat energy storage concept, using embedded thermosyphons as heat transfer enhancement, is compared with a two-tank sensible heat energy storage system and it was found that the latent heat system is economically competitive with the sensible storage with the potential to reduce capital costs by at least 15%.

Li et al. (2019) conducted a review of shell and tube molten salt PCM TES devices for medium and high heat applications. They investigated performance enhancements of such systems, considering different device orientations as seen in Figure 10, and found that both the operating conditions and geometrical parameters have a significant impact on the system's performance. The HTF inlet temperature and inlet velocity was found to increase the melting rate and overall heat capacity of the system, with the velocity having a bigger impact. The orientation of the device was also found to play a vital role in the effect of natural convection in the system which has a big impact on the heat transfer performance. Conflicting reports have, however, been found in the literature and it was suggested that further investigation is necessary on this.

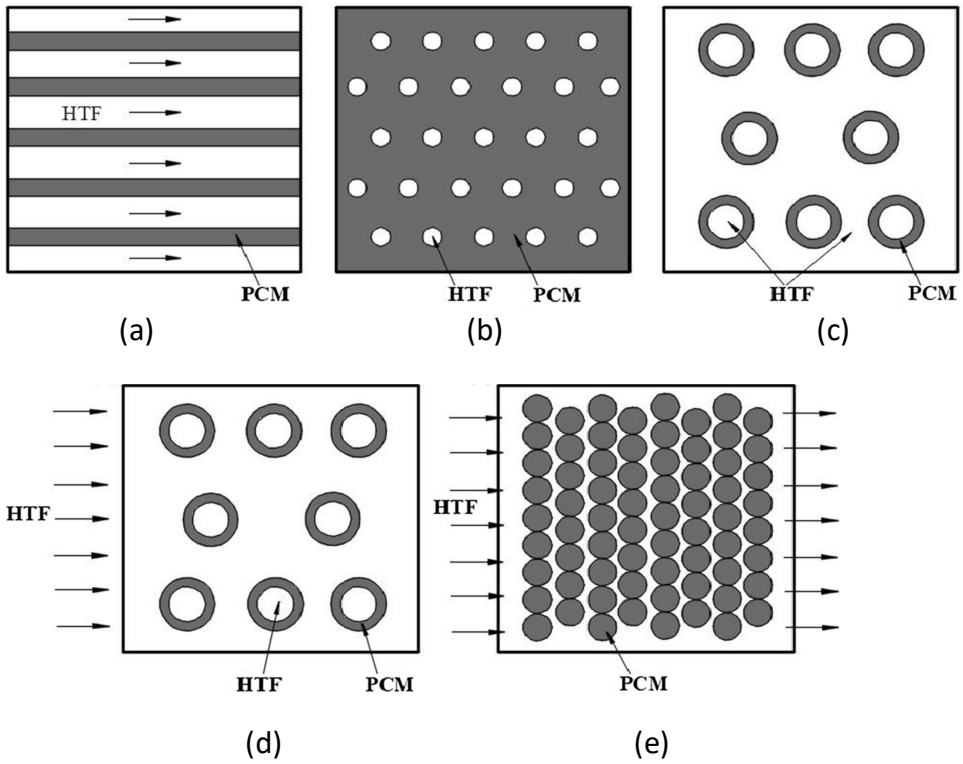

Figure 10 Different TES device orientations (a) flat plate (b) shell and tube - internal flow (c) shell and tube - parallel flow (d) shell and tube - cross flow and (e) packed bed (Li et al., 2019).

2.6 Heat transfer in PCMs

The study of heat transfer characteristics of melting and solidification processes is one of the most attractive areas in contemporary heat transfer research (Sharma et al., 2009). The two dominant heat transfer mechanisms involved in the phase change problem (in solid-liquid PCMs), are conduction and convection in the liquid phase (more specifically natural convection).

The earliest literature analyses simplified the heat transfer by only considering one-dimensional conduction in pure substances – studies were done on ice formation by Lamé and Clapeyron in 1831 and Stefan in 1891. Precise solutions to more general phase change problems were first presented by F. Neuman in 1912 before the process of ice formation for a cylinder, sphere and flat plate was analysed in 1943 by London and Seban (1943).

In 1978 work on the natural convection effects in an annular geometry using hydrated salts and waxes/paraffins, was published by Marshall (1978). He was first to show that the existence of natural convection has a significant impact on the melting time of PCMs and recommended the use of natural convection to enhance the heat transfer in substances with low thermal conductivities. Similarly, Bathelt et al. (1979) studied solidification around a horizontal cylinder and using photographs, he indicated the importance of natural convection.

In 1983 a thermal storage experimental study was carried out using an immersed tubular heat exchanger in a PCM (using salt hydrates and fatty acids). A theoretical study was developed using the enthalpy method and solved only for conduction (disregarding convection). When comparing the experimental and theoretical results, significant

discrepancies were found in melting. It was therefore concluded that it is necessary to model natural convection in the liquid (Achard et al., 1983).

2.6.1 Heat transfer mechanisms during phase change

The dominant mechanism of heat transfer differs depending on whether a PCM is melting or solidifying. During the early stages of melting, conduction will dominate heat transfer for as long as the viscous force opposes the fluid motion (due to buoyancy). This results in an almost uniform phase change front. As time progresses and more of the PCM melts, the buoyancy force becomes large enough to overcome the viscous force which leads to natural convection starting the heat transfer (Shokouhmand and Kamkari, 2013). Circulating currents start to form due to the natural convection which accelerate the phase change process due to the additional heat transfer mechanism until the PCM is completely melted.

The influence of convection, considering an effective thermal conductivity (k_{eff}), can be expressed as (Farid and Husian, 1990):

$$k_{\mathrm{eff}} = cRa^{n}k_{\mathrm{l}} \tag{8}$$

where k_{l} is the liquid PCM heat conductivity, c and n are empirical constants dependant on the geometry of the storage and the Rayleigh number, Ra, is given by:

$$Ra = \frac{g\beta C_{\mathrm{p,l}}(T_{\mathrm{w}} - T_{\mathrm{m}})L^{3}}{\mu k_{\mathrm{l}}} \tag{9}$$

Here g is the gravitational acceleration; $C_{\mathrm{p,l}}$ is the specific heat of the liquid PCM; β is the thermal expansion coefficient of the liquid PCM; T_{w} is the heat source wall temperature and T_{m} is the melting temperature of the PCM. L is the melt layer thickness, μ the viscosity of the liquid PCM; and k_{l} the liquid PCM thermal conductivity.

The solidification process can also be classified into two distinct stages. Initially solid PCM particles start to form close to the heat transfer surface and are suspended in the liquid PCM, but since the surrounding temperature is still higher than the melting point, the solid particles re-melt. Once the temperature of the liquid PCM becomes low enough, the forming solid particles grow larger and accumulate at the bottom of the enclosure due to its higher density compared to the surrounding liquid (Wang et al., 2015). In the first stage natural convection still dominates the heat transfer due to the PCM being mostly liquid. The forming of solid PCM however significantly slows down the buoyancy forces in the enclosure and conduction takes over as the dominant heat transfer mechanism.

2.6.2 The moving boundary problem

In 1889 Stefan posed the moving boundary problem (for water/ice as the PCM) as follows (Stefan, 1889):

The heat conducting material occupies the space $-\infty < X < \infty$, where X is the surface position of the moving boundary. At the initial time, the liquid phase fills the domain $0 < X < \infty$ at temperature $\mathrm{T_l} > 0\ ^{\circ}\mathrm{C}$ while the solid occupies the domain $-\infty < X < 0$ at temperature $\mathrm{T_s} < 0\ ^{\circ}\mathrm{C}$. At $X = 0$, it is maintained at constant temperature $\mathrm{T} < 0\ ^{\circ}$, under the effect of which the solidification occurs isothermally at temperature $\mathrm{T_m} = 0\ ^{\circ}\mathrm{C}$ without super-cooling and

conduction is the mode of heat transfer in the material. The energy equation at the solid-liquid interface given by Stefan is:

$$H_{\mathrm{f}}\rho\left(\frac{dX(t)}{dt}\right) = k_{\mathrm{s}}\left(\frac{\delta T_{\mathrm{s}}}{\delta t}\right) - k_{\mathrm{l}}\left(\frac{\delta T_{\mathrm{l}}}{\delta t}\right) \tag{10}$$

where H_{f} is the latent heat of fusion and $X(t)$ is the surface position of moving boundary at time t.

A general representation of the progression of the moving boundary, during solidification, is shown in Figure 11.

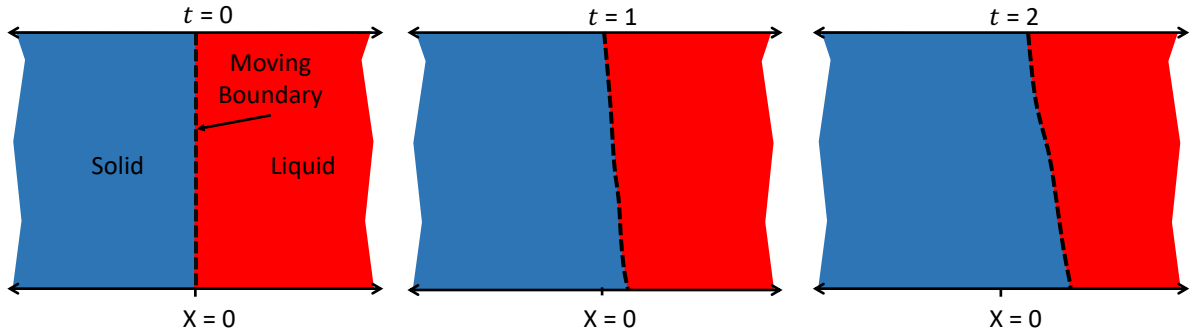

Figure 11 Moving boundary progression with time.

The analysis of phase change (melting and solidification) heat transfer problems, called moving boundary problems (or the Stefan problem) in scientific literature, is especially complicated due to the fact that the interface or boundary between the solid and liquid phases moves depending on the rate at which the latent heat is absorbed or released at the boundary. The position of the boundary is thus not known beforehand and forms part of the solution.

2.6.3 Solutions to the moving boundary problem

Various analytical and numerical methods exist to solve the moving boundary problems, each method with its own merits and disadvantages (Henry and Stavros, 1996).

Analytical

Analytical methods are mainly used to validate numerical models before they are implemented. Different analytical methods include Neumann's method (which is valid for semi-infinite problems with parameters constant in each phase and constant initial and imposed temperatures) and the heat balance integral method (which has been extensively applied to different real-world problems).

Numerical

Many approximate analytical techniques exist for solving the Stefan problem, all with a common drawback of these techniques that they are limited to one-dimensional analysis and become very complicated when applied to multidimensional problem.

Numerical methods such as finite element methods (FEM) and finite difference methods (FDM), appear more powerful in solving the moving boundary problem. In general, a time variant grid approach offers good accuracy but is limited to simple problems and geometries.

The fixed grid approach, in which the latent heat of fusion is usually absorbed into the material's specific heat or enthalpy, is much simpler in practical application.

During phase change the solid-liquid boundary moves away from the heat transfer surface. The difficulty in solving a phase change problem is the presence of a moving boundary or region on which heat and mass balance conditions have to be met. This is where methods of latent-heat evolution are introduced.

Fixed grid

Fixed grid methods approximate the heat flow equation by finite difference replacements for the derivatives in order to calculate the temperature at each location-node and time on a fixed grid in the space-time plane. At any time, the moving boundary will be located between two adjacent grid points. The numerical solution of the method is carried out on a space grid that remains fixed throughout the calculation.

The new temperature is calculated from temperatures at the previous time step for each node up to the phase change interface. The temperature variation at the boundary is then calculated by implementing the latent heat of fusion.

Fixed grid methods are capable of handling multidimensional problems efficiently with ease. The moving boundary can thus be handled numerically through simple modifications of existing heat transfer methods. They have become a common method of modelling a variety of complex moving boundary problems because of this reason.

A disadvantage of the fixed methods is that they sometimes fail when the boundary moves a distance greater than one space increment in a single time step. This constraint, which is dependent on the velocity of the moving boundary, could cause significant increases in memory usage (due to larger arrays) and thus calculation time. These problems can be avoided by using variable grid methods.

Variable grid

In the variable grid methods, the exact location of the moving boundary is evaluated on a grid at each step. The grid can be either interface fitting or dynamic.

Interface-fitting grids (or variable time step methods) use a spatial grid with a non-uniform time step and adjusts the time step such that the moving boundary moves a desired distance each time step, instead of applying a fixed time step and then search for the moving boundary. These methods have been repeatedly employed to solve two-phase and one-phase problems.

Dynamic grid methods are based on a variable grid spacing, where the number of spatial intervals is kept constant, but the size of the intervals is adjusted such that the moving boundary will lie on a particular grid point after each time step. The spatial intervals in these methods are thus a function of time.

Methods of latent-heat evolution

The focus of the fixed- and variable-grid methods is on applying finite difference techniques to the strong formulation of the process, locating the moving boundary, and determining the temperatures at each time step. These methods are good choices when solving one-dimensional problems not involving more than two phases. For two-dimensional cases, these

solution methods require much more computational time, and it is even more time consuming and challenging when applied to three-dimensional cases. More complicated schemes must thus be used in these cases.

Alternatively, the problem could be formulated such that the Stefan problem is implicitly incorporated in a few sets of equations, which apply over the entire region of a fixed domain. These methods are called weak numerical solutions, in which the nature of the moving boundary is not given explicit attention. Weak methods include the apparent heat capacity method and effective heat capacity method, the heat integration method, the source-based method, and the enthalpy method. Of these methods, only the enthalpy method is of interest since a variation of this method is used in ANYS Fluent's modelling of solidification and melting.

The enthalpy method was proposed as early as 1946 to avoid nonlinearity in a heat conduction problem (Eyres et al., 1946). It is more complex and expensive than other methods, with the computational cost increasing with the mesh refinement, however, the solutions obtained are accurate, especially for the solidification of a metal in which a phase change temperature range exist. Additionally, the solution is independent of the time step and phase change temperature range.

2.7 Chapter summary

A literature review was conducted to gain a better understanding into the theory involved in thermal energy storage. The various different methods of harnessing solar energy and the thermodynamic cycles used to generate power using the solar energy, were investigated. The different methods of storing solar energy were investigated and it was found that latent heat TES is a promising method in the solar energy field.

Solid-liquid PCMs were identified as the most effective among PCMs. Different solid-liquid PCMs and their thermophysical properties were investigated to determine which materials are best suited for high temperature applications. It was found that inorganic materials (especially hydrated salts) perform best at high temperatures.

The PCM containment method and its geometry can have a big impact on the heat transfer capabilities of a PCM TES system. Different geometries can be used: spherical, cylindrical and rectangular, and heat transfer enhancement techniques (such as fins) can be incorporated in the storage containers.

The main heat transfer mechanisms in phase change processes were identified as conduction and natural convection. The solution of the phase change problem required setup of a special problem formulation: the moving boundary problem (or Stefan problem). This defines what happens at the interface between the solid and liquid phases of the PCM. A number of studies have been done on the using PCMs as a TES system.

In the next chapter the information gathered from literature is used to motivate and present the domain and numerical model that was used in this study.

3. Thermal Energy Storage Application

The TES application under consideration in this study and its geometric layout is defined in this chapter, as well as how it could be represented by a simplified two-dimensional domain suitable for the numerical analysis. The PCM and container material are also selected and their thermophysical properties are discussed.

3.1 Enclosure

Thermal energy storage using PCM can be applied in a number of different layouts and configurations as was shown in Figure 10 of the previous chapter. Each layout might have different heat transfer enhancement techniques. For purposes of this investigation, a TES layout as shown in Figure 12 was selected. It is similar to the Figure 10b and consists of a bank of vertical tubes carrying a HTF, and surrounded by a PCM. As the heat enhancement technique, horizontal plate fins are incorporated and spaced at regular intervals. Therefore, the PCM is present within the volumes between the plates and the HTF tubes.

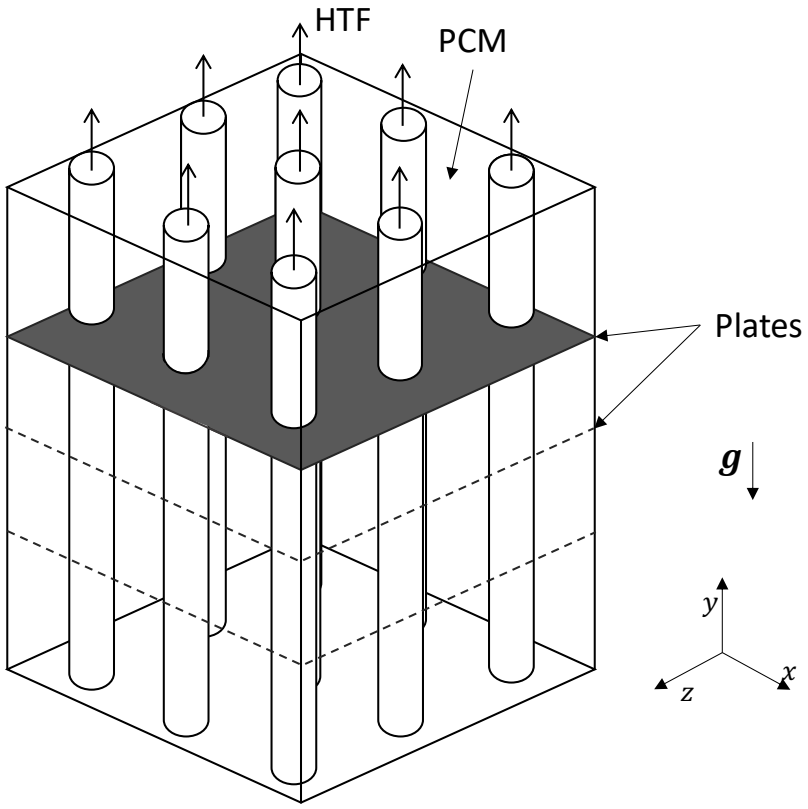

Figure 12 PCM TES application with plate fins.

The HTF tubes can be arranged in a few different ways. Kallannavar et al. (2020) investigated the effect of tube layouts on the performance of shell-and-tube heat exchangers. They studied staggered and inline layouts and reported that a staggered layout resulted in higher heat transfer rates. A top view representation of the TES device in Figure 12 is shown in Figure 13 for a) an inline layout and b) a staggered layout. The characteristic region for each of these cases is shown as the shaded area.

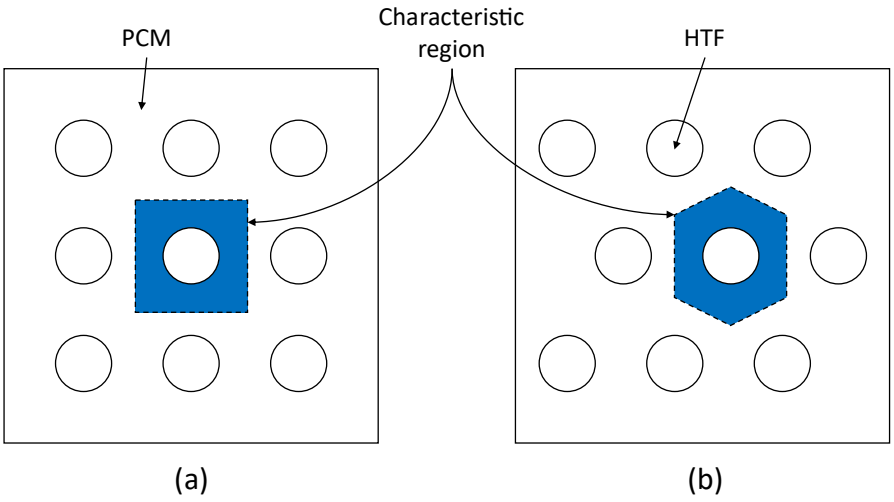

Figure 13 PCM TES tube layout and characteristic region for (a) inline and (b) staggered arrangements.

As a first order approximation, the hexagonal characteristic region can be replaced with a region with a circular profile such that its thermal response will resemble that of the staggered tube arrangement, as is shown in Figure 14a. Typically TES schemes of this nature will consist of a large number of tubes, which for near-adiabatic boundary conditions on the TES outer layers, will result in axisymmetric thermal fields around each tube which can be represented on a two-dimensional plane as is shown in Figure 14b.

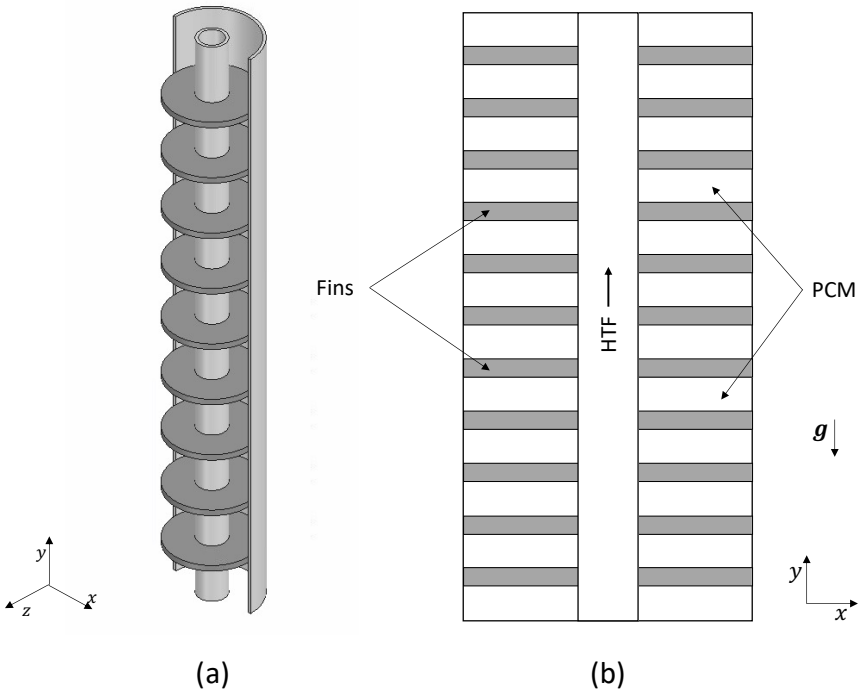

Figure 14 Simplified single shell and tube PCM TES with (a) a three-dimensional representation and (b) a two-dimensional cross section in the vertical plane.

This enables the ability to model the system numerically only in two dimensions instead of three, which will result in a significant computational saving. It also allows the results to be extrapolated and used in different three-dimensional geometries, such as with a rectangular

enclosure or circular fins in a cylindrical enclosure as shown in Figure 2c and d in a previous chapter.

During a discharging cycle colder HTF flows from the thermodynamic cycle through the TES device containing molten PCM. Because of the temperature difference between the PCM and the HTF, the fluid will receive heat along its way. If flow boiling is absent in the HTF, the small vertical fin pitch will result in only a small increase in the HTF temperature from fin to fin, and in the case that flow boiling does occur, the fluid temperature will remain constant. This, combined with the vertical symmetry and the repeating pattern of the PCM cavities and fins means that in order to characterise the phase change process in the PCM, only a single section between two adjacent fins need to be modelled, as is shown in Figure 15. The dimensions of the fin width (L), the fin pitch spacing (P) and the fin thickness (t_f) are also shown with the bottom fin and top fin each contributing half the thickness of a full fin.

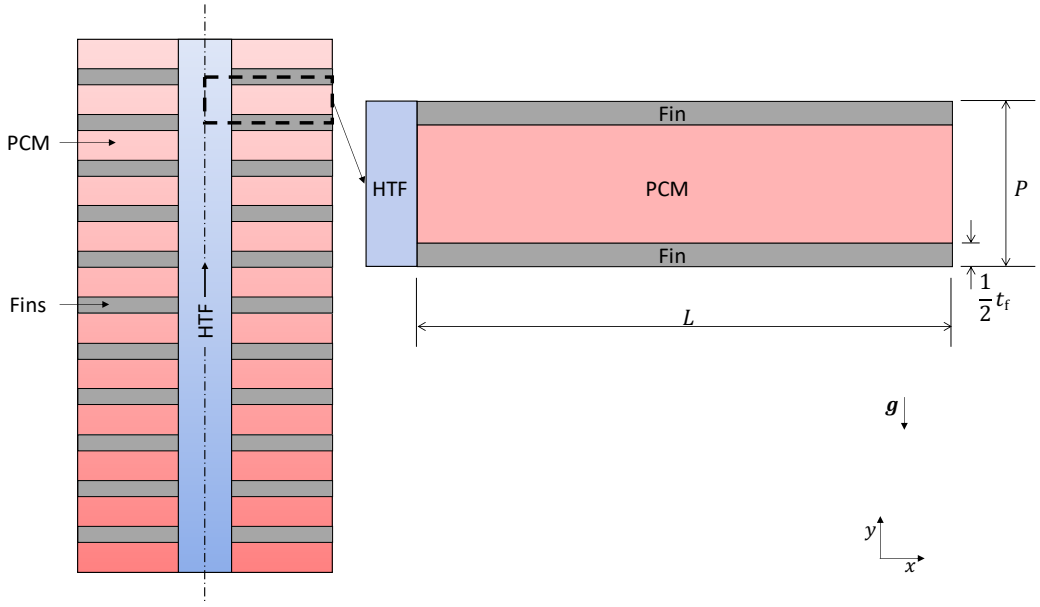

Figure 15 TES enclosure with PCM and its dimensions.

3.2 Materials selection

Motivation of the material selection is given in this section while the relevant material properties of the selected materials are supplied in Table 5 in the next section.

Aluminium was chosen as the fin material because of its high thermal conductivity and low propensity to react chemically with most PCMs and its melting temperature (660 °C) being much higher than the temperatures we will be working with in this study.

A PCM had to be selected based on the criteria defined in the literature review with the availability, affordability and temperature range of the PCM carrying the most weight in the selection process. A PCM melting temperature close to 324 °C was needed, which is the saturation discharge temperature corresponding to a maximised thermal efficiency of a commercial Rankine power cycle operating at 120 bar (Ruiz-Cabañas et al., 2017). The selection of PCMs was thus narrowed down to two materials: potassium nitrate (KNO_3) and sodium nitrate ($NaNO_3$) which have melting temperatures of 333 °C and 306 °C respectively. These two materials are commonly combined to create composite PCMs for specific

applications; composites were, however, not considered within this investigation in order to keep the replication of this numerical study on an experimental scale simpler.

Because of its high latent heat of fusion (according to most literature) $NaNO_3$ was chosen even though its melting temperature is lower than 324 °C. In addition, there appears to be more reliable information on its thermophysical properties in literature than that of KNO_3. Unless stated different, all modelling in the rest of this document was conducted with $NaNO_3$.

3.2.1 Thermophysical properties

For the PCM, the properties that are of interest in modelling the phase change process numerically are the melting, liquidus and solidus temperatures, latent heat of fusion, dynamic viscosity, the volumetric expansion coefficient, as well as its density, thermal conductivity and specific heat capacity in both the liquid and solid phases. For the fin the important properties are density, thermal conductivity and specific heat capacity.

The thermophysical properties of the aluminium enclosure were taken from the ANSYS Fluent properties data base while the properties of the $NaNO_3$ PCM were gathered from various sources in literature. The melting temperature, latent heat of fusion, thermal conductivity, specific heat capacity and volumetric expansion coefficient for this study is based on the values used by Bauer et al. (2012). The thermal conductivity for the solid phase was averaged over three temperature readings given in the reference. Similarly, the specific heat capacity for the solid phase was averaged over six temperature readings. The liquidus and solidus temperatures are based on the values measured by Lomonaco et al. (2016).

Bauer et al. (2012) only had density values for the solid phase, and thus another reference had to be found for the liquid density of the PCM. Liquid and solid densities for this study were based on the values listed in the review article by Liu et al. (2012). For the numerical simulations it was decided that the most accurate results would be obtained by applying the Boussinesq approximation to the density – given the importance of natural convection in phase change heat transfer, as will be discussed in more detail in the next chapter. Care has to be taken when choosing to apply the Boussinesq approximation, as it is inaccurate when the density differences are large, specifically when $\frac{\Delta\rho}{\rho}$ is of order unity. The temperature range, affecting the Boussinesq density, thus has to be kept small for the approximation to be valid.

Finally, the dynamic viscosity values for this study is calculated at each temperature using the polynomial expression used by (Koller et al., 2016):

$$\mu(T) = 0.0251 - 6.054T \times 10^{-5} + 3.871T^2 \times 10^{-8} \rightarrow T \text{ in Kelvin} \tag{11}$$

All of the relevant thermophysical properties of the selected materials are listed in Table 5.

Table 5 Thermophysical properties of PCM and fin material.

Property	Symbol	Unit	$NaNO_3$	Aluminium	Reference
Melting temperature	T_{m}	°C	306	-	(Bauer et al., 2012)
Liquidus temperature	T_{l}	°C	307	-	(Lomonaco et al., 2016)
Solidus temperature	T_{s}	°C	305*	-	(Lomonaco et al., 2016)
Latent heat of fusion	H_{f}	kJ/kg	178	-	(Bauer et al., 2012)
Density	ρ	kg/m^3	2260 (s) 1905 (l)	2719	(Liu et al., 2012), (ANSYS, 2018)
Thermal conductivity	k	W/m.K	0.82 (s)** 0.514 (l)	202.4	(Bauer et al., 2012), (ANSYS, 2018)
Specific heat	C_{p}	kJ/kg.K	1.325 (s)*** 1.658 (l)	871	(Koller et al., 2016), (ANSYS, 2018)
Dynamic viscosity	μ	kg/m.s	0.003****	-	(Koller et al., 2016)
Volumetric expansion	β	K^{-1}	4×10^{-5}	-	(Bauer et al., 2012)

* Average value taken from $\boldsymbol{T_s}$ value measured with two different tecniques.
** Average value taken from $\boldsymbol{k}$-values at three different temperatures.
*** Average $\boldsymbol{C_p}$ value taken from six temperatures.
**** Dynamic viscosity at the melting temperature based on equation (11).

3.3 Chapter summary

The TES device containing PCM was selected. A PCM container with HTF tubes arranged in a staggered layout and with horizontal plate fins at regular intervals was defined. A characteristic region was defined around the HTF, which was further simplified to a cylindrical volume. The device was simplified to two dimensions by first taking a cross section in the vertical plane through the middle of the cylinder and then leveraging the geometry's vertical symmetry and repeating PCM and fin pattern to define a single PCM and fin unit with width L, fin pitch spacing P and fin thickness t_{f}. Aluminium was selected for the fin material and $NaNO_3$ was chosen was the PCM. Relevant thermophysical material properties were presented for both,

In the next chapter the numerical domain is officially defined, along with the relevant boundary conditions and method which will be used to model the solidification process of the PCM.

4. Numerical Method

This chapter present information on the selected numerical simulation platform, the numerical domain, the boundary conditions, the transient state governing equations, and the mesh. Initial mesh independence and validation is also done.

4.1 Simulation platform

ANSYS Fluent 18.1 was selected as the platform on which to model the phase change process within the PCM. It is particularly suitable because it solves the moving boundary problem by using a fixed grid enthalpy-porosity method by modelling the mushy-zone as a pseudo-porous medium with a porosity equal to the liquid fraction of the PCM and ranging from 1 to 0 as the material solidifies (Voller and Prakash, 1987). As indicated later, sinks are added to the momentum equations to account for the pressure drop caused by the presence of the material in the solid phase.

There are a number of different methods to solve for solidification and melting numerically. The methods considered for this study are discussed in section 2.6.3 of the literature review. These include fixed grid methods, variable grid methods and methods of latent-heat evolution – such as the apparent capacity method, effective heat capacity method, heat integration method, source-based method and the enthalpy method. The enthalpy method is the one that was finally chosen.

4.2 Domain

The single PCM and fin unit shown in Figure 15 was used to define the rectangular numerical domain, which is represented in Figure 16 on an $x - y$ plane. The domain has the same dimensional definition mentioned earlier: L, P and t_f. The effects of gravity (g = 9.81 m/s) was considered in the negative y direction.

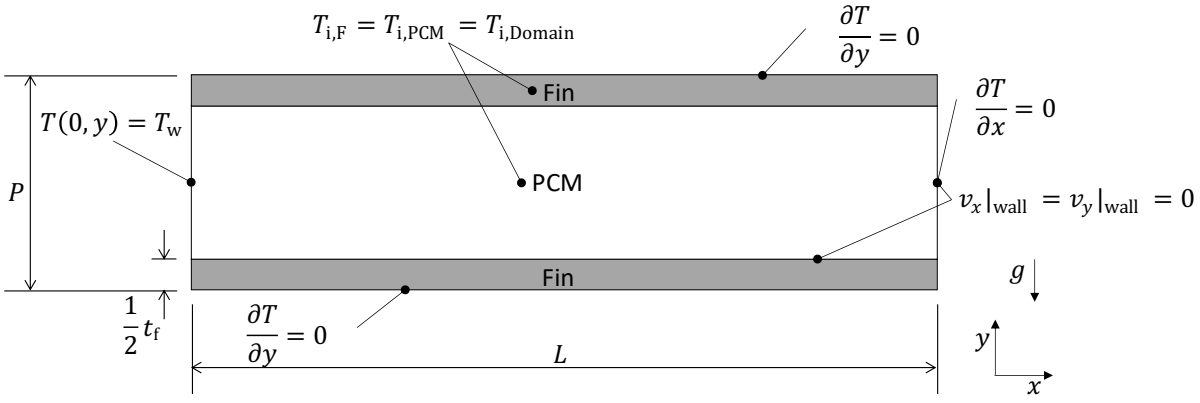

Figure 16 Numerical domain with dimensions and boundary conditions.

Heat is extracted from the PCM by the HTF passing on the left hand side of the PCM. Because the fluid behaviour is not the focus of this study the presence of the colder heat transfer fluid is represented as uniform wall temperature only. As such, the domain only contains the fins and the PCM.

4.3 Boundary and initial conditions

The boundary and initial conditions applied to the domain are also shown in equation format in Figure 16. A symmetry condition was applied to the top and bottom of the compartment (in die middle of the fin) to reduce the computational processing power and time necessary to solve the system.

Looking at numerical studies that applied a temperature gradient to the heat transfer wall instead of a constant wall temperature, such as (Pointner et al., 2016), it was found that the effect of the temperature gradient is negligible. Therefore, because of this and the reasons supplied previously indicating a very small temperature gradient, a constant wall temperature (T_{w}) was applied which is ΔT lower than the PCM melting temperature. An adiabatic boundary conditions was applied to the outside wall of the enclosure. A no-slip condition was applied to all the walls. The entire domain will be initialised at a uniform temperature.

4.4 Governing equations

This section covers the governing equations that were used. This includes the general Navier-Stokes equation that takes into consideration the mass, momentum and energy conservations, as well as equations specific to solidification and melting process, and the buoyancy driven flow incorporation.

4.4.1 Navier-Stokes equations

The Navier-Stokes equations are very well known and the basis for solving most heat and mass transfer problems. ANSYS Fluent defines the general continuity, momentum and energy equations used in most of their physical models as are shown in equations (12), (13) and (15).

Continuity:

$$\frac{\partial \rho}{\partial t} + \nabla \cdot (\rho \vec{v}) = S_{\mathrm{m}} \tag{12}$$

Here S_m is a source term for the mass that could be added or removed during a transient simulation (e.g. vaporisation of liquid droplets).

Momentum equation:

$$\frac{\partial}{\partial t}(\rho \vec{v}) + \nabla \cdot (\rho \vec{v} \vec{v}) = -\nabla p + \nabla \cdot (\bar{\bar{\tau}}) + \rho \vec{g} + \vec{F} \tag{13}$$

Here p is the static pressure, $\rho \vec{g}$ and $\vec{F}$ are the gravitational and external body forces and $\bar{\bar{\tau}}$ is the stress tensor, which is given by:

$$\bar{\bar{\tau}} = \mu[(\nabla \vec{v} + \nabla \vec{v}^T) - \frac{2}{3} \nabla \cdot \vec{v} I] \tag{14}$$

where μ is the dynamic viscosity and I is the unit tensor. In equation (13), $\vec{F}$ also contains other model-dependent source terms such as porous-media – which is applicable to this study.

Energy equation:

$$\frac{\partial}{\partial t}(\rho E) + \nabla \cdot \left(\vec{v}(\rho E + p)\right) = \nabla \cdot k\nabla T + S_{\mathrm{h}} \tag{15}$$

Here S_h includes any volumetric heat sources and E is given by:

$$E = h - \frac{p}{\rho} + \frac{v^2}{2} \tag{16}$$

Where h is the sensible enthalpy.

4.4.2 Solidification and melting

Modelling phase change in Fluent requires a slight change in the general Navier-Stokes equations to allow for the implementation of the enthalpy-porosity technique used to model the solidification and melting process. The methodology followed by Voller and Prakash (1987) in developing the enthalpy-porosity technique, specifically for the case of solidification, is detailed below.

The enthalpy of the material is computed as the sum of the sensible enthalpy, h, and the latent heat ΔH:

$$H = h + \Delta H \tag{17}$$

where the sensible enthalpy (h) is defined as:

$$h = C_{\mathrm{p}} T \tag{18}$$

which can also be expressed as an integral:

$$h = h_{\mathrm{ref}} + \int_{T_{\mathrm{ref}}}^{T} C_{\mathrm{p}} dT \tag{19}$$

Establishing a mushy phase change, the contribution of the latent heat of fusion has to be associated with the solid fraction in the mushy zone and specified as a function of temperature:

$$\Delta H = \begin{cases} 0, & T < T_{\mathrm{s}} \\ H_{\mathrm{f}}(1-\psi), & T_{\mathrm{s}} \le T < T_{\mathrm{l}} \\ H_{\mathrm{f}}, & T \ge T_{l} \end{cases} \tag{20}$$

where H_{f} is the latent heat of fusion, ψ is the local solid fraction defined as a volume fraction occupied by the solid phase as is given in equation (21) below, T_{l} is the liquidus temperature (the temperature at which the PCM starts to solidify) and T_{s} is the solidus temperature (the temperature at which the PCM is fully solid).

$$\psi = 1 - \phi \tag{21}$$

Here ϕ is the melt (or liquid) fraction of the PCM. A simple linear form for the local solid fraction is given as:

$$\psi(T) = \begin{cases} 1, & T < -\varepsilon \\ \dfrac{\varepsilon - T}{2\varepsilon}, & -\varepsilon \leq T < \varepsilon \\ 0, & T \geq \varepsilon \end{cases} \tag{22}$$

where the temperature has been scaled such that $T = \varepsilon$ and $T = -\varepsilon$ represent the T_l and T_s respectively. In this equation ε is the half temperature range of the mushy zone, i.e. $\varepsilon = (T_\mathrm{s} - T_\mathrm{l})/2$.

It is helpful to regard the entire cavity as a porous medium, where the porosity, defined as the liquid fraction of the PCM in this context and can be represented by λ. $\lambda = 1$ in the liquid phase, $\lambda = 0$ in the solid phase and $0 < \lambda < 1$ in the mushy zone. The governing equations can then be written in terms of the superficial velocity ($\vec{v}$) defined as:

$$\vec{v} = \lambda \overrightarrow{v_\mathrm{l}} \tag{23}$$

where $\overrightarrow{v_\mathrm{l}}$ is the actual fluid velocity. On recognizing that the porosity $\lambda = 1 - \psi$, the above relationship can be expanded to give:

$$\vec{v} = \begin{cases} 0, & \text{in the solid phase} \\ (1-\psi)\overrightarrow{v_\mathrm{l}}, & \text{in the mushy zone} \\ \overrightarrow{v_\mathrm{l}}, & \text{in the liquid phase} \end{cases} \tag{24}$$

The governing equations for solidification can thus be redefined as follows:

Continuity:

The modelling of solidification and melting does not require the source term S_m in equation (12) when the Boussinesq approximation is applied. The Boussinesq approximation treats the density in the system as a constant value, except for the buoyancy term in the momentum equation, and thus no mass is added to the system. ANSYS Fluent defines the Boussinesq approximation as:

$$\rho = \rho_\mathrm{s}(1 - \beta \Delta T) \tag{25}$$

where ρ_s is the solid density, β the volumetric expansion coefficient and ΔT the difference between the current temperature (at which the density is calculated) and the reference temperature of the PCM.

The right-hand side of equation (12) becomes zero and simplifies to:

$$\frac{\partial v_x}{\partial x} + \frac{\partial v_y}{\partial y} = 0 \tag{26}$$

where v_x and v_y are the liquid velocities in the x and y directions.

Momentum:

$$\frac{\partial(\rho v_x)}{\partial t} + \nabla \cdot (\rho \vec{v} v_x) = \nabla \cdot (\mu \nabla v_x) - \frac{\partial p}{\partial x} + S_x \tag{27}$$

$$\frac{\partial(\rho v_y)}{\partial t} + \nabla \cdot (\rho \vec{v} v_y) = \nabla \cdot (\mu \nabla v_y) - \frac{\partial p}{\partial y} + S_y + S_{\mathrm{b}} \tag{28}$$

Where:

$$S_x = -A v_x \tag{29}$$
$$S_y = -A v_y \tag{30}$$

Here A is a function that increases from zero to a large number as ψ increases from its liquid value of 0 to its solid value of 1 and is given by:

$$A = -A_{\mathrm{mush}} \frac{(1-\lambda)^2}{\lambda^3 + \varepsilon} \tag{31}$$

Where A_{mush} is the constant mushy zone parameter of which the default value of $A_{\mathrm{mush}} = 10^4$ provided by ANSYS was used in this study.

S_{b} is the buoyancy term:

$$S_{\mathrm{b}} = \frac{\rho g \beta (h - h_{\mathrm{ref}})}{C_{\mathrm{p,l}}} \tag{32}$$

where β is a thermal expansion coefficient and h_{ref} is a reference value of the sensible heat.

Alternatively, the momentum sink terms (S_x and S_y) can be changed to take into account the pull velocities due to the PCM's shrinkage and pulling away from the wall. In this study, the pull velocities were assumed to be 0, since the change in relative volume of the PCM during solidification was not taken into account.

Energy:

$$\frac{\partial \rho h}{\partial t} + \nabla \cdot (\rho \vec{v} h) = \nabla \cdot (\alpha \nabla h) - S_{\mathrm{h}} = 0 \tag{33}$$

The form of the enthalpy source term S_h is derived from the enthalpy formulation of convection-diffusion phase change:

$$\frac{\partial \rho H}{\partial t} + \nabla \cdot (H \rho \vec{v}) - \nabla \cdot (k \nabla T) = 0 \tag{34}$$

This equation can be expanded on substitution of $H = C_{\mathrm{p}} T + \Delta T$, which results in:

$$S_{\mathrm{h}} = \frac{\partial \rho \Delta H}{\partial t} + \nabla \cdot (\rho \vec{v} \Delta H) \tag{35}$$

4.5 Mesh

In order to solve the governing equations numerically, the domain must first be divided by a numerical mesh in order for variables at each element (cell, node, vertex or face) to be solved individually and thus cumulatively forming a solution. Different geometries and applications required different types of numerical meshes. The resolution of the mesh grid can also vary throughout the domain depending on which area is of interest, e.g. a heat transfer wall, phase change front, convection currents, etc.

4.5.1 Mesh theory

The elements of a mesh are connected to form a grid, of which the main types are structured and unstructured grids, or a combination of the two. In two-dimensional geometries, structured and unstructured grids make use of one of two basic cell shapes – triangles (or tri), which are mostly used in unstructured grids, and quadrilaterals (or quads), which are mostly used in structured grids.

Structured grids:
Structured grids are identified by the regular connectivity of its nodes and follows a uniform pattern to which i and j (and k in three-dimensions) indexing can be applied. This means the neighbourhood relationships of the nodes are defined by the storage arrangement which results in a highly space-efficient (in terms of hard drive storage) grid. The simplicity of the grid also generally produces convergence in numerical simulations and requires less processing power.

A downside to structured grids is that their applicability is limited in terms of the range of geometries for which it is suitable. Very complicated geometries are difficult to mesh using a structured grid. It is, however, very suitable to simple geometries.

Unstructured grids:
The nodes in an unstructured grid are arranged in an arbitrary way and do not follow a uniform pattern. It requires more attention and finer design to ensure it results in good convergence in numerical simulations. The unconstrained arrangement of an unstructured grid allows for it to be applied to more complex geometries than a structured grid.

Mesh refinement:
Once a suitable grid is chosen, care has to be taken to decide on which areas of grid to refine (increase the resolution) and which areas to coarsen. Areas of high interest in phase change problems are mostly those around the phase change front (and the interface between the PCM and the container or fins it is in contact with) where there will be higher temperature and fluid velocity gradients.

4.5.2 Meshing type

When considering mesh quality metrics like skewness, smoothness and aspect ratios, it becomes apparent that a structured grid is the mesh most suited for the domain of this numerical study.

A structured quad grid on a rectangular geometry results in a very good quality mesh, with a skewness possible close to 0 and smoothness and aspect ratio close to 1, if mesh

refinement is done correctly. Figure 17 shows the basic mesh type that was used. The grid size used here is only for demonstration purposes and was refined to improve the accuracy of the modelling results as is described in a later section.

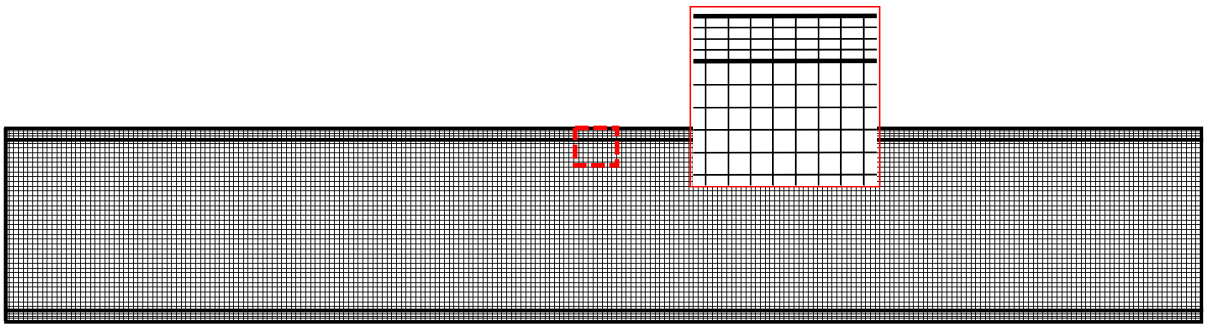

Figure 17 Basic mesh type used in this study

This basic mesh would likely produce good results since it scores perfectly on all the mesh metrics – a skewness of 0 and smoothness and aspect ratio of 1. The resolution of the mesh is, however, not fine enough to capture all the necessary information throughout the domain and mesh refinement was thus considered.

Refinement:

There are a number of different ways in which the mesh can be refined, including adaptive mesh refinement (AMR). In this study, this method works well in capturing the temperature gradient at the boundaries between the PCM and the fins; trying to refine the mesh around the phase change front to capture the desired information, however, poses a problem. Because the phase change front moves during phase transition, the region where the mesh needs to be refined, also moves as the PCM melts or solidifies.

Two different ways of overcoming this obstacle was investigated: maintaining the uniform layout of the mesh and refining it to a resolution fine enough to capture the desired information, or employing a method called dynamic adaptive mesh refinement. Dynamic AMR works on the same principle as normal AMR – the refinement is focused on regions of high interest in the domain – but is usually applied to time dependent simulations.

In time dependent simulations, the solution changes as time progresses and the regions of high interest could also move in the domain (i.e. a moving phase change front), which means the mesh refinement cannot be static. The solution is thus evaluated at intervals to determine which areas of the mesh need to be refined and which can be coarsened. The solver then automatically adapts the mesh as the solution changes.

A test was done on an arbitrary domain, solving for solid-liquid phase change, to determine how effective dynamic AMR is at creating a well-refined mesh that could capture the desired information around the moving phase change front. Melting in a rectangular PCM enclosure was simulated with a hot wall (on the left-hand side), a cold wall (on the right-hand side) and the top and bottom walls adiabatic. A uniform structured quad mesh was applied initially, after which the solver's dynamic AMR was set to refine the mesh around the phase change front only. The mesh refinement superimposed onto a contour plot of the PCM's phase of matter (with blue representing solid, red liquid and anything in between falling in the mushy zone) is shown in Figure 18 at 0 s, 40 s, 80 s and 115 s into the simulation.

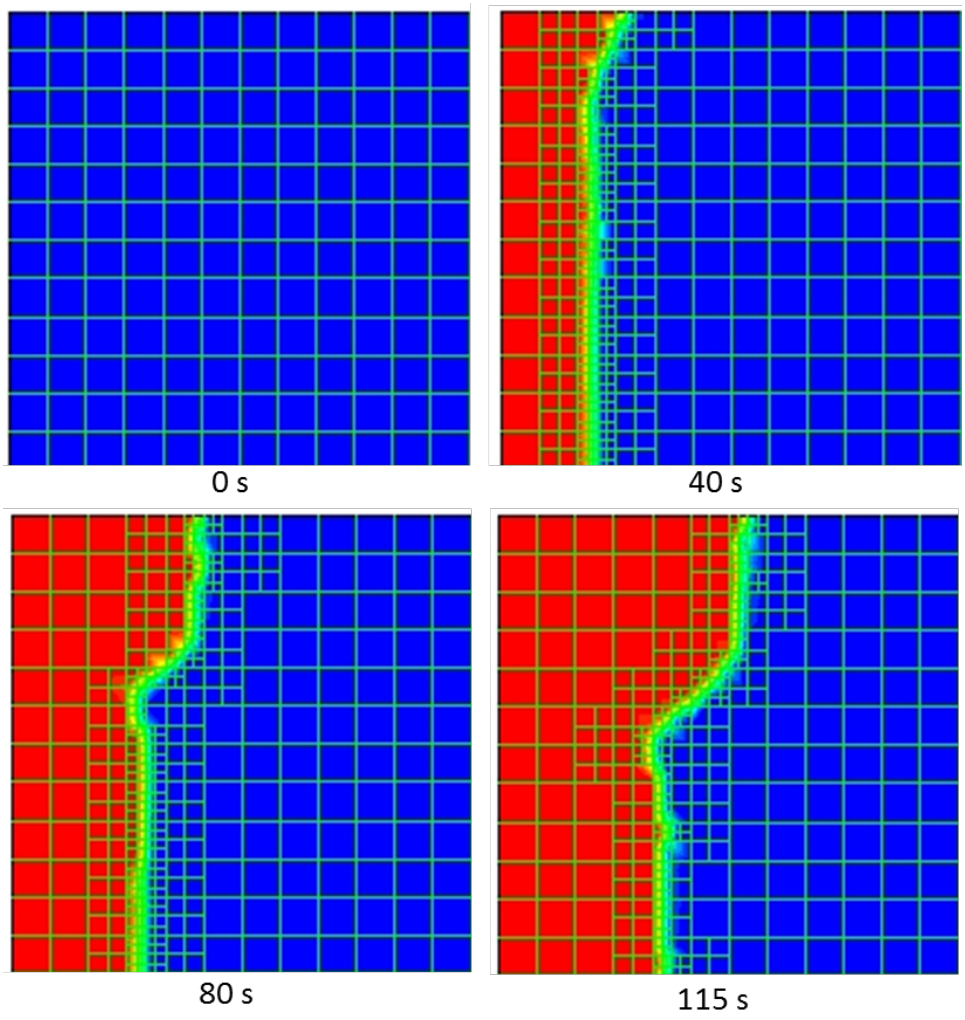

Figure 18 Dynamic mesh refinement.

It can be seen that the mesh can be refined to capture all the parameter of interests around the phase change front (which could include natural convection and latent heat transfer), while keeping the rest of the mesh grid size large to reduce the processing power and time required for the simulation.

This method can have advantages in terms of accuracy of results or reducing the amount of processing power required to solve a problem. It does, however, have a big drawback: when conducting a numerical research study, it is essential to conduct a mesh independence study to minimise numerical error and any effect the mesh might have on the result of the simulation. This requires the exact size of the mesh to be constant and known for each iteration of the independence study, which is not possible with a dynamically adaptive mesh.

The alternative to dynamic AMR is maintaining the uniform mesh and just refining the mesh of the entire domain. This method does create a fine mesh in regions where it is not necessary at all times, which requires more processing power and time, but it also allows for a reliable mesh independence study to be conducted. Additionally, having a high-quality mesh throughout the domain allows for accurate results regardless of where the phase change front is.

4.6 Determining the mesh and time step size

Errors and uncertainty are unavoidable aspects of numerical modelling and it is necessary to quantify the level of confidence in the results. In this section the discretisation error is quantified by performing systematic refinement of the mesh and time step (t_s) sizes and thereby reaching an independent solution for both. The derived mesh and time step size pair from this section was applied to the rest of the simulations in this study.

Because the purpose of this investigation was to determine the optimized fin spacing, it was inevitable that the phase change processes for several domain aspect ratios had to be modelled. It would have been too computationally expensive to do a full mesh and time step refinement for each optimisation geometrical case. As such, a comparable sized domain was used to determine the appropriate mesh and time step setting. It could be argued that the obtained mesh and time step size via this approach might not be applicable to all the geometric cases considered in this study. However, as it will be shown in the next chapter, the obtained mesh and time step size was indeed suitable to reproduce independent experimental data from literature for a different domain aspect than the one used in this section.

Figure 19 shows the domain used to determine the acceptable mesh and time step size settings. It is a simple rectangular domain, similar to the one defined previously. For the intended purpose, the enclosure has a width (L) of 10 mm, a pitch (P) of 14 mm and a fin thickness (t_f) of 4 mm (or half fin thickness of $\frac{1}{2}t_f = 2\ mm$ as shown in Figure 19).

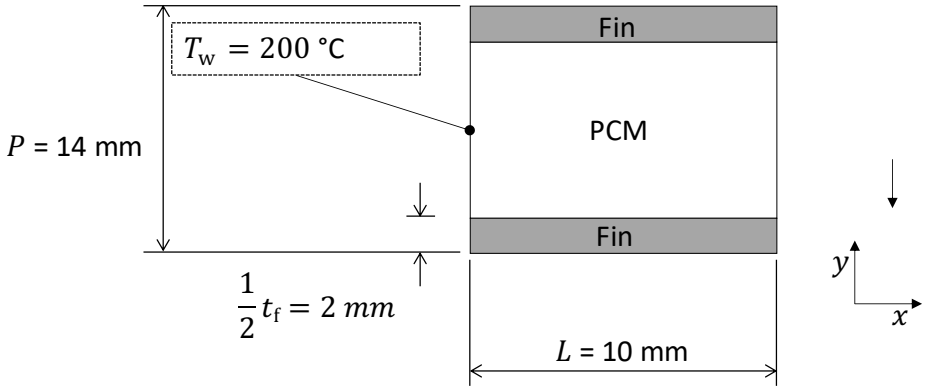

Figure 19 Independence study domain dimensions.

An isothermal wall temperature that was $\Delta T = 20$ K colder than the melting temperature was selected and the entire domain was initiated as a uniform temperature which was 1 K warmer than then melting temperature to ensure an initial liquid state within the PCM.

The convergence criteria were set to be 1×10^{-5} for the continuity, momentum and the energy equations. A maximum of 30 iterations were set per time step. All the cases were considered completed when the overall solid fraction (ψ) in the PCM reached a value of 1, indicating complete solidification.

4.6.1 Mesh independence

A uniform structured quad mesh (as discussed in earlier) was used for the mesh independence study. Six different mesh sizes were investigated to establish the number of elements required to reach a mesh independent result. A breakdown of the number of elements are given in Table 6 for cases M1 to M6 with the number of elements in the x and y direction listed as well as the their respective sizes: dx in the x direction which were the same for both the PCM and the fin, dy_{PCM} in the y direction for the PCM region, and dy_{f} in the y direction for the fin regions.

Table 6 Mesh independence cases.

Case	x divisions	dx [mm]	PCM y divisions	dy_{PCM} [mm]	Fin y divisions	dy_{f} [mm]	Total elements
M1	55	0.18	55	0.18	11	0.91	4235
M2	75	0.13	75	0.13	20	0.50	8625
M3	114	0.09	114	0.09	20	0.50	17 556
M4	170	0.06	170	0.06	20	0.50	35 700
M5	250	0.04	250	0.04	20	0.50	72 500
M6	365	0.03	365	0.03	20	0.50	147 825

The aim was to have elements with an aspect ratio of 1 in the PCM part of the domain, thus the number of elements in the x and the PCM y direction was kept the same. Having a high quality mesh in the PCM was more important because of, amongst other reasons, the influence of buoyancy driven flow in the liquid PCM. The number of elements in the fins in the y direction was thus kept constant in most of the cases except for the coarsest mesh where it was reduced to scale with the fewer cells in the PCM.

All the cases were run with a time step of t_{s} = 5 × 10^{-4} s. The heat flux (q) through the heat transfer wall and the solid fraction (ψ) for each of the mesh cases are shown in Figure 20 and Figure 21 respectively.

Cases M1, M2 and M3 seem to be equally spaced followed by a larger gap between M3 and M4, then M4 and M5 close to each other followed by another gap between M5 and M6.

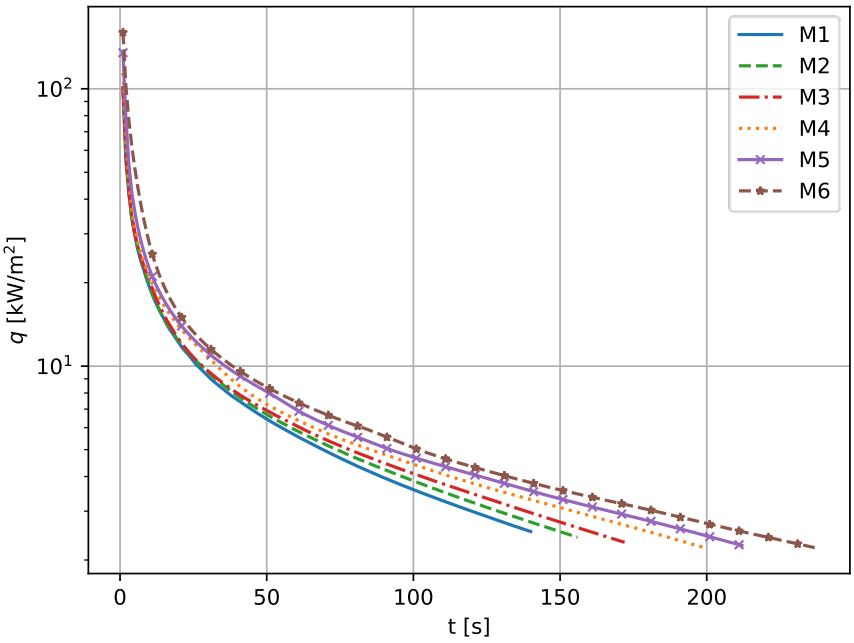

Figure 20 Mesh independence heat transfer wall heat flux vs time.

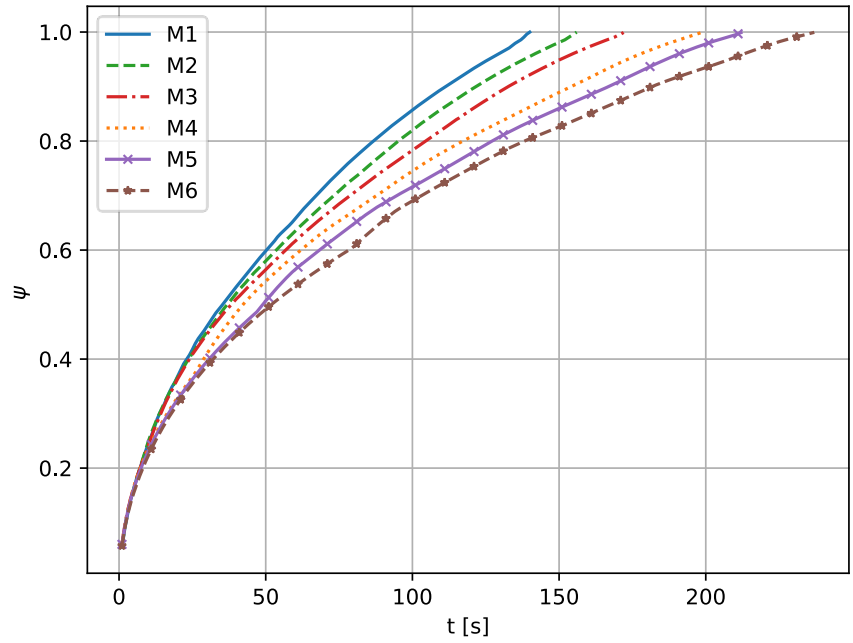

Figure 21 Mesh independence solid fraction vs time.

In order to determine for which mesh size an independent solution is reached, two approaches were taken (based on the solid fraction). Firstly, the error between consecutive mesh sizes was calculated for each time step and the average was calculated over time. Secondly, the grid convergence indicator (GCI) was calculated for each consecutive mesh size, according to Versteeg and Malalasekera (2006). Both these metrics were calculated as a function of time due to the transient nature of the solidification process.

Error fraction:

The error for the solid fraction between consecutive mesh sizes, $\varepsilon_{\mathrm{mesh},\psi}$, is calculated as:

$$\varepsilon_{\mathrm{mesh},\psi} = \frac{\mathrm{Mesh_{i+1}} - \mathrm{Mesh_i}}{\mathrm{Mesh_{i+1}}} \tag{36}$$

$\varepsilon_{\mathrm{mesh},\psi}$ for all the mesh sizes is plotted across the simulation time in Figure 22 and the average errors are listed in Table 7. In the first 50 s of the simulation the errors seem to fluctuate significantly (due to the steep initial gradient in the ψ vs time curve), which has an influence on the average error values. The averages were thus calculated over the full simulation time and also over only the time steps after 50 s.

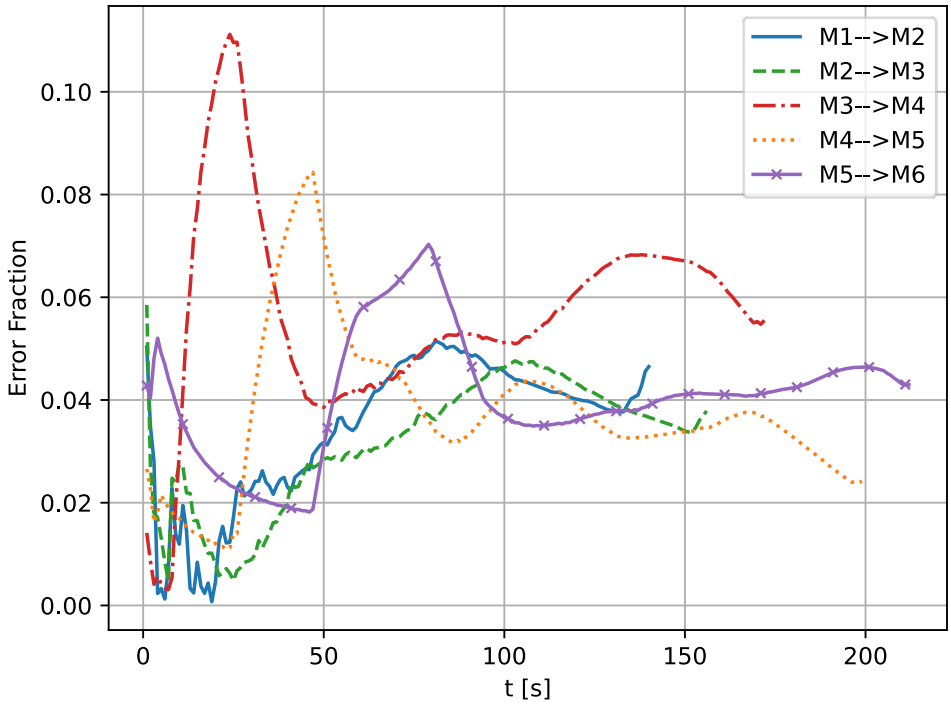

Figure 22 Error for ψ of all mesh cases vs time.

The average errors have similar values at smaller and larger mesh values for both the full simulation and t > 50 s with the largest error between at M3 to M4. For t > 50 s the average comparative errors were lower at larger mesh sizes (M4 to M5) than for smaller ones.

Table 7 Mesh independence errors.

Cases	Average Error (Full)	Average Error (t > 50 s)
M1 --> M2	0.025	0.034
M2 --> M3	0.023	0.031
M3 --> M4	0.038	0.044
M4 --> M5	0.025	0.028
M6 --> M7	0.028	0.034

When considering the full simulation, the smallest average error is 0.023 between cases M2 and M3 closely followed an error of 0.025 between cases M1 and M2 and between M4 and M5. However, when only considering the time steps after 50 s (after the initial fluctuations) the smallest average error is 0.028 between case M4 and M5 followed by an error of 0.031 between cases M2 and M3.

The smaller mesh sizes thus seem to show a better independence when considering the full simulation with the larger mesh sizes showing better independence after the initial fluctuations in error values.

Grid Convergence Indicator:

The GCI for each consecutive mesh size is calculated as:

$$\mathrm{GCI}_{12} = \frac{F_s \left| \frac{f_2 - f_1}{f_1} \right|}{r^p - 1} \tag{37}$$

Where F_s is a safety factor (with a value of 1.25), f_1 and f_2 are the solution values for two consecutive mesh cases (e.g. the ψ value for cases M1 and M2 or M2 and M3), r is the ratio between mesh sizes (approximately 2.03 for all cases) and p is the observed order of truncation error decay, calculated across three successive meshes as:

$$p = \ln\left(\frac{f_3 - f_2}{f_2 - f_1}\right) / \ln(r) \tag{38}$$

The GCI of another set of consecutive cases then has to be calculated and independence is reached when the GCI ratio is approximately 1:

$$\frac{\mathrm{GCI}_{23}}{r^p \mathrm{GCI}_{12}} \approx 1 \tag{39}$$

The GCI was calculated for each consecutive pairing of meshes in order to determine whether independence has been reached according to equation (39). This was done at each time step in the simulation, limited to the maximum time step of the shortest case (140 s). The results are shown in Figure 23 along with a line indicating a GCI ratio of 1.

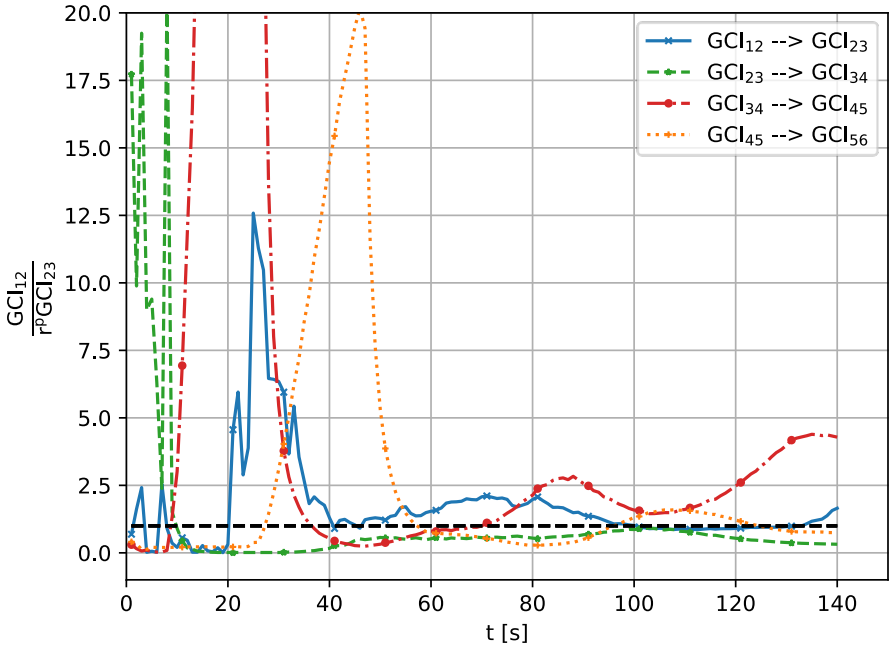

Figure 23 GCI independence vs full simulation time.

The values can again be seen to fluctuate significantly in the first 50 s for all the cases. The results for t = 51 s to t = 140 s, plotted in Figure 24, show that none of the cases have a consistent value close to 1.

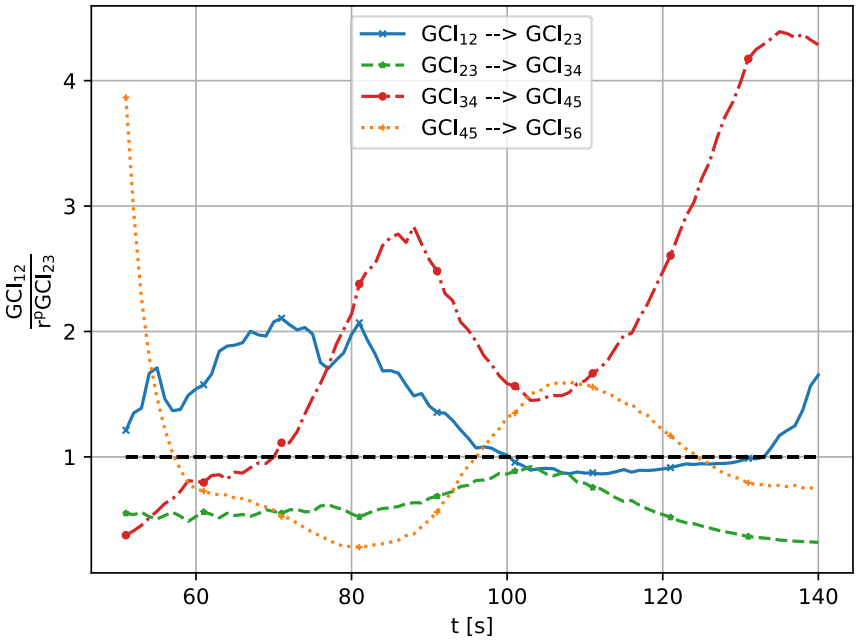

Figure 24 GCI independence vs t > 50s.

GCI_{12} --> GCI_{23} is the most consistent after its initial fluctuations, while GCI_{23} --> GCI_{34} is also fairly consistent, but consistently below 1. The GCI for mesh cases M4 to M6 (GCI_{45} --> GCI_{56}) seem to be the one that fluctuates consistently around the 1 value.

The averages and standard deviations (σ) for each of the cases are listed in Table 8. The values confirm what was observed in Figure 23 and Figure 24. The smaller meshes (M1 to M3 and M2 to M4) seem to show a better independence when considering the simulation time from 0 s, but the values are skewed by the large fluctuations before 50 s. When only considering the values from 51 s onwards, the larger meshes (M4 to M6) have a value of 0.97 which indicates mesh independence within a tolerance of 3%.

Table 8 GCI independence average and standard deviation across time.

GCI	Average	σ	Average (t >50s)	σ (t >50s)
GCI_{12} --> GCI_{23}	1.7419	1.8875	1.3399	0.4146
GCI_{23} --> GCI_{34}	1.1166	3.0443	0.5925	0.1581
GCI_{34} --> GCI_{45}	7.6773	18.1372	2.0894	1.1384
GCI_{45} --> GCI_{56}	2.4587	4.4779	0.9705	0.5772

When taking both the error fraction and GCI results into consideration, it was found that using case M5 (a mesh size of 0.04×0.04 mm with a dy_f of 0.5 mm) will result in the best mesh independent solution for purposes of this study.

4.6.2 Time step independence

The resultant mesh from the mesh independent study (case M5 with a 0.04×0.04 mm grid size) was used as the mesh for the time step independence study. Eight different time step sizes were investigated to establish the maximum time step size required to reach a time step independent result. A breakdown of the different cases (TS1 to TS8) and their time steps are given in Table 9.

Table 9 Time step independence cases.

Case	Time step [s]	Mesh Size
TS1	0.01	Mesh case M5 (0.04×0.04 mm)
TS2	5×10^{-3}	
TS3	2.5×10^{-3}	
TS4	1×10^{-3}	
TS5	5×10^{-4}	
TS6	2.5×10^{-4}	
TS7	1×10^{-4}	
TS8	5×10^{-5}	

The heat flux (q) through the heat transfer wall and the solid fraction (ψ) for each case, are shown in Figure 25 and Figure 26 respectively.

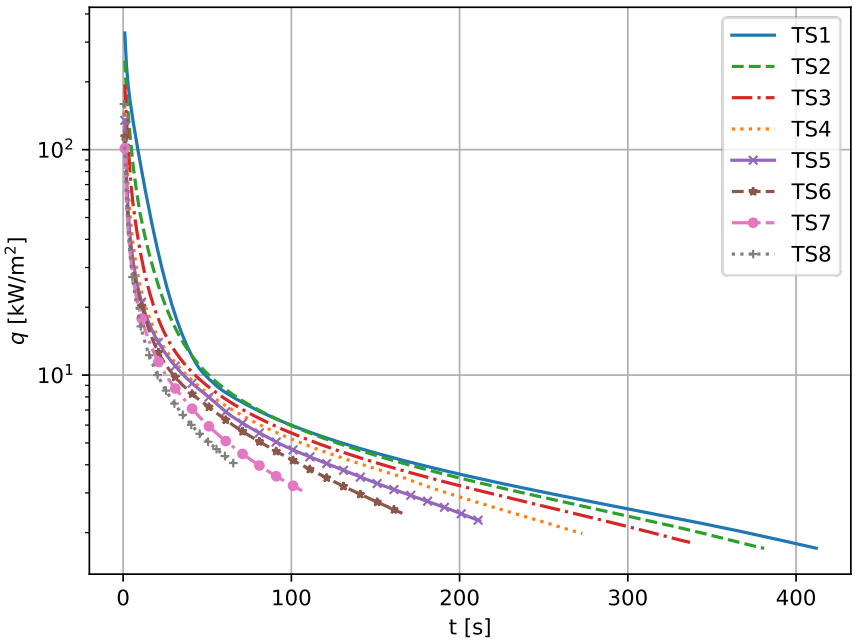

Figure 25 Time step independence heat transfer wall heat flux vs time.

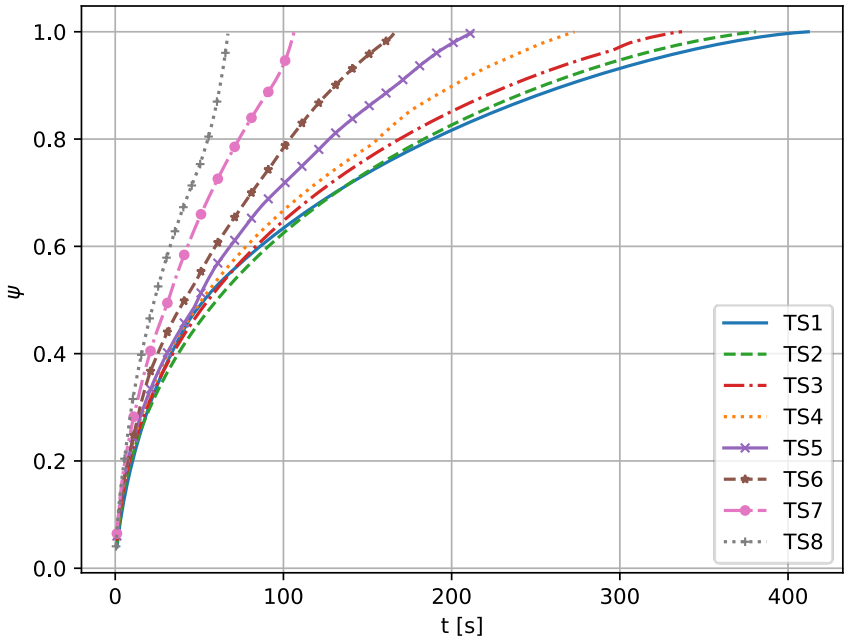

Figure 26 Time step independence solid fraction vs time.

The time step cases do not seem to converge to a solution as the time step gets more refined. The two largest time steps tested (0.01 s and 0.005 s) are the only two cases which seem to converge towards a similar solution, thereafter the difference between cases seem to grow steadily. The solid fraction results were used to calculate the error between consecutive time step sizes to determine what the average error fraction is over the simulation time. This was the only method used to determine time step independence.

The error for the solid fraction between consecutive mesh sizes, $\varepsilon_{t_s,\psi}$, was calculated as:

$$\varepsilon_{t_s,\psi} = \frac{t_{s_{i+1}} - t_{s_i}}{t_{s_{i+1}}} \tag{40}$$

$\varepsilon_{t_s,\psi}$ for all the time step sizes is plotted across the simulation time in Figure 27 and the average errors are listed in Table 10.

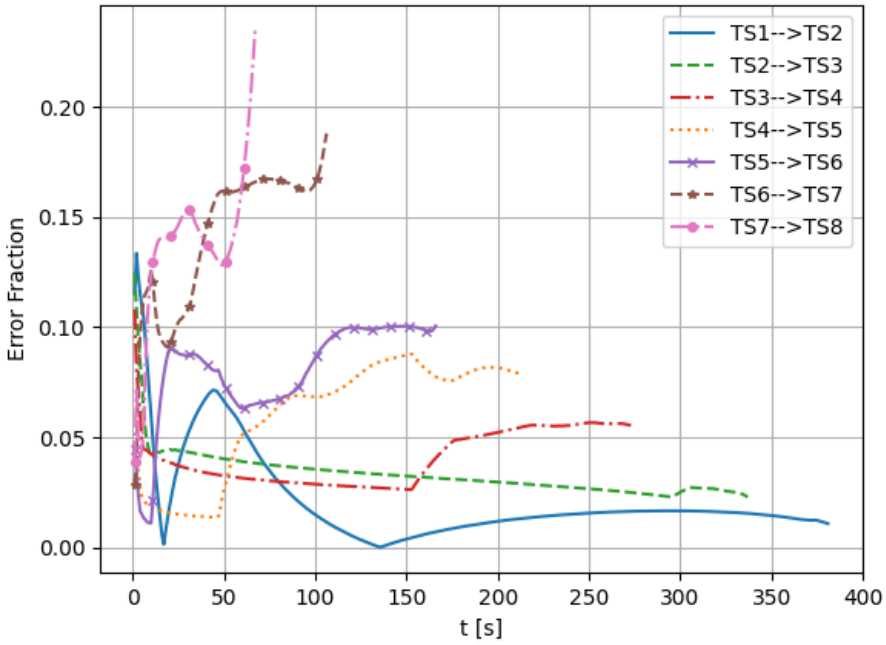

Figure 27 Error for ψ of all time step cases vs time.

The errors between cases were very small when considering the larger time steps, especially from 0.01 s to 0.005 s, but increased rapidly as the time steps became larger. The errors between TS4 and T6 were still quite small, with the maximum error peaking at 10% between TS5 and TS6, and the averages all below 6% for the full simulation time. When only considering the simulation time after t > 50 s it reveals that only the first set of time steps (TS1 to TS2) have a lower average than for the full simulation. The errors from TS1 to TS6 do seem to reach a stable value eventually while the error from TS6 to TS8 seem to keep increasing.

Table 10 Time step independence errors.

Cases	Time steps	Average Error (Full)	Average Error (t > 50 s)
TS1 --> TS2	$0.01 \rightarrow 5\times10^{-3}$	0.0127	0.0121
TS2 --> TS3	$5\times10^{-3} \rightarrow 2.5\times10^{-3}$	0.0285	0.0312
TS3 --> TS4	$2.5\times10^{-3} \rightarrow 1\times10^{-3}$	0.0254	0.0283
TS4 --> TS5	$1\times10^{-3} \rightarrow 5\times10^{-4}$	0.0467	0.0594
TS5 --> TS6	$5\times10^{-4} \rightarrow 2.5\times10^{-4}$	0.0580	0.0709
TS6 --> TS7	$2.5\times10^{-4} \rightarrow 1\times10^{-4}$	0.0979	0.1375
TS7 --> TS8	$1\times10^{-4} \rightarrow 5\times10^{-5}$	0.0870	0.1463

The $\varepsilon_{t_s,\psi}$ results for all the time step sizes show that the error only increased as the time steps decreased, especially between TS6 and TS7 onwards. It was thus decided to choose a time step that still falls within the range where the errors settle on a stable value. The largest time step (0.01 s) was selected as the time step to produce to most independent results as the smaller time steps resulted in increasing errors.

4.6.3 Final mesh and time step size

The numerical mesh selected for this study is a uniform structured quad mesh refined to a resolution that produces mesh independent and accurate results. After the mesh independence study was completed it was decided to use a mesh with a cell size of 0.04×0.04 mm in die PCM. The number of cells in the fin was fixed to be 4 in the vertical direction and 250 in the horizontal (which equates to a cell width of 0.2 mm).

The quality of the selected mesh is defined by the mesh metrics below:

- **Skewness:** since it is a structured quad mesh the skewness value is 0.
- **Smoothness:** all the cells in the PCM are the same size and all the cells in the fins are the same size; the only region that is not ideal is the transition between the fins' cells and the PCM's cells, which is negligible.
- **Aspect ratio:** The aspect ratio of the cells in the PCM is 1 while those in the fins vary from 2 ($P = 8$ mm) to 3.56 ($P = 2$ mm). This is not ideal, but the most important cells are those in the PCM and a less than perfect aspect ratio in the fins is thus acceptable.

The largest time step – of $t_s = 0.01$ s – was selected as the final independent time step. A larger time step might not seem like the best choice, but other studies from literature also used large time step for their numerical simulations: Niyas et al. (2017) used a minimum time step of 0.01 s; Pointner et al. (2016) used time steps of 1 s and 5 s; Shatikian et al. (2005) also used a time step of 0.01 s.

4.7 Chapter summary

In this chapter the two-dimensional numerical domain was presented along with the numerical method and the mesh and time step settings. The domain consisted of a long aluminium enclosure with the PCM stored inside. A constant wall temperature was imposed for the heat transfer wall, a symmetry wall condition was applied to the top and bottom walls and an adiabatic boundary condition to the right wall. The equations governing phase change heat transfer included the Navier-Stokes equations for the mass, continuity and energy conservation, the Boussinesq density approximation for buoyancy driven flow, and the enthalpy porosity method for the phase change process.

A structured quad grid was chosen and was refined uniformly throughout the entire domain. This was done to capture the buoyancy flows and heat transfer around the phase change front as it moves through the domain. Mesh and time step independence studies were conducted. A mesh size that resulted in the best independent solution was chosen from a list of cases by calculating and comparing the errors between consecutive mesh sizes and also by calculating the GCI between mesh sizes. It was found that a 0.04×0.04 mm mesh is the first solution to reach mesh independent results. The time step independence was not as

straightforward as the mesh independence, as errors between consecutive time step cases only grew as the time steps decreased. It was decided to use the largest time step – 0.01 s.

In the next chapter the numerical method is validated by using independently produced experimental data from literature.

5. Numerical Method Validation

In this chapter the numerical method described in the previous chapter is validated against independently produced experimental data from literature. For this purpose, a suitable study had to be identified that conformed to the following criteria:

- It had to be a study on the solidification of a PCM in a rectangular container.
- The study had to contain experimental results to compare against.
- The PCM in use should be a mid- to high-temperature PCM (with a melting temperature above 200 °C).

The study chosen for the validation of the verified numerical model is an analysis of a flat plate latent heat storage design by Johnson et al. (2014). In the sections that follow, the experimental set-up and procedure followed by Johnson et al. is presented, followed by a description of how the numerical domain used for the current study was adjusted to match the size and conditions of Johnson et al., and finally the comparison between the numerical model prediction with the experimental results are presented.

5.1 Experimental setup (Johnson et al.)

Johnson et al. (2014) used a four-chamber vertical plate unit, shown in Figure 28a, which was designed specifically to house a PCM for heat storage. The two inner chambers each had an internal width of 80 mm while the outer two each had a width of 40 mm. The internal height of the unit was 1010 mm. The four chambers were separated vertically by channels in which a heat transfer fluid was pumped from the top downward during PCM charging operation and from bottom to top during PCM discharge operation. Charging occurred over a period of 14 hours during the reported experimental investigation.

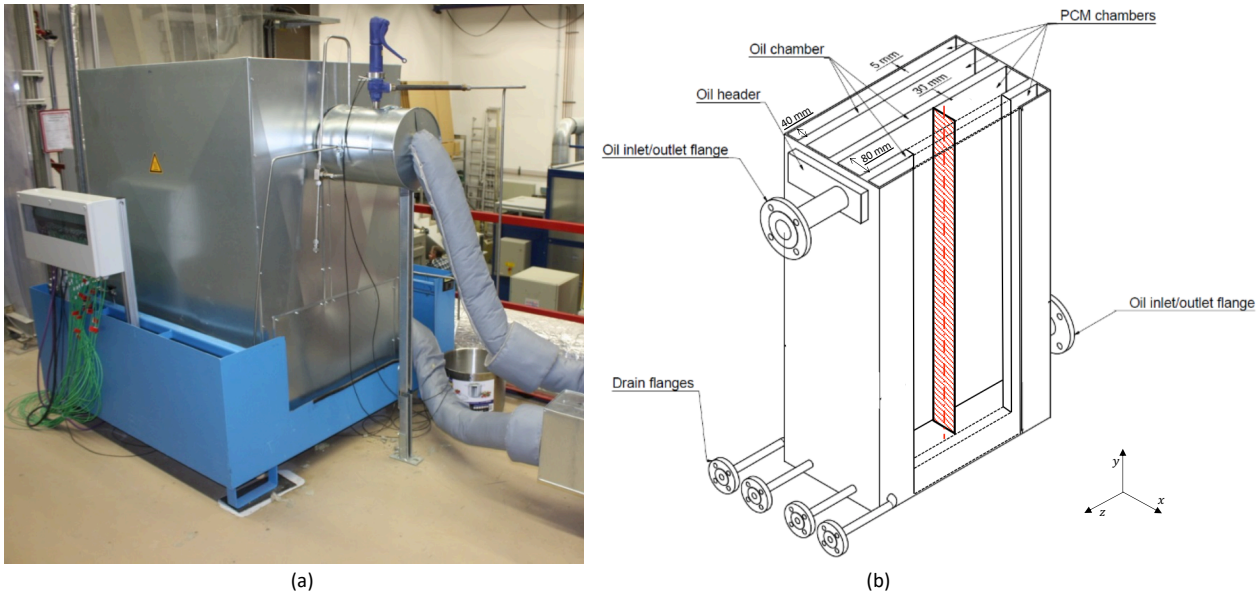

Figure 28 (a) Experimental setup of flat plate PCM storage unit and (b) a sketch of the storage tank with a two-dimensional plat cut for the simulation (Johnson et al., 2014).

A 54:46 mass percentage eutectic KNO_3-$NaNO_3$ mixture was used for this study. The storage chamber and plates were constructed from carbon steel 1.0425 and Mobiltherm 603

was used as the HTF. The material properties of the PCM, steel container and the HTF are listed in Table 11.

Table 11 Thermophysical properties of validation model PCM and fin material used by Johnson et al.

Property	Symbol	KNO_3-$NaNO_3$	Steel (1.0425)	Mobiltherm 603	Unit
Density	ρ	2050 (s)* 1959 (l)	7800	741	kg/m^3
Specific heat capacity (solid)	C_p	1350 (s) 1492 (l)	540	2550	J/kg.K
Thermal conductivity	k	0.435 (s) 0.457 (l)	51	0.122	W/m.K
Dynamic viscosity	μ	5.8×10^{-3}	-	-	kg/m.s
Thermal expansion coefficient	β	3.5×10^{-4}	-	-	K^{-1}
Melting temperature	T_{m}	219.5	-	-	°C
Latent heat of fusion	H_{f}	94000	-	-	J/kg

* The Boussinesq approximation used to model the PCM density.

The volumetric flow rate of the HTF and the temperature range about the melting temperature of the PCM were varied by between 0.5 m^3/h and 2 m^3/h and ±10 K, ±18 K and ±22.5 K respectively. The study reported most extensively on the results for 2 m^3/h and ±18 K and full results for all the thermocouples and the HTF inlet and outlet temperatures were only available for this set of parameters. This was thus the parameters that were chosen for the validation study.

It is also noteworthy to mention that experimental results of Johnson et al. (2014) were also used by Pointner et al. (2016) to validate their numerical model. Pointner et al. (2016) used the results for a volumetric flow rate of 2 m^3/h and a temperature range of ±22.5 K. The numerical setup from this study could be examined and certain aspects of it could be incorporated in the validation study but the results could unfortunately not be used for validation purposes.

The physical set up, shown in Figure 28, was simplified by Pointner et al. (2016) by only modelling one of the PCM chambers and by applying a vertical symmetry boundary condition, shown as the red shaded area in Figure 28b. The symmetry condition could be applied because the HTF flow was shown to have an equal distribution throughout all the HTF channels. This simplification reduced the computational and time resources required to solve the numerical model. The domain, with the boundary conditions and the placement of the thermocouples, is shown in Figure 30.

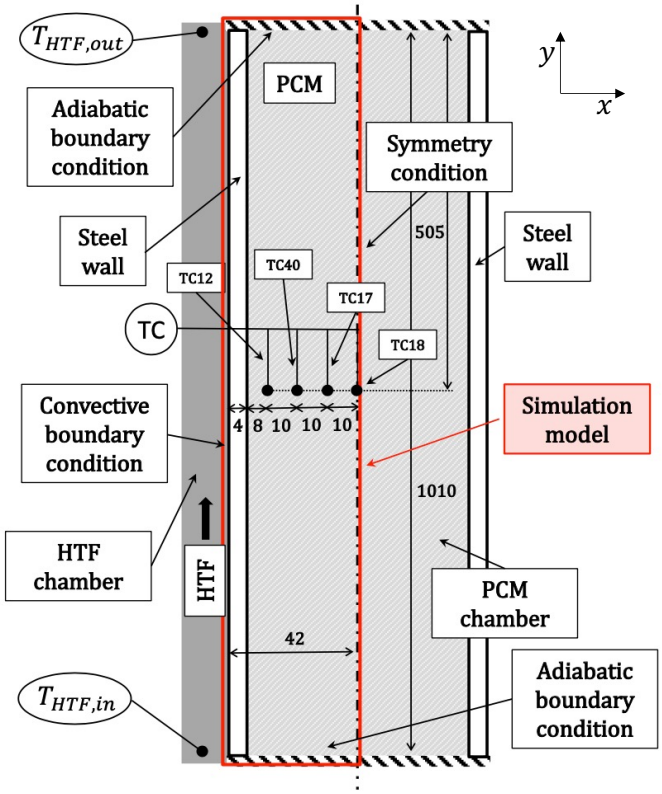

Figure 29 Numerical domain used by Pointner et al. (2016).

The top and bottom walls were kept adiabatic, while a vertical symmetry condition was applied to the inner wall. A convective boundary condition was applied to the heat transfer wall, with a convective heat transfer coefficient of h_c = 200 W/m^{2}K between the HTF and the outer steel wall, and a constant free stream temperature of 205 °C.

Pointner et al. (2016) applied a linear temperature gradient to the heat transfer wall by interpolating between the HTF inlet and outlet temperatures of the experimental results and implementing this gradient as a time dependent boundary condition.

The initial temperature of the steel, the HTF and the PCM was set to 246.2 °C (22.5 K more than the melting temperature). The convective boundary condition caused the steel and the PCM to lose energy to the environment which, in turn, caused a drop in internal temperature. Temperatures were measured at four points in the domain, shown in Figure 30, all at the midway point in the vertical direction (505 mm). Thermocouple TC12 was placed 8 mm from the heat transfer wall, to best observe the effects of the heat conduction through the wall. The rest of the thermocouples (TC40, TC17 and TC18) were all placed 10 mm from each other. By spacing them horizontally on the same vertical plane the effects of buoyancy driven flow and convective heat transfer could best be observed.

5.2 Numerical setup adjustment

The numerical setup by Pointner et al. (2016) was replicated except for a two key aspects: the heat transfer wall boundary condition and the initial temperature of the system.

Firstly, instead of applying a time dependant linear temperature gradient to the heat transfer wall, a constant temperature was used. The average temperatures of the HTF inlet and outlet were calculated from the experimental results from Johnson et al. (2014) to be 204.4 °C and

206.1 °C across the full discharge cycle with standard deviations of 0.37 °C and 2.95 °C respectively. It was thus decided to use a constant temperature of 205 °C instead of applying a temperature gradient, which reduced the computational and time resources required to reach a solution.

Secondly, the initial temperature of the steel and the PCM was set to 239.2 °C (18 K higher than the melting temperature of the PCM). The domain used for the validation study simulations, with the boundary conditions and the placement of the thermocouples, is shown in Figure 30.

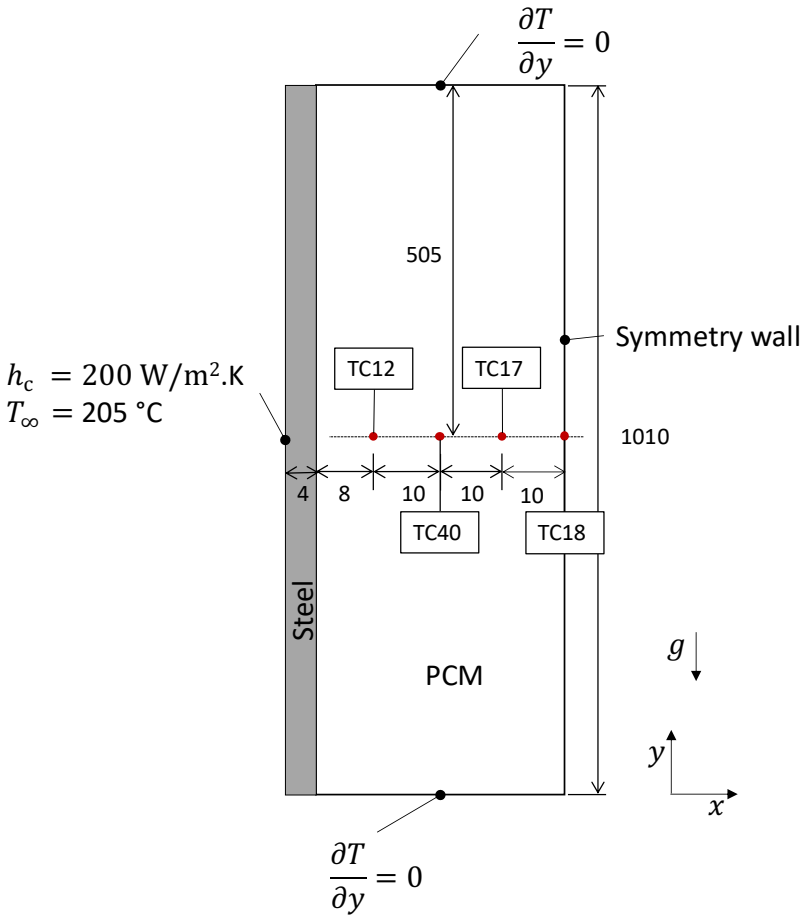

Figure 30 Numerical domain used for this validation study.

The mesh and time steps sizes determined in the independence study done in Chapter 4 was used: a uniform quadrilateral mesh with a cell size of 0.04 mm across the entire domain and a time step size of 0.01 s.

5.3 Result Comparisons

In this section a comparison of the numerically obtained temperatures against the experimental measurements are presented in a series of figures.

Consider Figure 31 for the comparisons against thermocouples a) TC12 b) TC40 c) TC17 and d) TC18. The numerical results for the thermocouple locations closer to the heat transfer wall (TC12 and TC40) showed better correlation to the experimental results than those further away (TC17 and TC18). In general, however, it can be seen that good correlation

during phase change process (temperatures close to the T_{m} line) were obtained for all thermocouple locations.

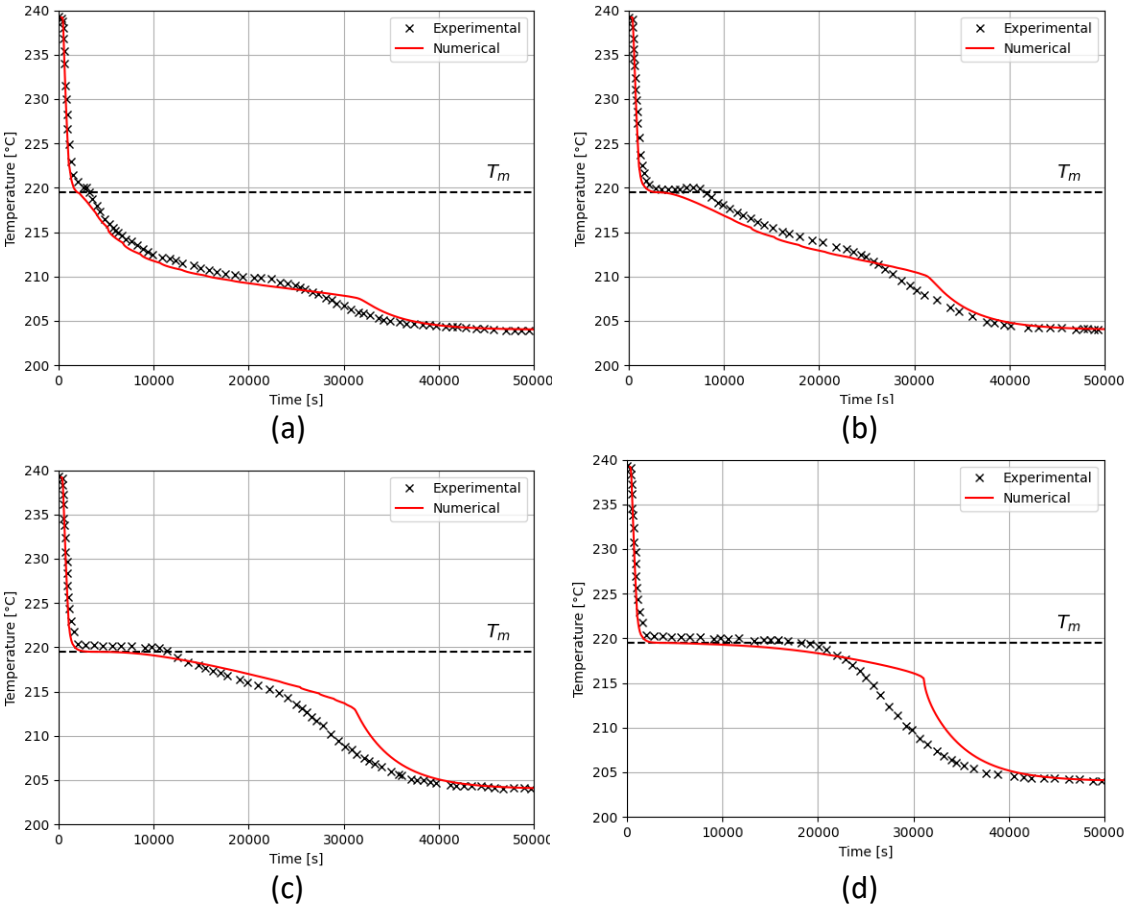

Figure 31 Validation results vs experimental for thermocouples a) TC12 b) TC40 c) TC17 and d) TC18.

Directly after phase change (TC12: 2000 s – 35000 s; TC40: 8000 s – 37000 s; TC17: 12000 s – 38000 s; TC18: 20000 s – 39000 s) the numerical model indicated lower heat transfer rates further away from the heat transfer wall. Particularly thermocouple locations TC17 and TC18 exhibited a delay in the temperature decrease compared to the experimental results.

When looking at the difference between the validation and the experimental results in Figure 32 to Figure 35, it is clear that the maximum error for all the thermocouples occurred just after 30 000 s into the run (except for TC12 which shows a higher error at the very start). TC12 had the lowest maximum error of 2.06 °C (or 1.35 °C at the 30 000 s mark), TC40 is 2.25 °C, TC17 4.87 °C and TC18 7.02 °C.

Due to the uncertainties associated with experimental measurements and material properties, there is an uncertainty range around the experimental results. For the study conducted by Johnson et al. (2014) the total uncertainty added up to ±2.65 °C. This gives an approximation of the experimental value, rather than an exact value and is shown with the error bars in Figure 32 to Figure 35. It is clear that for all the thermocouple locations, the numerical results were well within the uncertainty bands during the actual phase change

process for the relevant location, and within the error bands for locations close to the heat transfer wall, long after the phase change process was completed.

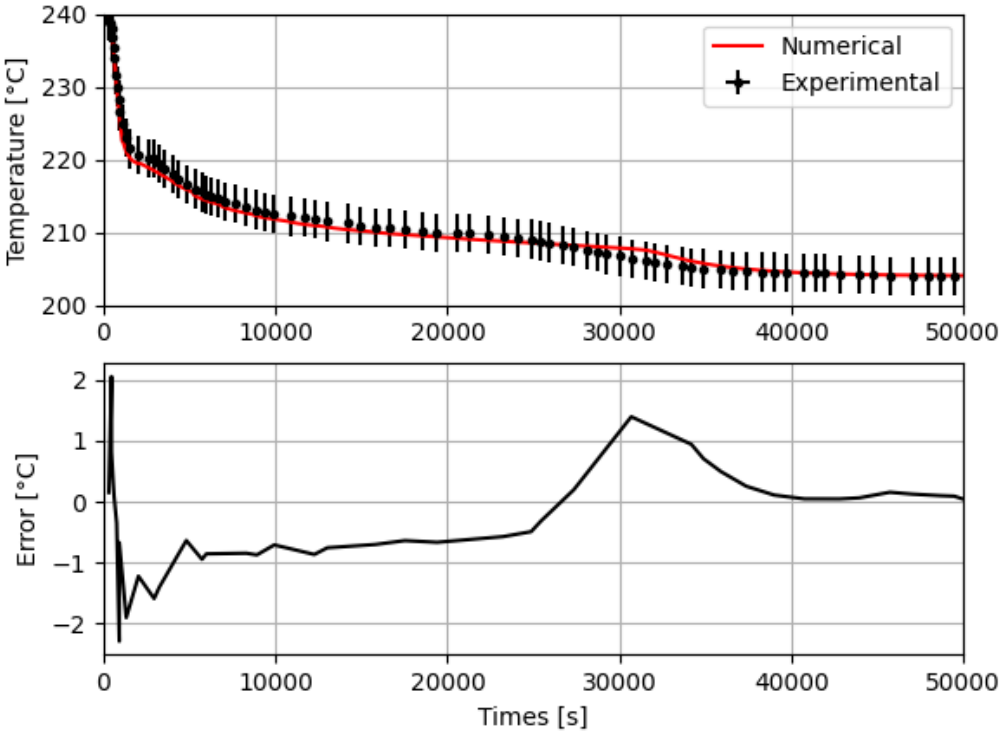

Figure 32 TC12 validation result comparison and associated errors.

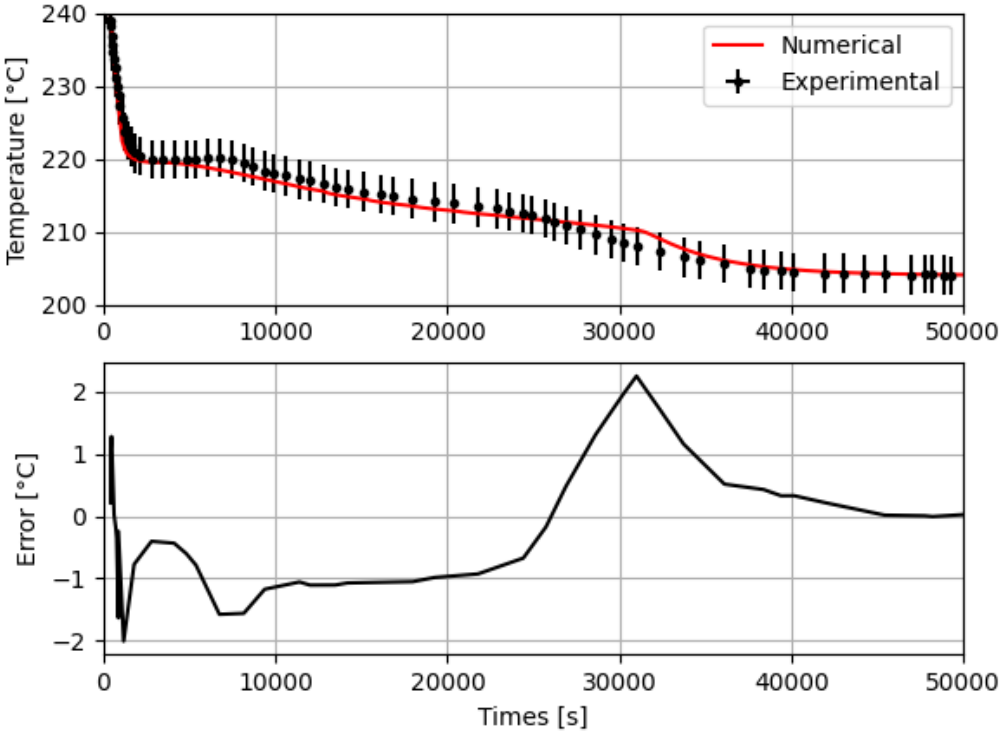

Figure 33 TC40 validation result comparison and associated errors.

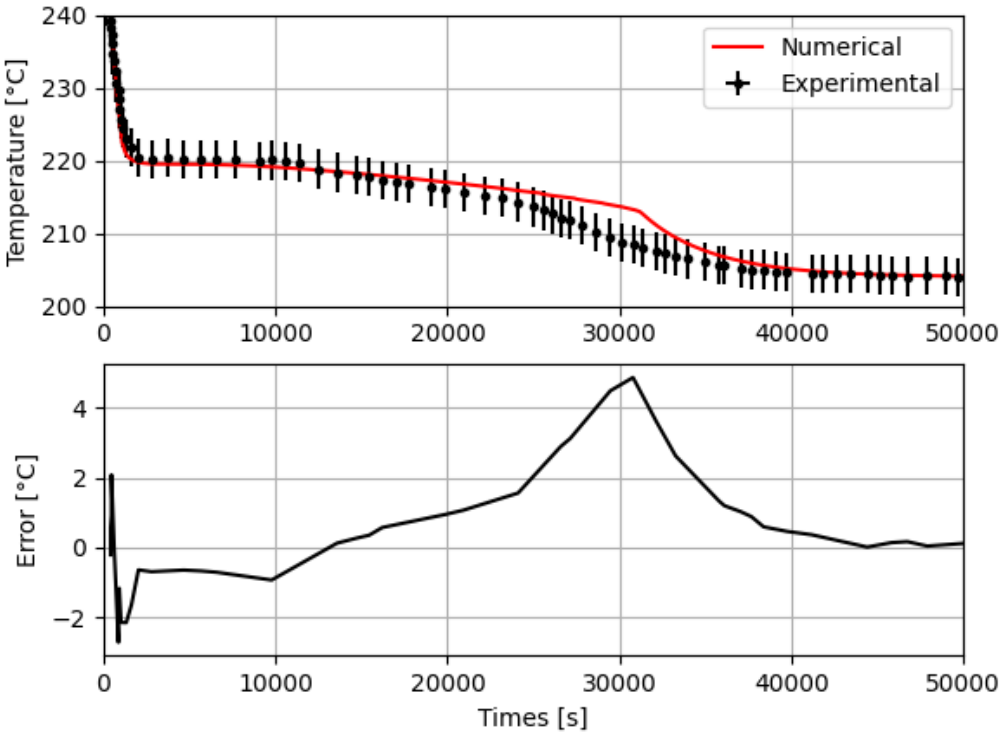

Figure 34 TC17 validation results error comparison and associated errors.

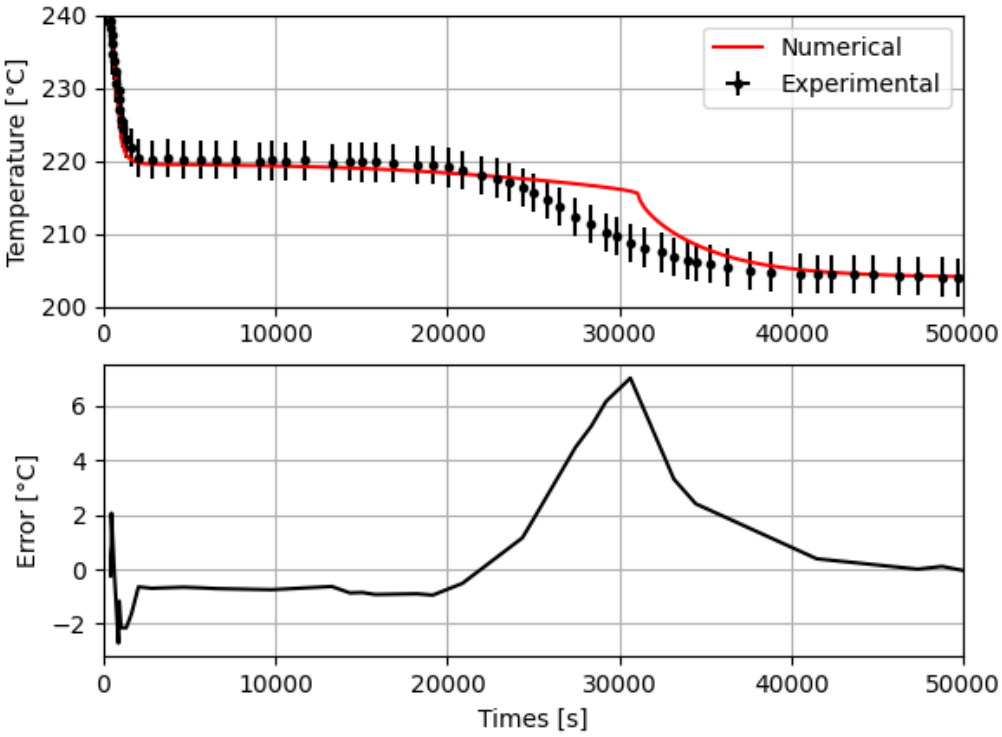

Figure 35 TC18 validation results error comparison and associated errors.

In order to better quantify the accuracy of the numerical method, the difference between the simulated temperature (T_{sim}) and the experimental temperature (T_{expr}) was calculated at each time step, based on the same approach followed by Pointner et al. (2016). The averaged deviation (D) was then calculated via summation of the absolute values of all the differences and dividing it by the number of measurements (n), including the starting condition.

$$D = \frac{\sum_{\mathrm{i}=0}^{\mathrm{i}=n} |T_{\mathrm{expr}}(t_{\mathrm{i}}) - T_{\mathrm{sim}}(t_{\mathrm{i}})|}{n+1} \tag{41}$$

The number of measurements from the validation model that fall within this uncertainty range gives a good indication of the overall accuracy of the numerical method with the respect to the experimental results. The number of measurements in the uncertainty range was divided by the total number of measurements to obtain a percentage (ξ) for each thermocouple. The accuracy metrics D and ξ, as well as each thermocouple's maximum error, are presented in Table 12.

Table 12 Validation thermocouple accuracies.

Thermocouple	D [°C]	ξ [%]	$\varepsilon_{\max}$ [°C]
TC12	0.65	100	2.06
TC40	0.77	100	2.25
TC17	1.19	86.05	4.87
TC18	1.54	83.33	7.02

From the accuracy results it is clear that the thermocouples close to the heat transfer walls show the best correlation with the experimental results, while the thermocouples further from the from the heat transfer wall show worse accuracies. It can be concluded that conduction is simulated very well, since this will be the dominant mechanism for heat transfer close to the heat transfer wall, while convection is the primary heat transfer mechanism further away from the wall. The buoyancy induced flow fields caused by natural convection could cause inaccuracies in the simulated results, particularly for the validation domain which consisted of a relatively large cavity compared to compartmentalised cavities considered in this study.

Impact on main study

When comparing the model used for the validation study with the one defined for the main study (in Chapter 4), the main differences are the geometry and the number of effective heat transfer walls in contact with the PCM. The validation study had a high, narrow geometry and two adiabatic walls, one symmetry wall and one heat transfer wall. The main study has a flat, wide geometry and one adiabatic wall and effectively three heat transfer walls: the one heat transfer wall to the left of the PCM in Figure 16 and the highly conductive fins in contact with the PCM at the top and the bottom.

The validation results showed that the thermocouples closer to the heat transfer walls produced better accuracies. The effects of natural convection is a factor that could contribute to the relative inaccuracies of the thermocouples further away from the heat transfer wall. However, even though it is important, the buoyancy driven flow for the smaller cavities in this study will not able to be as developed as in the experimental set up of Johnson et al. (2014). The validation study's geometry promotes the effects of natural convection inside the liquid PCM while the flatter and wider geometry of the main study be result in less active flow

fields. The three heat transfer walls of the main study will also ensure that more of the PCM is close to a heat transfer wall – which will ensure higher accuracies.

5.4 Chapter summary

This chapter described the validation procedure of the numerical method defined in Chapter 4. The same numerical method was followed as proposed previously, but adapted to the geometric case of the experimental study by Johnson et al. (2014). Direct comparison between the numerical model results and the experimental measurements at four thermocouple locations were performed. It was found that the thermocouple locations closer to the heat transfer wall showed good correlation to the experimental results, with all the simulation measurements falling within the uncertainty range defined by Pointner et al. (2016). The thermocouples further from the heat transfer wall had 83% and 86% of their simulation measurements inside the uncertainty range. Therefore, it was concluded that good agreement was found to exists and the numerical model was able to correctly simulate the thermal-fluid interactions in the liquid and solid phases.

In the next chapter the numerical method is applied to the geometry of interest in this study and a sample case for a particular cavity geometry is presented.

6. Sample Case Results

The results for a selected enclosure width, pitch fin distance, fin thickness and wall temperature, using the numerical model defined in Chapter 3 and 4 and validated in Chapter 5, are presented in this chapter. The intension is to highlight any points of interest during the phase change process which will be of value when the optimisation cases are considered in the following chapter.

6.1 Dimensions and boundary conditions

For this sample case, the width of the domain was chosen to be $L = 50\,mm$ and a pitch distance of $P = 8\,mm$ was selected. The fin thickness was selected to be $t_\mathrm{f} = 0.8\,mm$ (or $\frac{1}{2}t_\mathrm{f} = 0.4\,mm$), such that the total volume of the total area of the fins would be 10% of the volume of the entire enclosure (the fins plus the PCM). The wall temperature was selected to be $\Delta T = 10\,\mathrm{K}$, or $T_\mathrm{w} = 296\,°\mathrm{C}$. The domain with the selected parameters is shown in Figure 36.

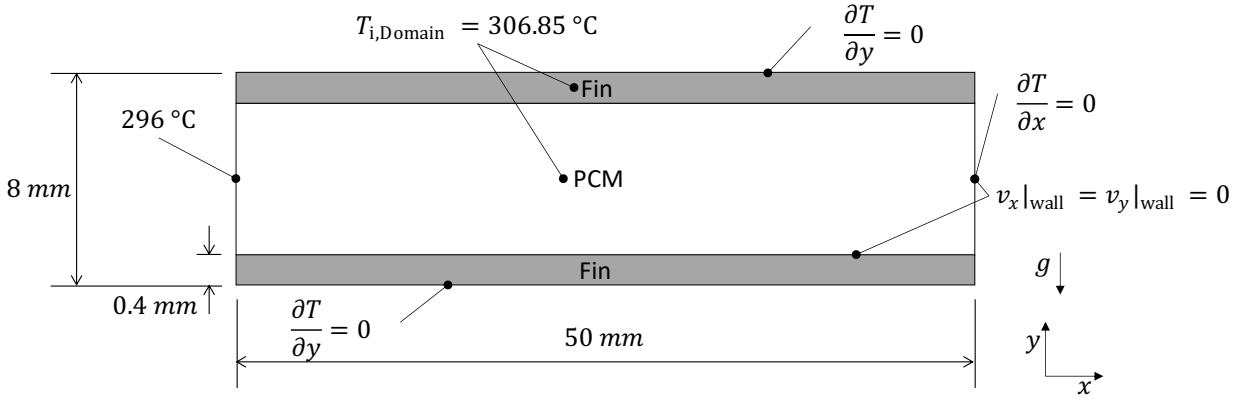

Figure 36 Numerical domain for $L = 50\,mm$, $P = 8\,mm$, $t_\mathrm{f} = 0.8\,mm$, $T_\mathrm{w} = 296\,°\mathrm{C}$ $T_{\mathrm{i,Domain}} = 306,85\,°\mathrm{C}$.

The entire enclosure, the PCM and the fin material, was initialise with a temperature of $T_{\mathrm{i,Domain}} = 306.85\,°\mathrm{C}$ (or 580 K), which is only slightly higher than the phase change temperature of $NaNO_3$ such that the solidification process will start very soon after initialisation.

6.2 Sample Results

The heat flux (q) at the HTF wall, and solid fraction (ψ) against time are shown in Figure 37 and Figure 38 respectively. From Figure 37 it can be seen that the initial heat flux is high and starts at 100 kW/m^2. Soon after the initiation, the heat flux significantly reduces and then exhibits a steady drop. This is also reflected in Figure 38 showing a decline in the rate of solidification.

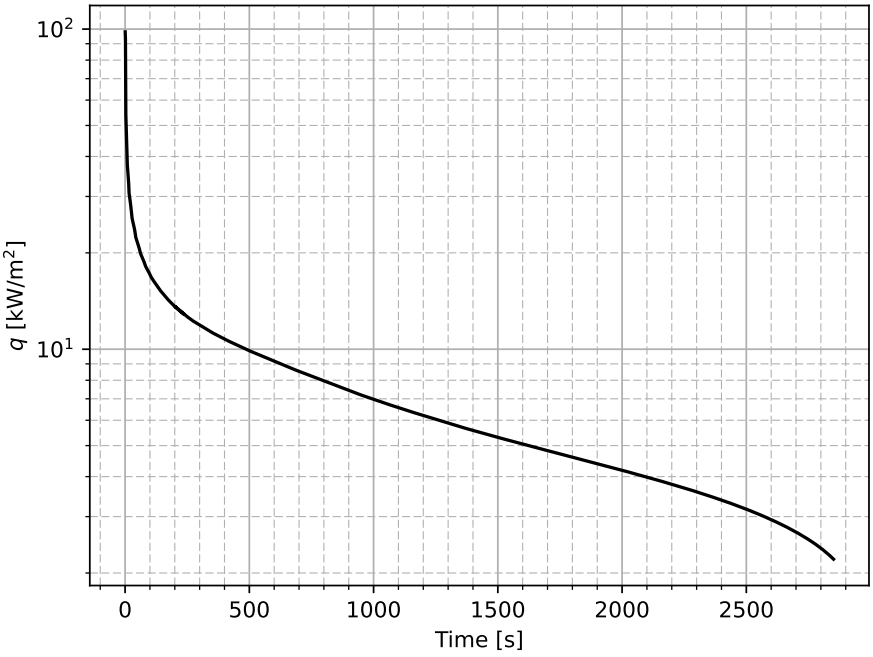

Figure 37 Heat flux vs time.

During the first 200 s in Figure 37, the heat flux out of the system is relatively quick when compared to 300 s onwards. This is due to the highly conductive aluminium fin conducting the heat quickly and after that the much slower heat transfer from the PCM out of the system.

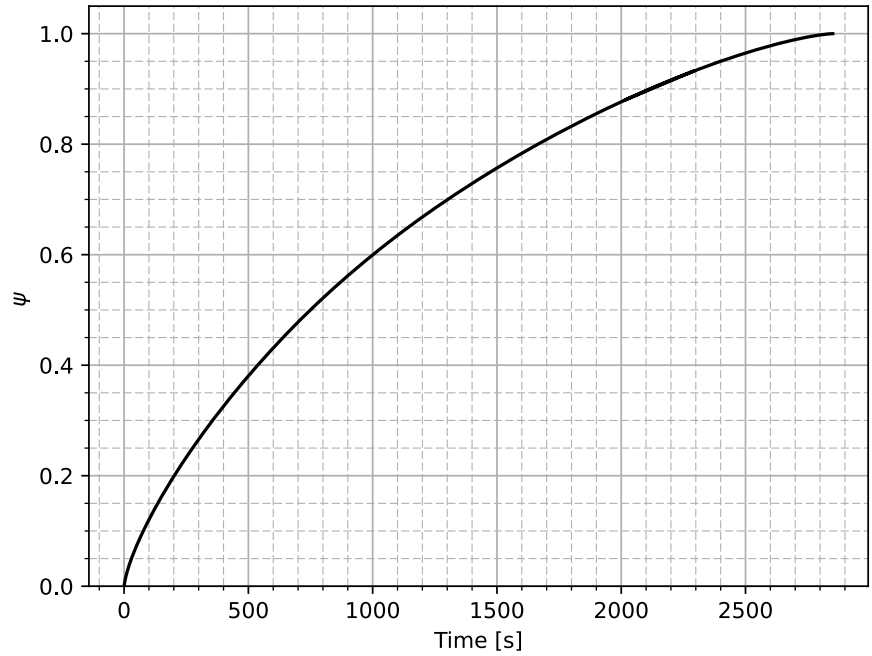

Figure 38 Solid fraction vs time.

The PCM solidifies quickly initially as heat is transferred easily between the liquid PCM and the aluminium fins. As the PCM against the fins starts solidifying, the solidification is slowed down as the low thermal conductivity of the PCM impedes the conductive heat transfer from the PCM to the fins.

The phase boundary progression is shown in Figure 39 at a) 100 s b) 1000 s and c) 2000 s, where red represents a fully liquid PCM ($\psi = 1$), blue fully solid ($\psi = 0$) and green/yellow the mushy zone (as defined earlier).

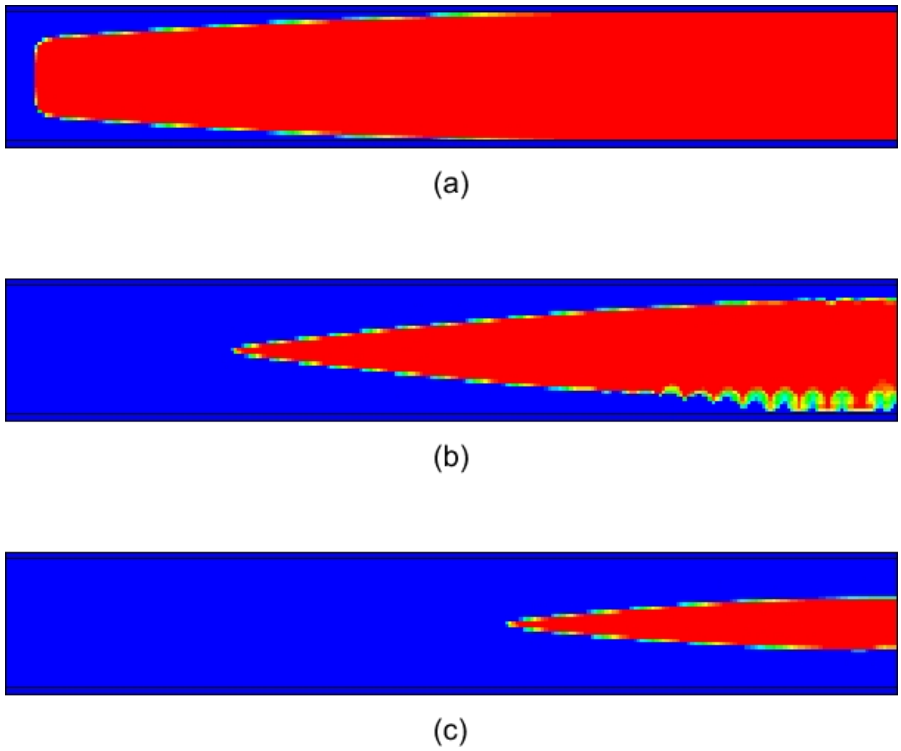

Figure 39 Phase boundary progression at a) 100 s b) 1000 s and c) 2000 s.

From this it can be seen how the PCM closest to the fins and heat transfer wall start solidifying first (in Figure 39a and b) which causes the reduction in heat transfer rate seen in Figure 37 and Figure 38. The effects of buoyancy induced flow fields can, however, be seen in the plumes forming close to the bottom fin in Figure 39b. Towards the end of the process the buoyancy flow fields seem to weaken as the phase boundary in Figure 39c returns to being regular and no more plumes are present.

6.3 Chapter summary

The numerical model, defined in Chapter 4 and validated in Chapter 5, was used and an sample case enclosure width of $L = 50\,mm$, fin pitch $P = 8\,mm$, fin thickness $t_f = 0.8\,mm$ initial temperature $T_{\mathrm{i,Domain}} = 306{,}85\,°\mathrm{C}$ and wall temperature difference $\Delta T = 10\,\mathrm{K}$ was selected as the parameters. The simulation was run until the entire PCM was solidified.

The results from the heat flux and solid fraction show a relatively fast initial heat transfer period which slows down as the PCM starts to solidify and its low thermal conductivity impeding the conductive heat transfer out of the PCM. The phase boundary progression confirms the PCM solidification around the heat transfer surfaces but also showed evidence of buoyancy driven natural convection flow fields which could have a positive effect on the heat transfer rate of the system.

In the next chapter the simulation conducted in here are repeated for several geometric cases in order to perform a parametric study to maximise the heat transfer rate from the PCM.

7. Parametric Study

In this chapter the design variables and the initial conditions of the parametric study is defined and the results obtained are presented and discussed.

7.1 Design variables

As mentioned, the purpose of this study is one of optimisation, and thus design variables had to be selected. The focus of the optimisation was decided to lie with the geometry of the latent heat TES system enclosure, where the choice of design variables was the width of the enclosure and the pitch and the thickness of the fins: respectively L, P and t_f in Figure 40.

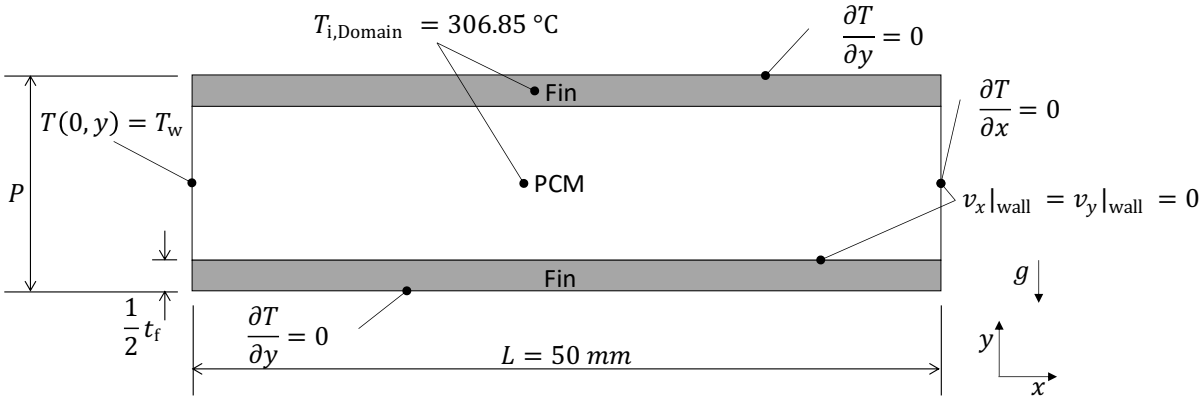

Figure 40 Numerical domain.

The different variables could have different effects of the heat transfer of the system. Increasing the fin thickness would result in a higher volume of highly conductive fins which would increase the conductive heat transfer of the system. This would, however, also result in a smaller PCM volume and thus smaller overall energy storage capacity. Narrowing the enclosure width would result in a higher percentage of the PCM being closer to the heat transfer wall, which could also increase the conductive heat transfer rate. Changing fin pitch would affect the vertical height of the enclosure and thus have an effect on the convective heat transfer through buoyancy driven flow.

Investigating the effect of buoyancy driven flow on the overall heat transfer presented an interesting topic for this study, rather than focussing on conductive heat transfer only. It was thus decided to optimise the pitch of the fin whilst keeping the width (L) of the enclosure constant. The fin thicknesses (and thus volume, since the geometry is two dimensional) were changed in relation to the pitch such that the volume of the fins was always 10% of the total volume of the enclosure (the PCM plus the fins' volume). In studies found in literature the total fin volume range from 5% (Kamkari and Shokouhmand, 2014) and 7% (Velraj et al., 1999) to 18% (Debich et al., 2020).

In order to ensure the scalability of the results obtained from the study, the optimisation parameter was non-dimensionalised. This was done by taking the ratio of the pitch of the fins to the width of the enclosure and arriving at the aspect ratio of the PCM:

$$a^* = \frac{P}{L} \tag{42}$$

During the numerical simulations, the wall temperature (T_w in Figure 40) was kept constant for a set of fin pitches. Different temperature differences between the PCM melting temperature and the wall temperature (ΔT) will have an effect on the strength of the buoyancy driven flow in the liquid PCM and could result in a different optimum geometry. Two sets of fin pitches were thus defined and run, one at $\Delta T = 10\ \mathrm{K}$ ($T_w = 296\ °\mathrm{C}$) and the second set at $\Delta T = 5\ \mathrm{K}$ ($T_w = 301\ °\mathrm{C}$).

The set of values selected for each parameter is summarised in Table 13.

Table 13 Numerical study parameter set.

Case	ΔT	T_w	L	P	a^*	t_f
	[K]	[°C]	[mm]	[mm]	-	[mm]
1	10	296	50	8	0.16	0.8
2				7	0.14	0.7
3				6	0.12	0.6
4				5	0.1	0.5
5				4	0.08	0.4
6				3	0.06	0.3
7				2	0.04	0.2
8	5	301		8	0.16	0.8
9				7	0.14	0.7
10				6	0.12	0.6
11				5	0.1	0.5
12				4	0.08	0.4
13				3	0.06	0.3
14				2	0.04	0.2

Seven pitch values (P) were considered between 2 mm and 8 mm in order to find the fin pitch and aspect ratio at which the heat transfer rate will be at a maximum. These pitch values resulted in fin thicknesses ranging from 0.2 mm and 0.8 mm (the smaller sizes could present a challenge when manufacturing), and domain aspect ratios of between 0.04 and 0.16. Smaller fin pitch sizes were chosen because that is the range where an optimum is expected to exist (additionally, it lowers the simulation time of each run, since modelling transient phase change is a computationally and time expensive operation). A largest fin pitch of 8 mm was selected and then decreased by 1 mm until a minimum pitch of 2 mm. This gives a good range of fin pitches.

7.2 Results

The results are presented in this section according to the temperature difference between the heat transfer wall condition and the PCM melting temperature.

7.2.1 $\Delta T = 10\ \mathrm{K}$

The heat flux (q) and solid fraction (ψ) is shown in Figure 41 and Figure 42 for cases 1 to 7 – with a wall temperature difference of $\Delta T = 10\ \mathrm{K}$.

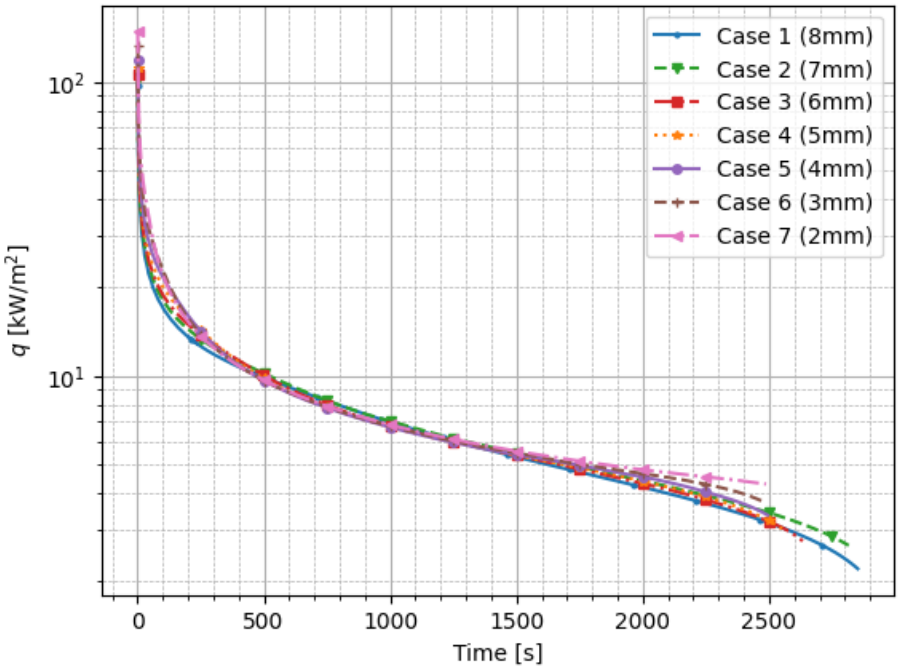

Figure 41 Heat flux results $\Delta T = 10\ \mathrm{K}$.

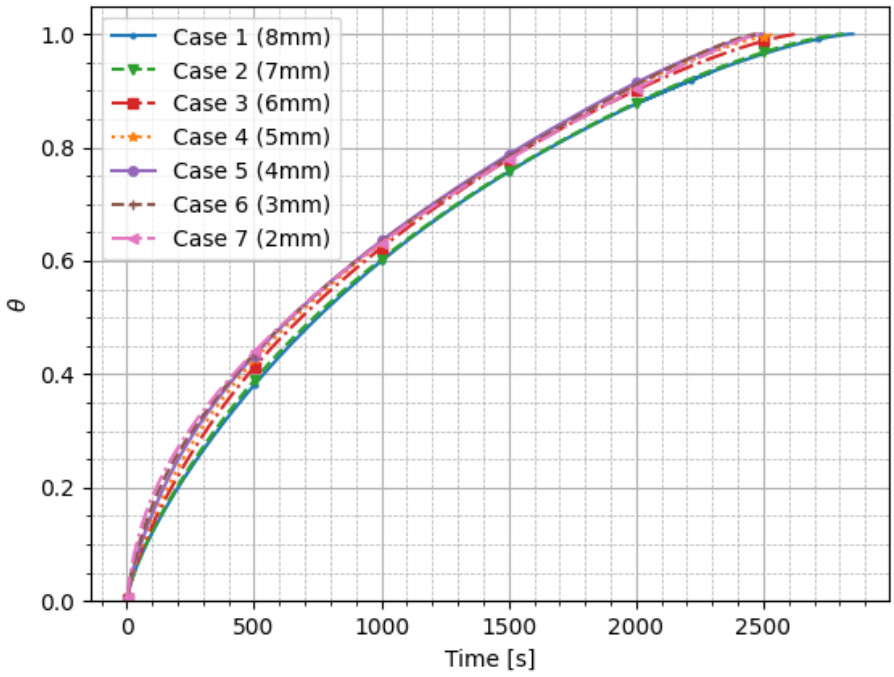

Figure 42 Solid fraction results for $\Delta T = 10\ \mathrm{K}$.

When looking at Figure 41 and Figure 42, it can be seen that the time to solidification and the trend across the run time do not vary much for the different cases.

The difference between two cases (i and j) can be expressed as the difference in ψ at a certain time step:

$$\Delta\psi_{t,ij} = \psi_{t,i} - \psi_{t,j} \tag{43}$$

or as a difference in time taken to reach a certain ψ:

$$\Delta t_{\psi,ij} = t_{\psi,i} - t_{\psi,j} \tag{44}$$

As an example, when considering Figure 42 the difference in solid fractions between case 7 (i) and case 1 (j) can thus be calculated at a 500 s (t) using equation (43):

$$\Delta\psi_{500,71} = \psi_{500,7} - \psi_{500,1}$$

$$\Delta\psi_{500,71} = 0.439 - 0.381$$

$$\Delta\psi_{500,71} = 0.058$$

The differences between the cases with the smallest and the largest solid fractions ($\Delta\psi_{t,maxmin}$) are plotted in 100 s intervals in Figure 43. The differences increase in the early stages of the solidification before decreasing approximately halfway through and finally increasing again towards the end of the solidification process.

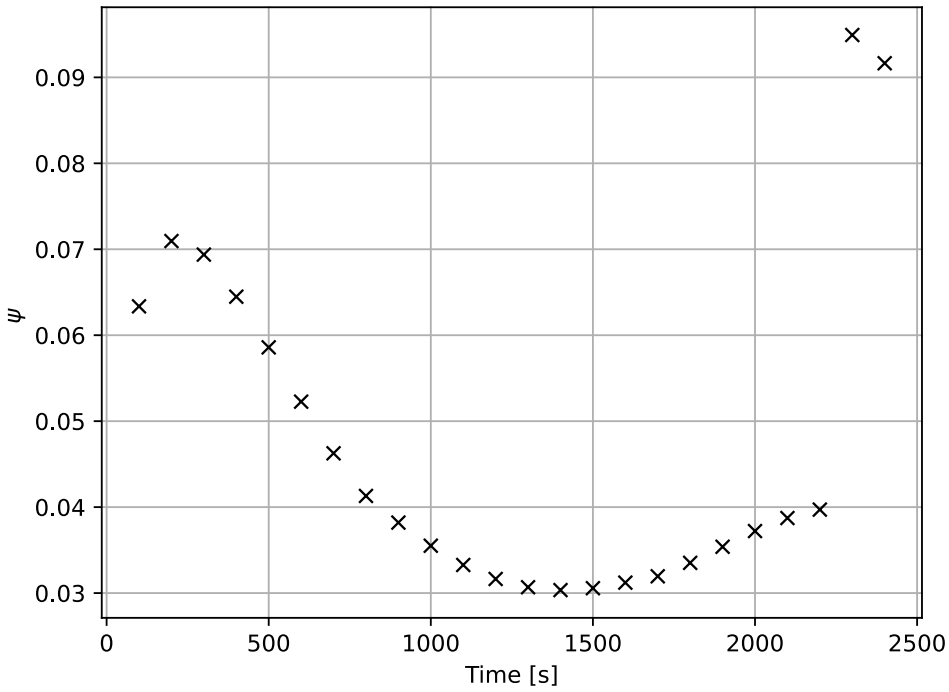

Figure 43 Difference between minimum and maximum ψ values for $\Delta T = 10$ K.

Alternatively, the time taken for a case to reach a certain solidification can also be considered ($t_{\psi,i}$). The time steps at which the different simulation cases reached ψ values of 0.25, 0.5, 0.75 and 1 are listed in Table 14 and presented graphically in Figure 44.

Table 14 Solidification time progress for $\Delta T = 10\ K$.

Case	a^*	P	$\psi = 0.25$	$\psi = 0.5$	$\psi = 0.75$	$\psi = 1$
	-	mm	t [s]			
1	0.16	8	281	761	1437	2647.5
2	0.14	7	267	735	1470	2815
3	0.12	6	247	703	1416	2551
4	0.1	5	220	661	1375	2551
5	0.08	4	202	645	1368	2493.5
6	0.06	3	188	643	1381	2471.5
7	0.04	2	174	639	1392	2488

The solid fraction results of all the cases start out close together, with case 7 the fastest to reach $\psi = 0.25$ in 174 s and case 1 the slowest at 281 s. Using equation (44), the difference between case 1 (i) and case 7 (j) can be calculated as:

$$\Delta t_{0.25,17} = t_{0.25,1} - t_{0.25,7}$$

$$\Delta t_{0.25,17} = 281\ s - 174\ s$$

$$\Delta t_{0.25,71} = 107\ s$$

The cases start growing slightly further apart until case 7 reaches $\psi = 0.5$ first in 639 s, 122 s faster than case 1 – which was the slowest at 761 s – and then come closer together with case 6 this time the fastest in reaching $\psi = 0.75$ in 1381 s, only 102 s faster than the slowest case (which is now case 2) that reach 75% solidification in 1470 s. In the final solidification phase, the cases diverge again with the fastest case (still case 6) reaching full solidification ($\psi = 1$) in 2471.5 s, 343.5 s faster than case 2 which is still the slowest at 2815 s.

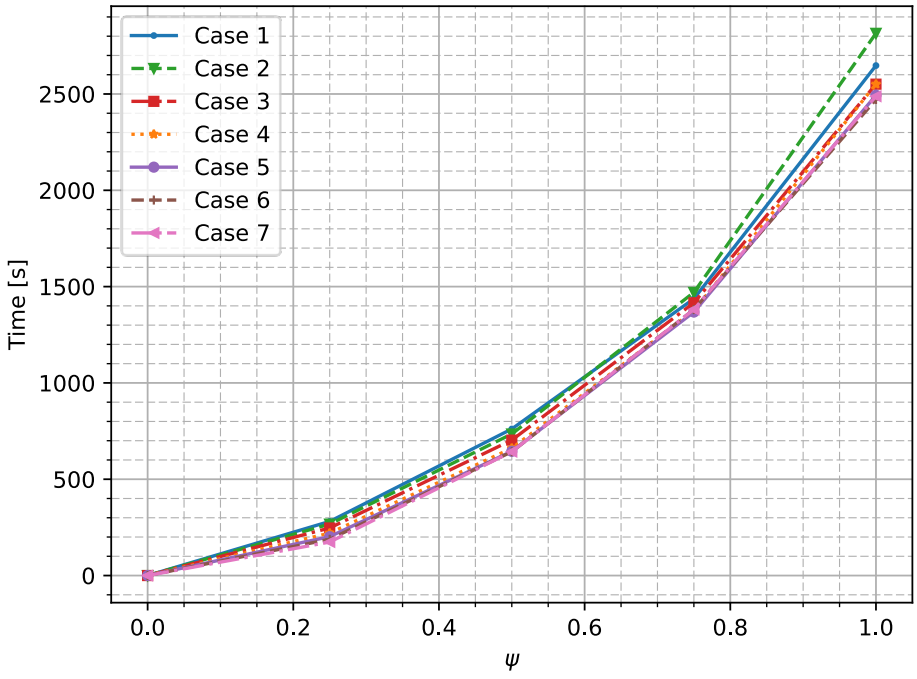

Figure 44 Solidification time progress for $\Delta T = 10\ K$.

Both methods of comparing – looking at the difference in time taken to reach a certain solidification and the difference in solidification at a certain time step, show the same trend of the cases starting off closes together, diverging early on in the process before converging and finally diverging again towards the end of the process. This difference represents the effective rate of heat transfer out of the system.

It is interesting to note that the case which took the longest is case 2, which has an aspect ratio of 0.14 – which is not the largest aspect ratio – and the case which solidified the quickest is case 6, which has an aspect ratio of 0.06 – which is not the smallest aspect ratio.

The phase boundary progression is now shown in Figure 45 at a) 100 s b) 500 s c) 1000 s d) 1500 s e) 2000 s and f) 2400 s for a pitch distance of (1) 8 mm (2) 7 mm (3) 6 mm (4) 5 mm (5) 4 mm (6) 3 mm and (7) 2 mm. Red represents a fully solid ($\psi = 1$) and blue fully ($\psi = 0$) liquid PCM.

In the early stages of the solidification process (Figure 45a and b) the phase boundary develops uniformly, from the fins and heat transfer walls inwards, due to conduction being the dominant method of heat transfer. As expected, the smallest pitch distance solidifies the quickest in this stage since a higher volume fraction of the PCM is in direct contact with the fin.

As the solidification progresses and buoyancy induced flow fields start to form (Figure 45b and c and d), the phase boundary starts to become irregular, and it can be seen where the PCM solidifies at a higher rate close to the flow fields. These irregularities in the phase boundary exists for all the pitch distances. As the PCM starts solidifying, the higher density solid PCM sinks to the bottom of the enclosure and results in this region being slightly thicker than the solid region close to the top fin. This is seen most prominently in Figure 45c. The buoyancy-induced flow fields also caused mixing in the liquid region, which promotes heat transfer within the liquid region causing a more uniform temperature in the liquid, but this prevents the solidification of local regions.

During the last stages of the solidification process more than 50% of the PCM has solidified and conduction starts to become the dominant heat transfer mechanism. Figure 45e (1) to (4) shows a uniform phase boundary as the thickness of solid PCM layer between the fin and the liquid PCM slows down the buoyancy forces. Figure 45e (5) to (7) still shows an irregular phase boundary as the buoyancy flow still plays an active role in the heat transfer for the smaller pitch distances. In Figure 45f (6) and (7) the entire PCM is either solid or in the mushy region for a 2 mm pitch distance and the phase boundary is completely uniform for the rest of the pitch distances.

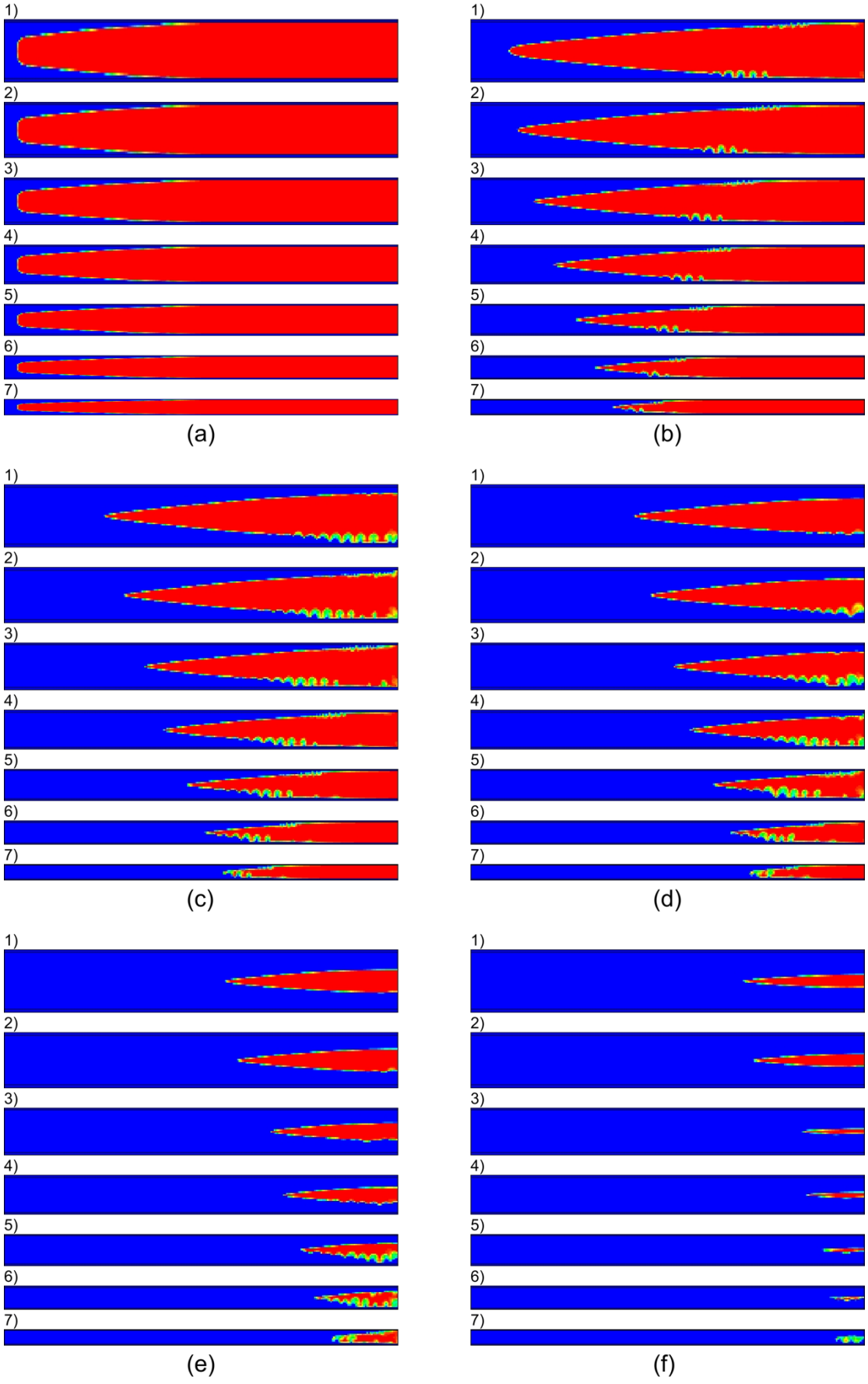

Figure 45 Phase boundary for $\Delta T = 10\ K$ at a) 100 s b) 500 s c) 1000 s d) 1500 s e) 2000 s and f) 2400 s for different pitch distances.

7.2.2 $\Delta T = 5$ K

The heat flux (q) and solid fraction (ψ) for cases 8 to 14 – with a wall temperature difference of $\Delta T = 5$ K is shown in Figure 46 and Figure 47.

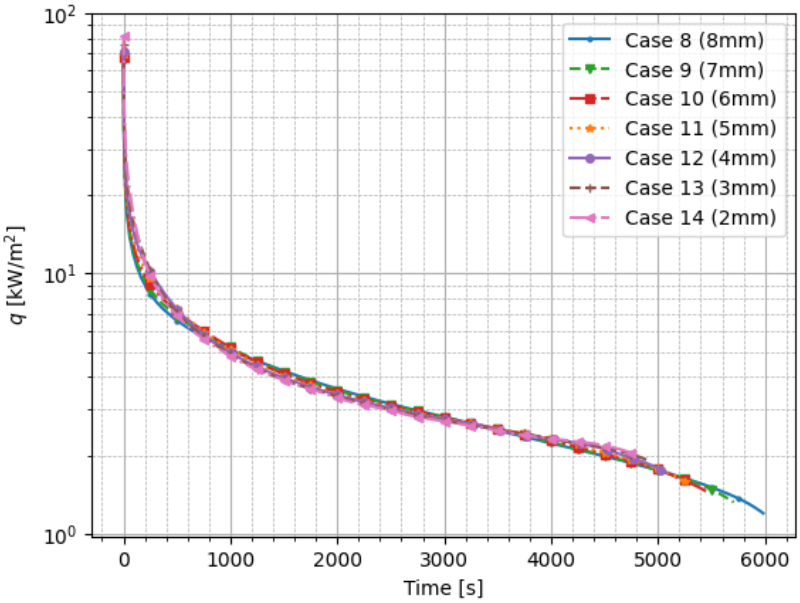

Figure 46 Heat flux results $\Delta T = 5$ K.

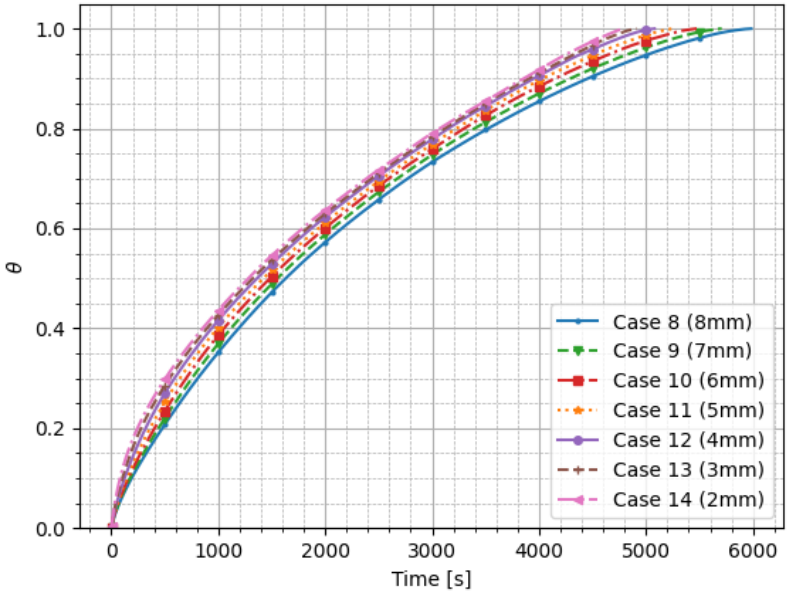

Figure 47 Solid fraction results $\Delta T = 5$ K.

Again, all the cases start out close together, as can be expected, but there is not a stage where the cases clearly converge as seen in the cases for $\Delta T = 10$ K. When looking at the differences between the cases with the smallest and largest ψ in Figure 48, plotted at 100 s intervals, the same trend seen in Figure 43 can again be seen here with $\Delta\psi_{t,maxmin}$ starting

off small, increasing then decreasing up until approximately halfway (slightly more than halfway for this T_w) before finally increasing again towards the end.

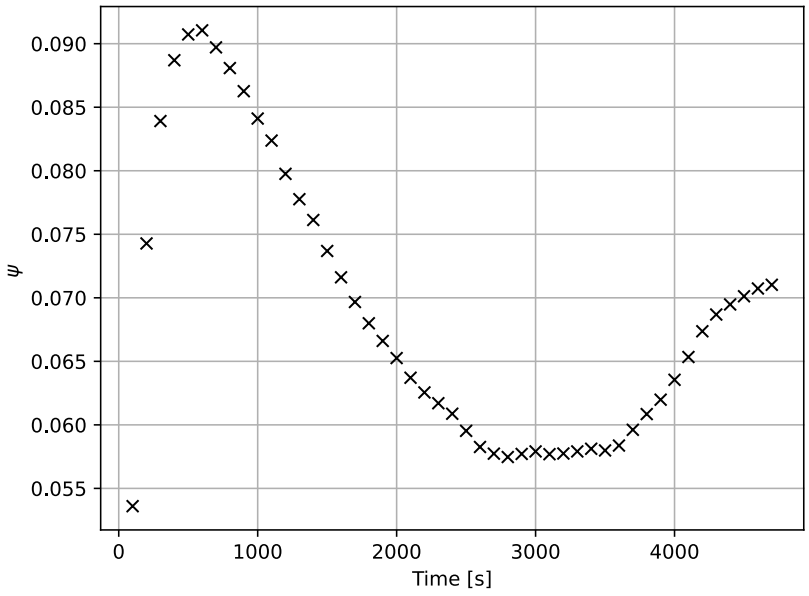

Figure 48 Difference between minimum and maximum ψ values for $\Delta T = 5$ K.

The time steps at which the different simulation cases reached ψ values of 0.25, 0.5, 0.75 and 1 for $\Delta T = 5$ K are listed in Table 15 and presented graphically in Figure 49.

Figure 49 shows the difference between the smallest and the largest time steps keep getting larger as the solidification progresses, with case 14 the fastest to each ψ and case 8 the slowest.

Table 15 Solidification time progress for $\Delta T = 5$ K.

Case	a^*	P	$\psi = 0.25$	$\psi = 0.5$	$\psi = 0.75$	$\psi = 1$
	-	mm	[s]			
8	0.16	8	637	1630	3127	5984
9	0.14	7	592	1552	3018	5708
10	0.12	6	545	1482	2935	5474.5
11	0.1	5	494	1421	2868	5262.5
12	0.08	4	445	1362	2798	5079.5
13	0.06	3	399	1321	2761	4912
14	0.04	2	363	1280	2721	4797

Case 14 reaches $\psi = 0.25$ in 363 s and case 8 in 637 s, for a difference of 274 s. The cases keep diverging with case 14 reaching $\psi = 0.5$ in 1280 s, 350 s faster than case 8 (at 1630 s), $\psi = 0.75$ in 2721 s and $\psi = 1$ in 4797 s – 406 s and 1187 s faster than case 8 that got to $\psi = 0.75$ in 3127 s and $\psi = 1$ in 5984 s.

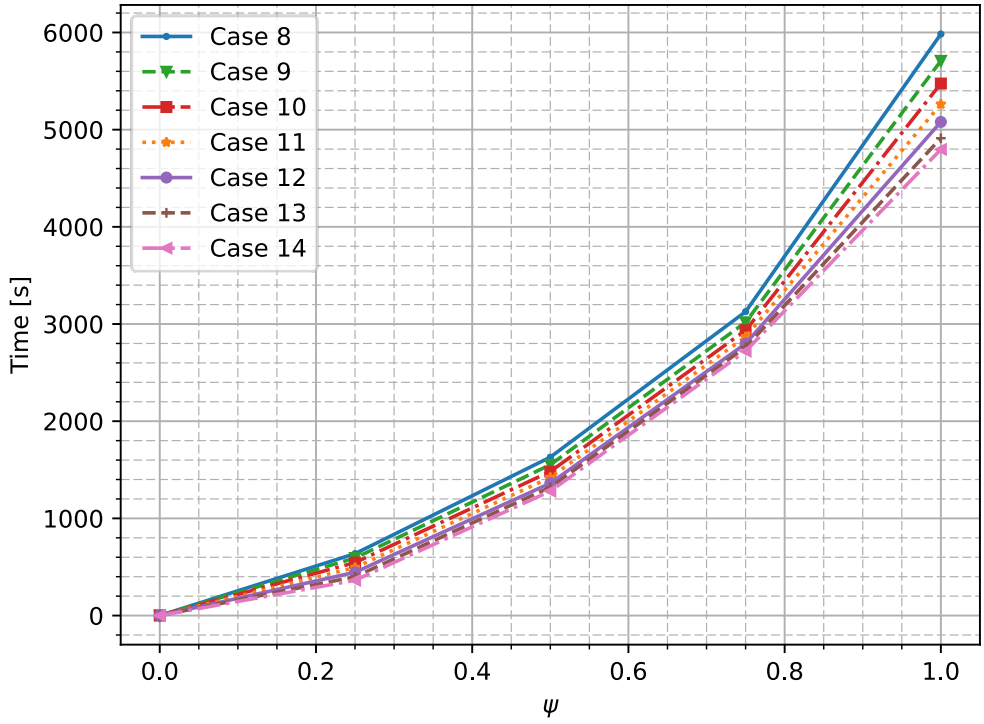

Figure 49 Solidification time progress for $\Delta T = 5$ K.

Unlike for the previous set of cases, both methods of comparing do not show the same trend: when comparing $\Delta\psi_t$ between the cases the differences between cases follow the same trend as with $\Delta T = 10$ K, whereas when comparing Δt_ψ shows only increasing differences between cases for increasing solid fractions.

Figure 50 shows the phase boundary progression for $\Delta T = 5$ K at a) 100 s b) 1000 s c) 2000 s d) 3000 s e) 4000 s and f) 4700 s for a pitch distance of (8) 8 mm (9) 7 mm (10) 6 mm (11) 5 mm (12) 4 mm (13) 3 mm and (14) 2 mm. Again red represents $\psi = 1$ and blue $\psi = 0$ for the PCM.

The same trends seen in Figure 45 for the phase boundary progression of $\Delta T = 10$ K can be seen in Figure 50. In the initial stages (Figure 50a), conduction is the dominant method of heat transfer and the phase boundary develops uniformly. In Figure 50b natural convection starts playing a role in the system heat transfer and the phase boundary starts breaking up as buoyancy induced flow fields starts to form. In Figure 50c and d, approximately halfway through the solidification process, the flow fields are at their most active for all pitch distances. During the last third of the solidification process (Figure 50e and f), conduction starts taking over again as the dominant heat transfer mechanism and the phase boundary starts getting regular for the larger pitch distances in Figure 50e (8) and (9) until eventually all the pitch distances have a regular phase boundary in Figure 50f.

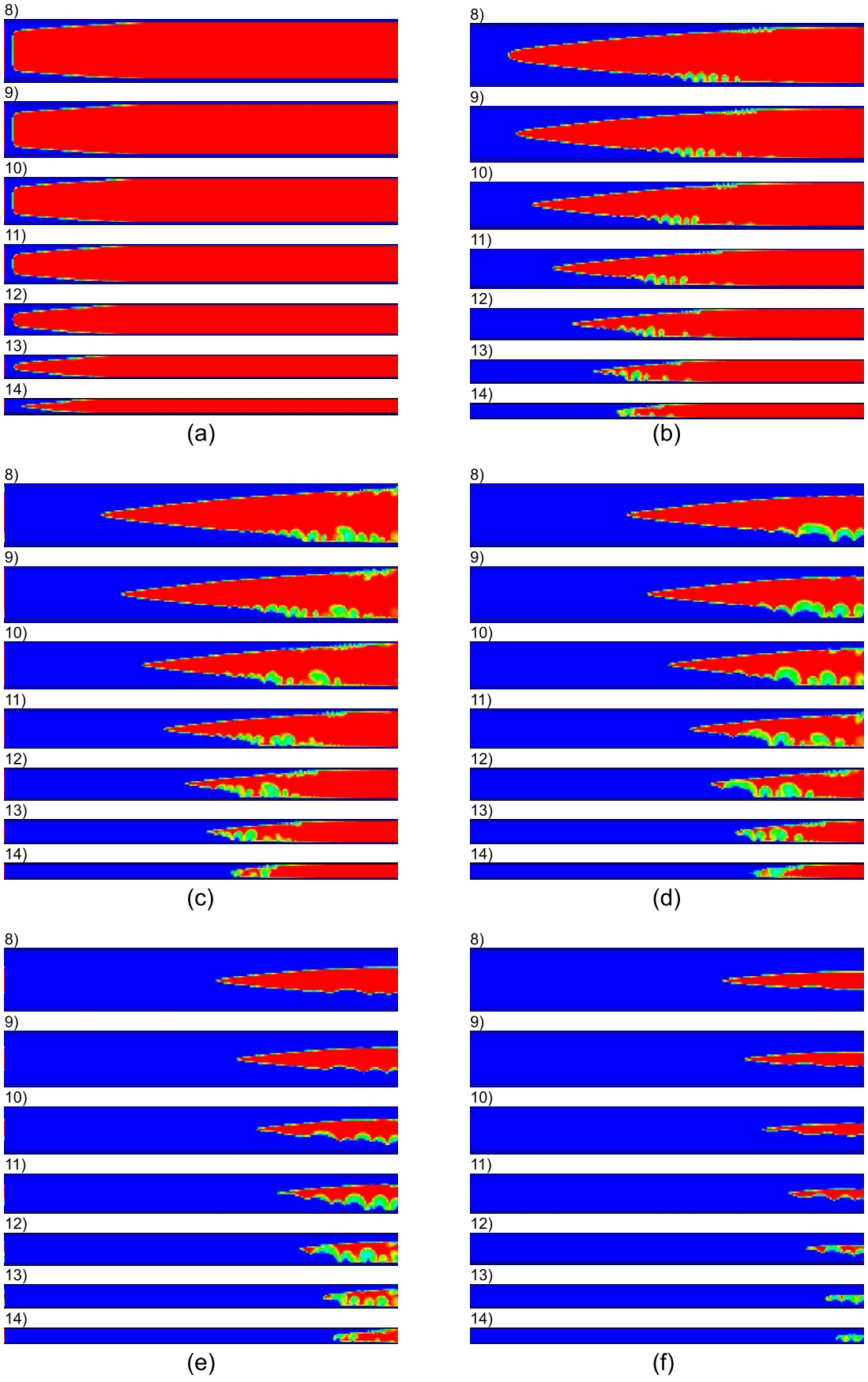

Figure 50 Phase boundary for $\Delta T = 5$ K at a) 100 s b) 1000 s c) 2000 s d) 3000 s e) 4000 s and f) 4700 s for different pitch distances.

The second set of cases (for $\Delta T = 5\ \mathrm{K}$) had a directly proportionate relationship with the aspect ratio of the fins – as a^* decreased, so did the time required to fully solidified. The set of cases for $\Delta T = 10\ \mathrm{K}$ did not follow this trend. A possible explanation for this behaviour is the influence of stronger natural convection flow field in the first set of cases due to there being a larger temperature difference between the initial temperature of the domain and the wall temperature. The (i) phase boundary and (ii) velocity fields are shown for (a) $\Delta T = 10\ \mathrm{K}$ and (b) $\Delta T = 5\ \mathrm{K}$ at a solidification of $\psi \approx 0.85$ for a pitch distance of 4 mm in Figure 51 and 2 mm in Figure 52. A solidification of $\psi \approx 0.85$ occurs after approximately 1700 s for $\Delta T = 10\ \mathrm{K}$ and approximately 3300 s for $\Delta T = 5\ \mathrm{K}$ and the velocities range from 0 m.s^{-1} (blue) and 1×10^{-5} m.s^{-1} (red).

When comparing the two cases in Figure 51, at a similar stage in the solidification process, one would expect the case with the lower boundary condition (Figure 51a) to have stronger velocity flow fields. It does seem like natural convection currents are present in the enlarged image of Figure 51a (ii) but there appears to be convection currents in the enlarged image in Figure 51b (ii) as well. Additionally, the velocity fields close to the fin in Figure 51b seem to be much stronger than the corresponding fields in Figure 51a. The velocity fields in Figure 52a and b look almost identical with both of them showing high velocities close to the fin and less evidence of convection currents – which is expected due to the smaller fin spacing favouring conduction over natural convection.

It is thus not clear, from the evidence of Figure 51 and Figure 52, whether the difference in behaviour between the two sets of cases could be attributed to stronger convection currents.

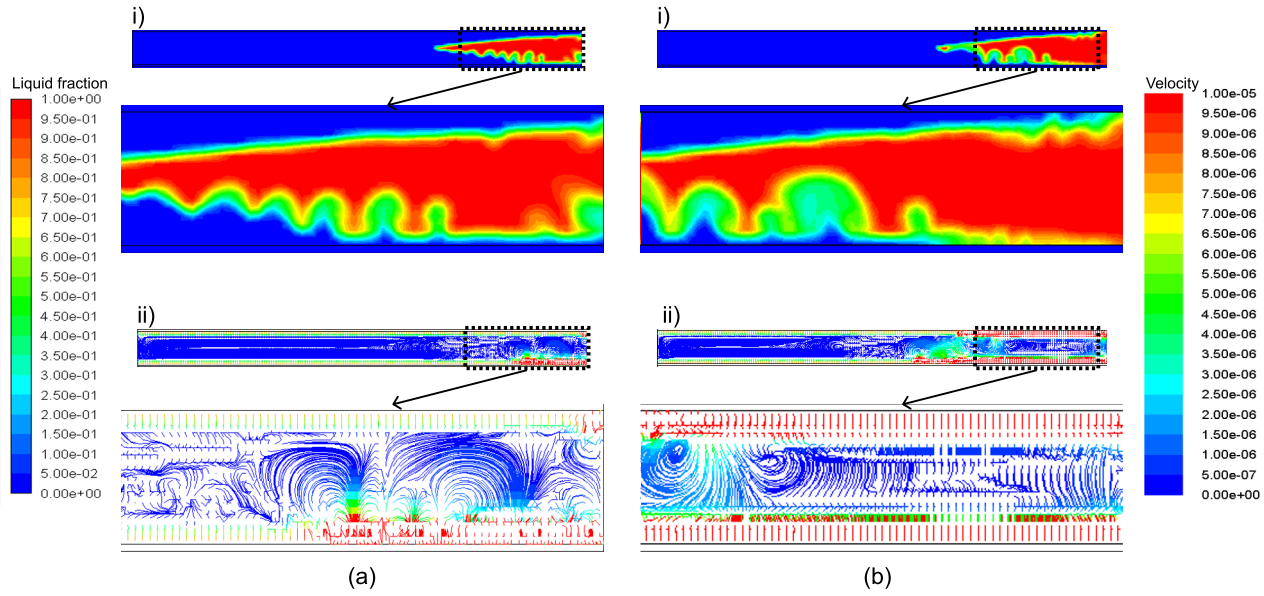

Figure 51 Comparison at $\psi \approx 0.85$ for $P = 4\ mm$ of (a) $\Delta T = 10\ \mathrm{K}$ and (b) $\Delta T = 5\ \mathrm{K}$ showing the (i) phase boundary and (ii) velocity fields.

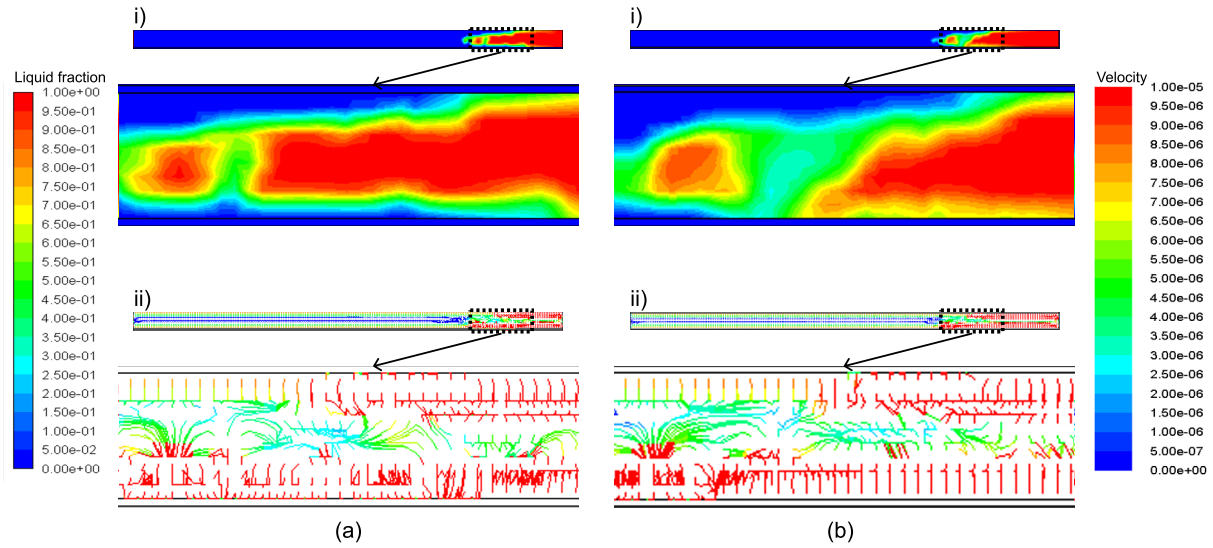

Figure 52 Comparison at $\psi \approx 0.85$ for $P = 2\ mm$ of (a) $\Delta T = 10$ K and (b) $\Delta T = 5$ K showing the (i) phase boundary and (ii) velocity fields.

7.3 Analyses

The trends seen in the results of the different fin pitch spacings for each of the two wall temperatures differences will be analysed and discussed in this section.

7.3.1 $\Delta T = 10$ K

The following results show the maximum value of the solid fraction at various times throughout the solidification process. The solid fractions for cases 1 to 7 are plotted in Figure 53 at a) 100 s b) 500 s c) 1000 s d) 1500 s e) 2000 s and f) 2400 s. In order to better analyse the results, a trendline was fit through the discrete data points to determine the optimum pitch size with a finer resolution. It was decided to make use of a polynomial approximation due its simplicity and the fact that an exact fit is not required, only a good approximation. A fourth order polynomial trendline was chosen because it fit the data the best, with a lowest coefficient of determination (R^2) value of 0.999 – where 0 would be a trendline that does not fit the data at all and 1 a trendline that fits the data perfectly. The maximum value of the trendline is also plotted (as the red dots) in Figure 53 to show which pitch distance could result in the maximum solid fraction if more data points were available.

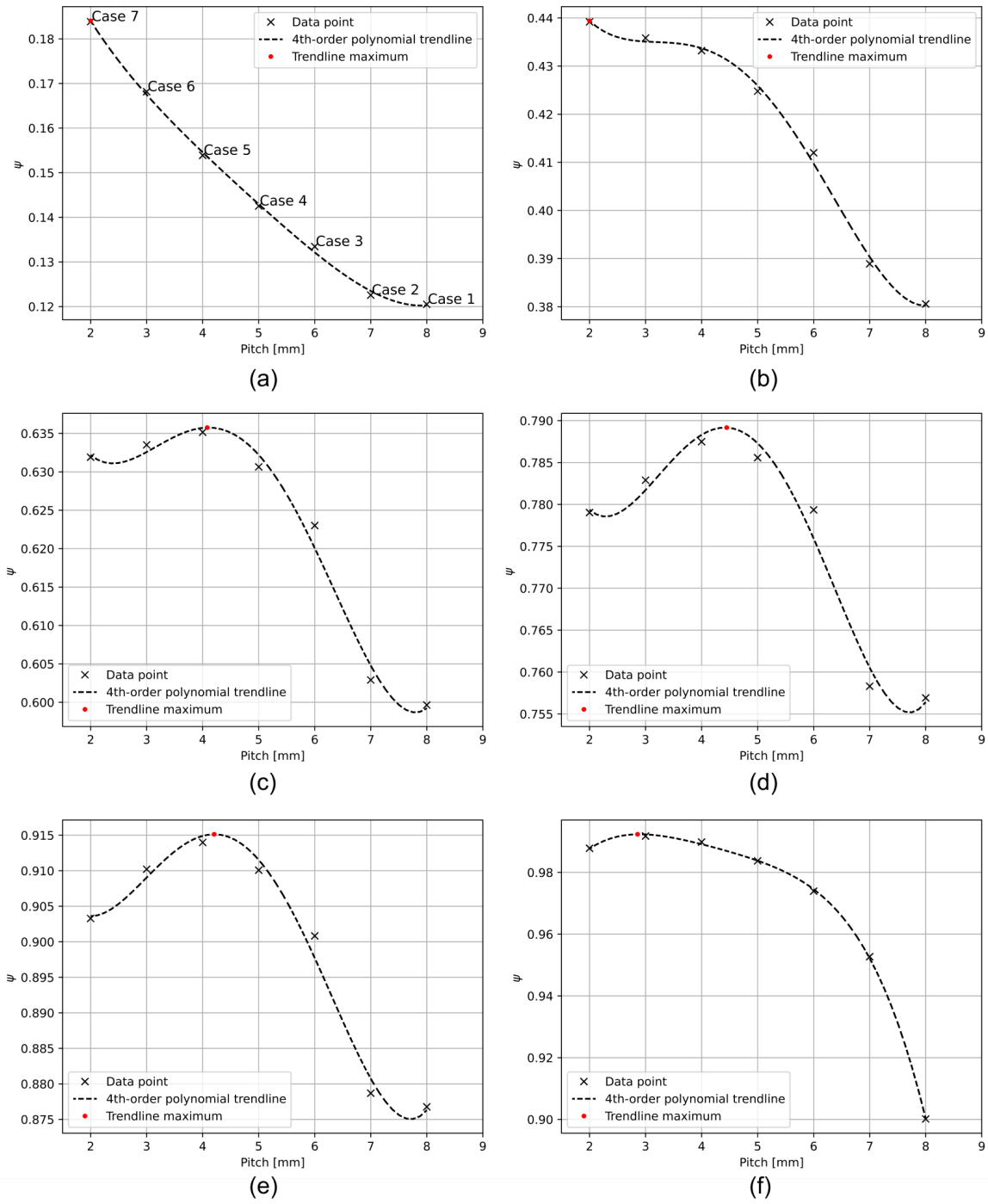

Figure 53 Solid fractions in terms of pitch distance at a) 100 s b) 500 s c) 1000 s d) 1500 s e) 2000 s and f) 2400 s ($\Delta T = 10$ K).

The solid fraction increases with time as more heat is discharged from the PCM. During the early stages of the solidification process (Figure 53a and b) small pitch distances (2 mm or lower) result in the highest solid fraction (which equates to the highest effective heat transfer rate). As the solidification progresses, the pitch distance which results in the highest effective heat transfer rate increases during the middle part of the solidification process (approximately 3.8 mm in Figure 53c and 4.3 mm in Figure 53d when looking at the trendline maximum – the red dot) before decreasing again towards the end (4.1 mm in Figure 53e and 2.8 mm in Figure 53f). The discharge time until the $NaNO_3$ fully solidified was thus not necessarily inversely proportional to the pitch.

A summary of the pitch values that result in the maximised cumulative heat transfer quantities for different intended discharge time spans are presented in Figure 54 for a wide range of time instances. The maximum pitch value obtained from results are presented vs the maximum value from the trendline fit through the data, shown in Figure 53.

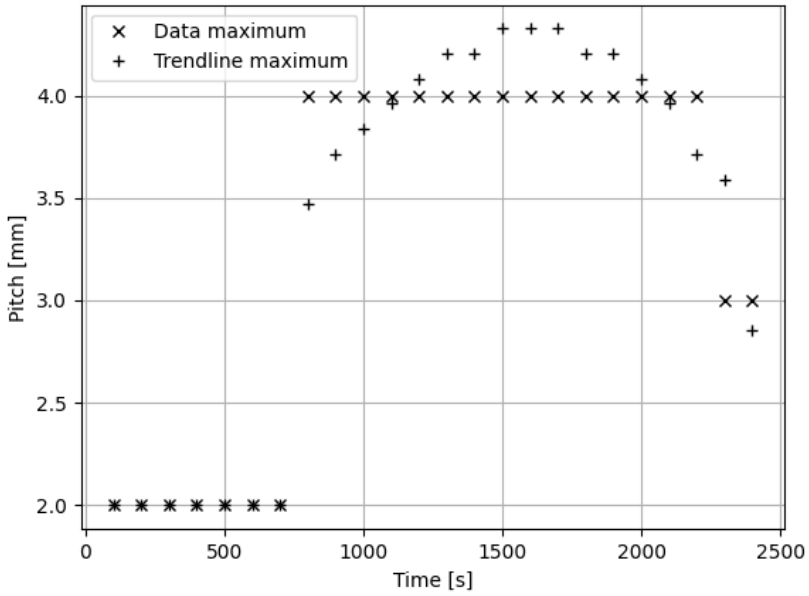

Figure 54 Position of maximum solid-fraction pitch $\Delta T = 10$ K.

For mid-range discharge times (when the thermal storage is not yet fully discharged), a pitch distance of between 4 mm and 4.5 mm resulted in the highest cumulative effective heat transfer rate (the data shows maximum of 4 mm but the trendline reveals pitch distances up to 4.5 mm) because it produced the highest solid fraction compared to the other pitch cases, while for short- and long-range discharge times smaller pitch distances produce higher heat transfer rates. This behaviour is attributed to the influence that the buoyancy induced flow fields (seen in Figure 51a) have which, if well-developed, can speed up the convective heat transfer process at the solid liquid interface. This was evident at larger pitch values. However, at higher solid fractions towards the end of the discharge process, the poor thermal conductivity performance of the solidified phase change material becomes dominant and lower pitch-to-length ratios are preferred.

7.3.2 $\Delta T = 5$ K

Similarly, the maximum values of the solid fractions for cases 8 to 14 are plotted in Figure 55 at a) 100 s b) 1000 s c) 2000 s d) 3000 s e) 4000 s and f) 4700 s. A fourth order polynomial trendline was fit through the data as for $\Delta T = 10$ K in Figure 53. The maximum value of the trendline is again plotted (as the red dots) to show which pitch distance could result in the maximum solid fraction if more data points were available.

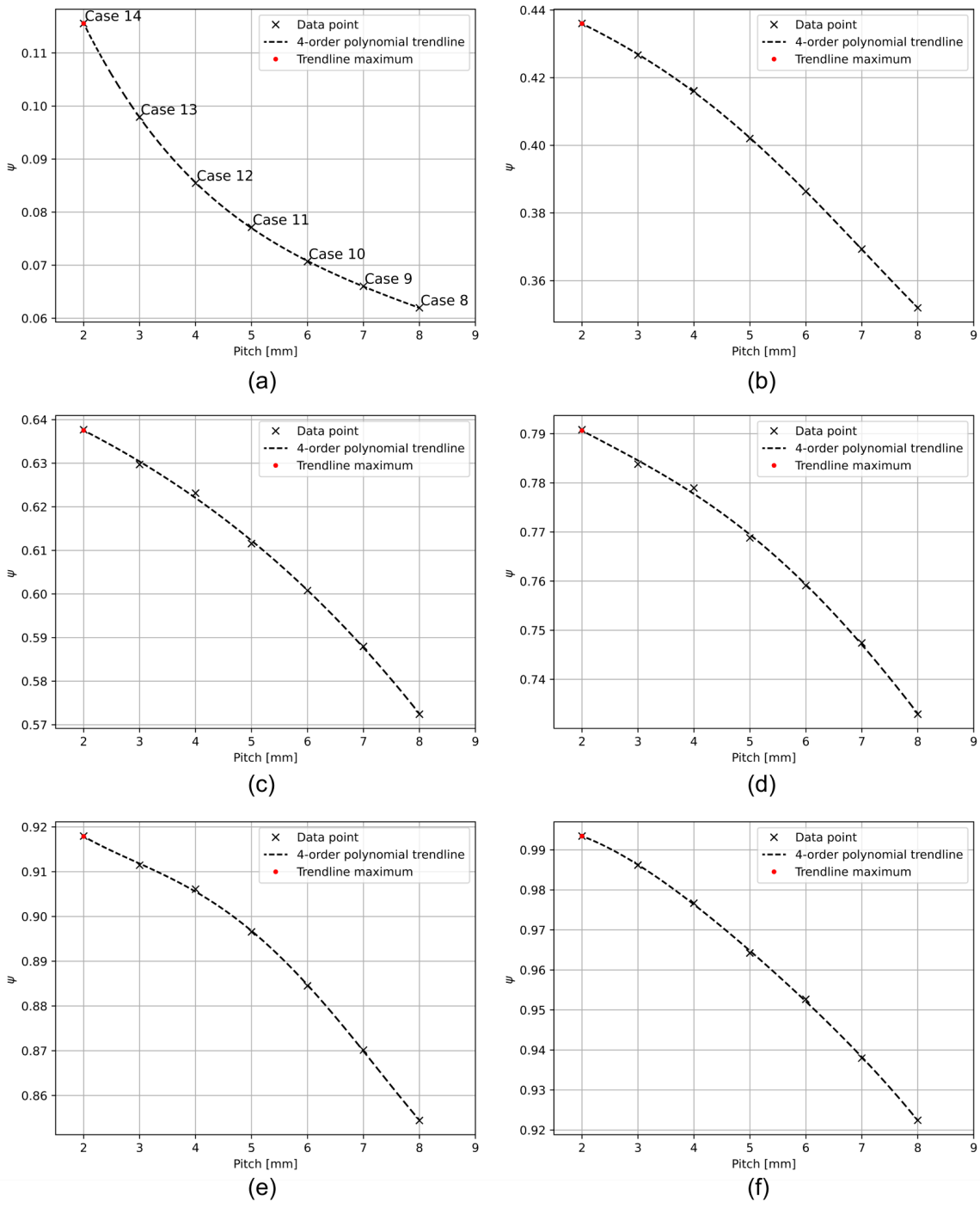

Figure 55 Solid fractions in terms of pitch distance at a) 100 s b) 1000 s c) 2000 s d) 3000 s e) 4000 s and f) 4700 s ($\Delta T = 5$ K).

These cases show a much less interesting trend than the results for $\Delta T = 10$ K – it is clear that the smallest fin pitch distances result in the highest effective heat transfer rate throughout the solidification process. The pitch values that result in maximum heat transfer for various discharge periods (for both the data points and the trendline), shown in Figure 56, reaffirm this.

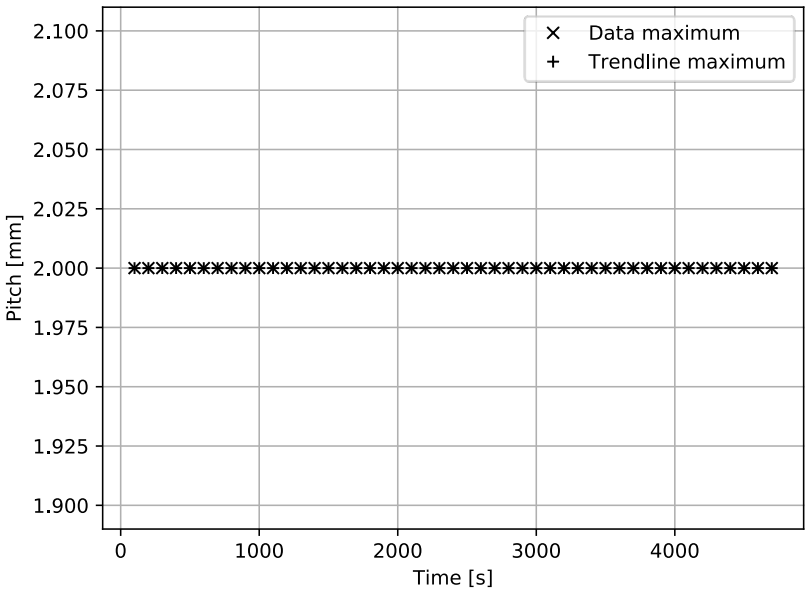

Figure 56 Position of maximum solid fraction pitch $\Delta T = 5$ K.

Figure 57 shows the pitch at which the shortest time is taken to reach different ψ values, as the solidification process progresses, for $\Delta T = 10$ K and $\Delta T = 5$ K. The trends witnessed in Figure 54 and Figure 56 can be seen again, where there seems to be an optimum pitch spacing – which is not the smallest pitch spacing – during the middle-to-end stage of solidification for the lower wall temperature, whereas the smallest fin spacing for the higher wall temperature shows the fastest solidification times.

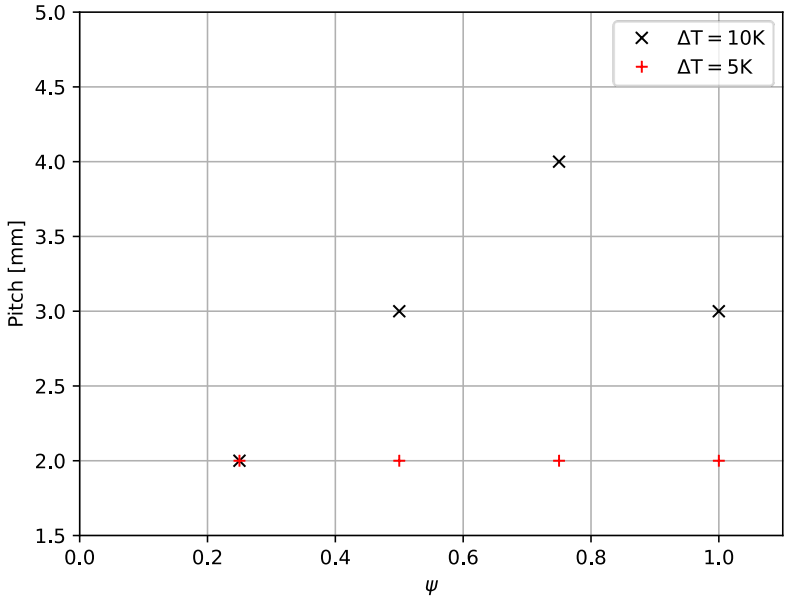

Figure 57 Position of shortest time to ψ for $\Delta T = 10$ K and $\Delta T = 5$ K.

The influence of buoyancy driven flow seems to be the most likely reason for the different trends, with the larger ΔT resulting in stronger buoyancy forces in larger pitch spacings which in turn results in a higher effective heat transfer rate. Figure 51 and Figure 52 did, however,

not show larger velocities in the $\Delta T = 10\ \mathrm{K}$ and $P = 4\ mm$ case (which resulted in the highest effective heat transfer rate at that stage in the process) when compared to the same pitch distance for $\Delta T = 5\ \mathrm{K}$. It is clear that the difference between the wall temperature and the PCM melting temperature plays a role in solidifying behaviour of the PCM for different fin pitch spacings, further investigation is necessary to determine what the impact is.

The results for $\Delta T = 10\ \mathrm{K}$ do, however, show that buoyancy induced natural convection has a significant impact on the effective heat transfer rate during the middle stages of the solidification process. The practical implications of this is that when designing a latent heat TES with plate fins, the intended discharge period has to be considered when choosing the pitch spacing of the fins. Different optimised fin pitch spacings exist to maximise the overall heat transfer quantity – smaller pitch spacings result in higher effective heat transfer rate at the beginning and end of the process and are thus best for short term energy while larger pitch spacings will provide more heat at discharge times corresponding to between midway through and full solidification.

7.4 Chapter summary

This chapter presented the influence of the fin pitch on the time dependent heat transfer rate. The fin pitch was chosen as the design variable to optimise for effective heat transfer out of the PCM enclosure, and two sets of seven fin pitches ranging from 2 mm to 8 mm was defined. The first set of fin pitches was run a wall temperature difference of 10 K and the second set at 5 K.

The $\Delta T = 5\ \mathrm{K}$ set of cases delivered expected results: the smallest fin pitch solidified in the shortest time (thus has the highest effective heat transfer rate) and the largest fin pitch took the longest to solidify (the smallest effective heat transfer rate). The $\Delta T = 10\ \mathrm{K}$ set of cases had more interesting results. The smallest fin pitch did not reach solidification the quickest and the largest fin pitch did not take the longest.

The difference in trends between $\Delta T = 10\ \mathrm{K}$ and $\Delta T = 5\ \mathrm{K}$ could be due to the effect of buoyancy induced natural convection currents being stronger in the cases with a larger ΔT causing the large pitch distances to perform better. When looking at the velocity fields of $P = 2\ mm$ and $P = 4\ mm$ at $\psi \approx 0.85$, it was not evident that the larger ΔT cases had stronger velocity fields. In fact, $P = 4\ mm$ showed larger velocities close to the fin for the smaller ΔT case than for the case with a larger ΔT.

This evidence does not disapprove the hypothesis that it is stronger natural convection flow fields that cause the difference in behaviour between the two sets of temperature differences; more investigation is however needed to better study this aspect.

Considering the larger ΔT, there seems to be an optimal fin pitch depending on the discharge time you are looking for. Short- and long-range discharge times favour smaller fin pitches (when conduction is the dominant heat transfer mechanism), where mid-range discharge times (when natural convection plays a big part in the heat transfer from the liquid PCM to the enclosure wall) favour fin pitches between 4 mm and 4.5 mm. This has to be kept in mind when designing a latent heat TES, the optimum fin pitch spacing will vary depending on the intended discharge time of the TES.

8. Summary, Conclusions and Recommendations

The final summary of the study, the conclusions reached and any recommendations for following studies are presented in this chapter.

8.1 Summary

A numerical parametric study was conducted of a latent heat energy storage device containing $NaNO_3$ as the phase change material with high-conductive aluminium full plate fins to enhance the heat transfer.

A two-dimensional numerical domain was set up consisting of a long vertical aluminium enclosure with the PCM housed inside. An enthalpy-porosity technique (using ANSYS Fluent) was used to model the phase change process while considering the effects of buoyancy driven flow.

A mesh independence study was conducted on a structured uniform quadrangular grid. The errors and grid convergence index of a list of cases with decreasing cell sizes were calculated and it was found that a 0.04×0.04 mm mesh delivers independent results. Similarly, a time step independence study was conducted by comparing cases with decreasing time step values. It was found that as the time step decreased, the error between cases increased. A time step of 0.01 s was found to be the time step that delivered the most independent results.

The numerical model was validated against literature using the independent mesh and time step values obtained from the independence studies. An experimental study of an analysis of a flat plate latent heat storage by Johnson et al. (2014) was chosen to validate the model against. Good correlation was found to exists between experimental results and the results obtained from the numerical model, especially closer to the heat transfer wall. Further away from the heat transfer wall the correlation got slightly weaker but overall the numerical model was able to correctly simulate the thermal and fluid interaction during the solidification of the phase change material.

Once a validated numerical model was defined with independent mesh and time step sizes, the parametric study was set up by keeping the horizontal width of the PCM enclosure and the volume of the fins relative to the total volume of the domain constant and changing the fin pitch distance. Two sets of cases were defined each with constant heat transfer wall temperature differences – $\Delta T = 5\ \mathrm{K}$ and $\Delta T = 10\ \mathrm{K}$ – to investigate whether the temperature difference between the heat transfer wall and the PCM melting temperature will have an influence on the heat transfer rate of different fin pitch distances.

It was found the fin pitch spacing had a significant influence on the effective heat transfer rate for the set of cases with $\Delta T = 10\ \mathrm{K}$. Larger fin spacings favoured improved buoyancy induced flow patterns in the liquid phase, which enhanced internal convective heat transfer midway through the solidification process, while smaller fin spacings resulted in improved thermal conductivity at the beginning and the end of the process. The set of cases with a wall temperature difference of $\Delta T = 5\ \mathrm{K}$ did not show the same pattern. At each stage of the process the smallest fin spacing produced the maximum effective heat transfer rate in this set.

The difference between the two sets of cases might be the difference in ΔT causing different strength buoyancy driven flow and different velocity profiles. Although when the velocity profiles of two cases at different temperature differences were compared at approximately 85% solidification, the case with a smaller ΔT seemed to have higher velocities close to the fin and similar strength convection currents. This does not prove that stronger buoyancy induced flow fields are not the reason that the larger fin pitch spacings performed better at a larger ΔT, it does however mean further investigation is required into the effect of the wall temperature difference on the discharge behaviour of a latent heat TES at different pitch distances.

The trends seen in the results for $\Delta T = 10\ \mathrm{K}$ do, however, show that when designing a TES using PCM and plate fins as heat transfer enhancement, the intended discharge time of the TES needs to be considered when deciding on the fin pitch spacing since different fin pitch spacings produce optimum heat transfer rates and different stages of the solidification process.

All results and the optimal thicknesses found are only for a sodium nitrate PCM. A different PCM with different thermophysical properties will result in different optimum fin pitches.

8.2 Conclusions

The following conclusions can be drawn from the results obtained from this study:

- Natural convection plays a significant role in the heat transfer during PCM solidification, not only conduction.
- The fin pitch spacing of horizontal plate fins in a LHS has an effect on the effective heat transfer of the system, where smaller fin pitch distances promote conductive heat transfer and larger fin pitch distances promote buoyancy driven flow and convective heat transfer.
- Due to the influence of buoyancy induced natural convection flows in the PCM, an optimum fin pitch distance does exist which maximises the overall effective heat transfer of the system.
- The temperature difference between the melting temperature of the PCM and the heat transfer wall has an effect on the strength of the buoyancy flow fields and thus the heat transfer rate of the system. It can be postulated that as this temperature difference increases, the buoyancy driven flow would start to become more dominant and more widely ranging optimum fin pitch distances might exist.

8.3 Recommendations

The hypothesis that the difference in behaviour between the cases with different ΔT is due to buoyancy driven flow fields, could not be proven by comparing the velocity flow fields between cases with different wall temperatures. A more in-depth study is needed to determine what the cause of this difference is.

Only one PCM was used in this study and the results obtained are reliant on the thermophysical properties of sodium nitrate. A study investigating the effect of the thermal physical properties of different PCMs on the optimum fin thickness is also needed.

Bibliography

ABDULATEEF, A. M., MAT, S., ABDULATEEF, J., SOPIAN, K. & AL-ABIDI, A. A. 2018. Geometric and design parameters of fins employed for enhancing thermal energy storage systems: a review. *Renewable and Sustainable Energy Reviews,* 82**,** 1620-1635.

ACHARD, P., LECOMTE, D. & MAYER, D. 1983. Etude des transferts thermiques dans un stockage par chaleur latente utilisant un échangeur tubulaire immergé. *Revue Générale de thermique Fr.,* 254**,** 169-175.

AGYENIM, F., HEWITT, N., EAMES, P. & SMYTH, M. 2010. A review of materials, heat transfer and phase change problem formulation for latent heat thermal energy storage systems (LHTESS). *Renewable and Sustainable Energy Reviews,* 14**,** 615-628.

ANSYS 2018. ANSYS Fluent material database. *Fluent.* 18.1 ed.

ATAER, O. E. 2006. Storage of Thermal Energy. *Encyclopedia of Life Support Systems.* Oxford: Eolss.

BABY, R. & BALAJI, C. 2013. Thermal optimization of PCM based pin fin heat sinks: An experimental study. *Applied Thermal Engineering,* 54**,** 65-77.

BATHELT, A. G., VAN BUREN, P. D. & VISKANTA, R. 1979. HEAT TRANSFER DURING SOLIDIFICATION AROUND A COOLED HORIZONTAL CYLINDER. *AIChE Symposium Series.* San Diego.

BAUER, T., LAING, D. & TAMME, R. 2012. Characterization of Sodium Nitrate as Phase Change Material. *International Journal of Thermophysics,* 33**,** 91-104.

BUTALA, V. & STRITIH, U. 2009. Experimental investigation of PCM cold storage. *Energy and Buildings,* 41**,** 354-359.

COCO-ENRÍQUEZ, L., MUÑOZ-ANTÓN, J. & MARTÍNEZ-VAL, J. M. 2015. Integration between direct steam generation in linear solar collectors and supercritical carbon dioxide Brayton power cycles. *International Journal of Hydrogen Energy,* 40**,** 15284-15300.

DE CÉSARO OLIVESKI, R., BECKER, F., ROCHA, L. A. O., BISERNI, C. & EBERHARDT, G. E. S. 2021. Design of fin structures for phase change material (PCM) melting process in rectangular cavities. *Journal of Energy Storage,* 35**,** 102337.

DEBICH, B., EL HAMI, A., YAICH, A., GAFSI, W., WALHA, L. & HADDAR, M. 2020. Design optimization of PCM-based finned heat sinks for mechatronic components: A numerical investigation and parametric study. *Journal of Energy Storage,* 32**,** 101960.

DHAIDAN, N. S. & KHODADADI, J. M. 2015. Melting and convection of phase change materials in different shape containers: A review. *Renewable and Sustainable Energy Reviews,* 43**,** 449-477.

DUNHAM, M. T. & IVERSON, B. D. 2014. High-efficiency thermodynamic power cycles for concentrated solar power systems. *Renewable and Sustainable Energy Reviews,* 30**,** 758-770.

EYRES, D. R. HARTREE, F. R. INGHAM, R. J. SARJANT & J. B. WAGSTAFF 1946. The calculation of variable heat flow in solids. *Philosophical Transactions of the Royal Society of London. Series A, Mathematical and Physical Sciences,* 240**,** 1-57.

FAIAS, S., SANTOS, P., SOUSA, J. & CASTRO, R. 2008. An overview on short and long-term response energy storage devices for power systems applications. *Renewable Energy and Power Quality Journal,* 1**,** 442-447.

FARID, M. M. & HUSIAN, R. M. 1990. An electrical storage heater using the phase-change method of heat storage. *Energy Conversion and Management,* 30**,** 219-230.

FARID, M. M., KHUDHAIR, A. M., RAZACK, S. A. K. & AL-HALLAJ, S. 2004. A review on phase change energy storage: materials and applications. *Energy Conversion and Management,* 45**,** 1597-1615.

FAZILATI, M. A. & ALEMRAJABI, A. A. 2013. Phase change material for enhancing solar water heater, an experimental approach. *Energy Conversion and Management,* 71**,** 138-145.

GARVEY, S. Medium-Duration Energy Storage explained. Medium Duration Energy Storage in the Net Zero UK, 2020 Online.

HENRY, H. & STAVROS, A. A. 1996. Mathematical modelling of solidification and melting: a review. *Modelling and Simulation in Materials Science and Engineering,* 4**,** 371.

HERRMANN, U. & KEARNEY, D. 2002. Survey of Thermal Energy Storage for Parabolic Trough Power Plants. *Journal of Solar Energy Engineering,* 124.

ISLAM, M. T., HUDA, N., ABDULLAH, A. B. & SAIDUR, R. 2018. A comprehensive review of state-of-the-art concentrating solar power (CSP) technologies: Current status and research trends. *Renewable and Sustainable Energy Reviews,* 91**,** 987-1018.

JOHNSON, M., FISS, M., KLEMM, T. & ECK, M. 2014. Test and Analysis of a Flat Plate Latent Heat Storage Design. *Energy Procedia,* 57**,** 662-671.

KALLANNAVAR, S., MASHYAL, S. & RAJANGALE, M. 2020. Effect of tube layout on the performance of shell and tube heat exchangers. *Materials Today: Proceedings,* 27**,** 263-267.

KAMKARI, B. & SHOKOUHMAND, H. 2014. Experimental investigation of phase change material melting in rectangular enclosures with horizontal partial fins. *International Journal of Heat and Mass Transfer,* 78**,** 839-851.

KARNI, J. 2012. Solar-thermal power generation. *Annual review of heat transfer,* 15**,** 37-92.

KHARE, S., DELL'AMICO, M., KNIGHT, C. & MCGARRY, S. 2012. Selection of materials for high temperature latent heat energy storage. *Solar Energy Materials and Solar Cells,* 107**,** 20-27.

KOLLER, M., WALTER, H. & HAMETER, M. 2016. Transient Numerical Simulation of the Melting and Solidification Behavior of NaNO3 Using a Wire Matrix for Enhancing the Heat Transfer. *Energies,* 9**,** 205.

KURAVI, S., TRAHAN, J., GOSWAMI, D. Y., RAHMAN, M. M. & STEFANAKOS, E. K. 2013. Thermal energy storage technologies and systems for concentrating solar power plants. *Progress in Energy and Combustion Science,* 39**,** 285-319.

LI, Q., LI, C., DU, Z., JIANG, F. & DING, Y. 2019. A review of performance investigation and enhancement of shell and tube thermal energy storage device containing molten salt based phase change materials for medium and high temperature applications. *Applied Energy,* 255**,** 113806.

LIU, H. & AWBI, H. B. 2009. Performance of phase change material boards under natural convection. *Building and Environment,* 44**,** 1788-1793.

LIU, M., SAMAN, W. & BRUNO, F. 2012. Review on storage materials and thermal performance enhancement techniques for high temperature phase change thermal storage systems. *Renewable and Sustainable Energy Reviews,* 16**,** 2118–2132.

LOMONACO, A., HAILLOT, D., PERNOT, E., FRANQUET, E. & BÉDÉCARRATS, J.-P. 2016. Sodium nitrate thermal behavior in latent heat thermal energy storage: A study of the impact of sodium nitrite on melting temperature and enthalpy. *Solar Energy Materials and Solar Cells,* 149**,** 81-87.

LONDON, A. L. & SEBAN, R. A. 1943. Rate of ice formation. *Trans. ASME***,** 771-778.

LOVEGROVE, K. & STEIN, W. 2012. *Concentrating solar power technology,* Oxford, Woodhead Publishing Limited.

MAHFUZ, M. H., ANISUR, M. R., KIBRIA, M. A., SAIDUR, R. & METSELAAR, I. H. S. C. 2014a. Performance investigation of thermal energy storage system with Phase Change Material (PCM) for solar water heating application. *International Communications in Heat and Mass Transfer,* 57**,** 132-139.

MAHFUZ, M. H., KAMYAR, A., AFSHAR, O., SARRAF, M., ANISUR, M. R., KIBRIA, M. A., SAIDUR, R. & METSELAAR, I. H. S. C. 2014b. Exergetic analysis of a solar thermal power system with PCM storage. *Energy Conversion and Management,* 78**,** 486-492.

MARRERO, I. O., LEFSAKER, A. M., RAZANI, A. & KIM, K. J. 2002. Second law analysis and optimization of a combined triple power cycle. *Energy Conversion and Management,* 43**,** 557-573.
MARSHALL, R. Studies of natural convection effects in an annulus containing a phase change material. 1978-01-01 1978 United Kingdom. University Coll., Cardiff, England.
NIYAS, H., PRASAD, S. & MUTHUKUMAR, P. 2017. Performance investigation of a lab–scale latent heat storage prototype – Numerical results. *Energy Conversion and Management,* 135**,** 188-199.
OUWERKERK, H. & DE LANGE, H. C. 2006. Technical and economical feasibility of the Rankine compression gas turbine (RCG). *Applied Thermal Engineering,* 26**,** 413-420.
P SUKHATME, S. 1997. Solar thermal power generation. *Chemical Science,* 109**,** 521-531.
PELAY, U., LUO, L., FAN, Y., STITOU, D. & ROOD, M. 2017. Thermal energy storage systems for concentrated solar power plants. *Renewable and Sustainable Energy Reviews,* 79**,** 82-100.
PIZZOLATO, A., SHARMA, A., MAUTE, K., SCIACOVELLI, A. & VERDA, V. 2017. Design of effective fins for fast PCM melting and solidification in shell-and-tube latent heat thermal energy storage through topology optimization. *Applied Energy,* 208**,** 210-227.
POINTNER, H., DE GRACIA, A., VOGEL, J., TAY, N. H. S., LIU, M., JOHNSON, M. & CABEZA, L. F. 2016. Computational efficiency in numerical modeling of high temperature latent heat storage: Comparison of selected software tools based on experimental data. *Applied Energy,* 161**,** 337-348.
REDPATH, D. A. G., LO, S. N. G. & EAMES, P. C. 2010. Experimental investigation and optimisation study of a direct thermosyphon heat-pipe evacuated tube solar water heater subjected to a northern maritime climate. *International Journal of Ambient Energy,* 31**,** 91-100.
REN21 2020. Renewable 2020 Global Status Report. Renewable Energy Policy Network for the 21st Century.
ROBAK, C. W., BERGMAN, T. L. & FAGHRI, A. 2011. Economic evaluation of latent heat thermal energy storage using embedded thermosyphons for concentrating solar power applications. *Solar Energy,* 85**,** 2461-2473.
RUIZ-CABAÑAS, F. J., JOVÉ, A., PRIETO, C., MADINA, V., FERNÁNDEZ, A. I. & CABEZA, L. F. 2017. Materials selection of steam-phase change material (PCM) heat exchanger for thermal energy storage systems in direct steam generation facilities. *Solar Energy Materials and Solar Cells,* 159**,** 526-535.
SCHOENUNG, S. M. 2001. Characteristics and Technologies for Long- vs. Short-Term Energy Storage. *DOE Energy Storage Systems Program.* Sandia National Laboratories.
SHARIFI, N., BERGMAN, T. L. & FAGHRI, A. 2011. Enhancement of PCM melting in enclosures with horizontally-finned internal surfaces. *International Journal of Heat and Mass Transfer,* 54**,** 4182-4192.
SHARMA, A., TYAGI, V. V., CHEN, C. R. & BUDDHI, D. 2009. Review on thermal energy storage with phase change materials and applications. *Renewable and Sustainable Energy Reviews,* 13**,** 318-345.
SHARMA, R. K., GANESAN, P., TYAGI, V. V., METSELAAR, H. S. C. & SANDARAN, S. C. 2015. Developments in organic solid–liquid phase change materials and their applications in thermal energy storage. *Energy Conversion and Management,* 95**,** 193-228.
SHATIKIAN, V., ZISKIND, G. & LETAN, R. 2005. Numerical investigation of a PCM-based heat sink with internal fins. *International Journal of Heat and Mass Transfer,* 48**,** 3689-3706.
SHOKOUHMAND, H. & KAMKARI, B. 2013. Experimental investigation on melting heat transfer characteristics of lauric acid in a rectangular thermal storage unit. *Experimental Thermal and Fluid Science,* 50**,** 201-212.

SIVASAMY, P., DEVARAJU, A. & HARIKRISHNAN, S. 2018. Review on Heat Transfer Enhancement of Phase Change Materials (PCMs). *Materials Today: Proceedings,* 5**,** 14423-14431.

SOUAYFANE, F., FARDOUN, F. & BIWOLE, P.-H. 2016. Phase change materials (PCM) for cooling applications in buildings: A review. *Energy and Buildings,* 129**,** 396-431.

STEFAN, J. 1889. Uber einge problem der theoric der warmeleitung. *S.-B Wien Akad. Mat. Natur.***,** 173-484.

TAMME, R., STEINMANN, W.-D. & LAING, D. 2005. Thermal Energy Storage Technology for Industrial Process Heat Applications. 417-422.

VELRAJ, R., SEENIRAJ, R. V., HAFNER, B., FABER, C. & SCHWARZER, K. 1999. HEAT TRANSFER ENHANCEMENT IN A LATENT HEAT STORAGE SYSTEM1Paper presented at the ISES Solar World Congress, Taejon, South Korea, 24–29 August 1997.1. *Solar Energy,* 65**,** 171-180.

VERSTEEG, H. K. & MALALASEKERA, W. 2006. *An introduction to computational fluid dynamics : the finite volume method*, New York : Pearson Education.

VOLLER, V. R. & PRAKASH, C. 1987. A fixed grid numerical modelling methodology for convection-diffusion mushy region phase-change problems. *International Journal of Heat and Mass Transfer,* 30**,** 1709-1719.

WANG, W., LI, H., GUO, S., HE, S., DING, J., YAN, J. & YANG, J. 2015. Numerical simulation study on discharging process of the direct-contact phase change energy storage system. *Applied Energy,* 150**,** 61-68.

XU, B., LI, P. & CHAN, C. 2015. Application of phase change materials for thermal energy storage in concentrated solar thermal power plants: A review to recent developments. *Applied Energy,* 160**,** 286-307.

YU, S.-C., CHEN, L., ZHAO, Y., LI, H.-X. & ZHANG, X.-R. 2015. A brief review study of various thermodynamic cycles for high temperature power generation systems. *Energy Conversion and Management,* 94**,** 68-83.

ZALBA, B., MARÍN, J. M., CABEZA, L. F. & MEHLING, H. 2003. Review on thermal energy storage with phase change: materials, heat transfer analysis and applications. *Applied Thermal Engineering,* 23**,** 251-283.